Developing Spin Devices for Logic and Memory Applications

Zheng Gu

Electrical Engineering and Computer Sciences
University of California at Berkeley

Technical Report No. UCB/EECS-2014-225
http://www.eecs.berkeley.edu/Pubs/TechRpts/2014/EECS-2014-225.html

December 18, 2014

Copyright © 2014, by the author(s).
All rights reserved.

Permission to make digital or hard copies of all or part of this work for personal or classroom use is granted without fee provided that copies are not made or distributed for profit or commercial advantage and that copies bear this notice and the full citation on the first page. To copy otherwise, to republish, to post on servers or to redistribute to lists, requires prior specific permission.

Developing Spin Devices for Logic and Memory Applications

By

Zheng Gu

A dissertation submitted in partial satisfaction of the

requirements for the degree of

Doctor of Philosophy

in

Engineering – Electrical Engineering and Computer Sciences

in the

Graduate Division

of the

University of California, Berkeley

Committee in charge:

Professor Jeffrey Bokor, Chair
Professor Sayeef Salahuddin
Professor Irfan Siddiqi

Fall 2014

Developing Spin Devices for Logic and Memory Applications

© 2014
by
Zheng Gu

Abstract

Developing Spin Devices for Logic and Memory Applications

by

Zheng Gu

Doctor of Philosophy in Electrical Engineering and Computer Sciences

University of California, Berkeley

Professor Jeffrey Bokor, Chair

Due to increasingly pervasive computation hardware, energy efficient electronics has gained much research and development attention. One approach toward this goal is to use spintronics, which leverages the spin degree of freedom of electrons. The fundamentally smaller energy dissipation from flipping spins instead of moving charges may lead to overall more efficient devices. This is in part due to the ability to retain information without any power as well as smaller amounts of Joule heating.

In this dissertation, we focus on a subset of spin logic devices known as nanomagnetic logic. Using a variety of modeling techniques and experimental imaging techniques, we investigate the performance of these devices in terms of speed and reliability. We also use optical techniques to investigate a spin-charge coupling mechanism known as the Spin Hall Effect. This effect is a very power-efficient way to switch nanomagnets and has obvious applications to both spin logic and memory. While spin logic devices still face many challenges, spin memory devices have become fairly feasible. With the rapid pace of innovation in this field, the outlook for spin devices in general is promising.

Contents

1: Introduction **1**

2: Spin Logic Systems
2.1: Field-Coupled Nanomagnetic Logic **2**
2.2: Torque-Coupled Spin Logic **4**

3: Theoretical Models for the Behavior of Ferromagnets
3.1: The Stoner-Wohlfarth Model **8**
3.2: The Landau-Lifshitz Equation **10**
3.3: The Addition of Thermal Effects **14**

4: Configurational Anisotropy in Nearly-Single-Domain Magnets
4.1: Edges and Corners of Nearly-Single-Domain Magnets **16**
4.2: Simulation Study of Configurational Phase Space **18**
4.3: Design of Nanomagnet Shapes for Nanomagnetic Logic **20**
4.4: Simulation Extraction of Anisotropy Constants **21**
4.5: Magneto-Optic Kerr Effect **24**

5: Information Transmission in Nanomagnetic Logic
5.1: Behavior of Chains in Nanomagnetic Logic **31**
5.2: Analytical Study of Chains of Nanomagnets with Biaxial Anisotropy **34**
5.3: Simulation Study of Chains of Nanomagnets with Biaxial Anisotropy **41**
5.4: Simulation Study of Chains of Nanomagnets with Configurational Anisotropy **47**
5.5: Signal Propagation Speed in Nanomagnetic Logic **49**

6: Static Experimental Methods for Investigating Nanomagnetic Logic
6.1: X-ray Magnetic Circular Dichroism **53**
6.2: Thermally Assisted Signal Propagation in Chains **55**
6.3: Surface Quality Effects on Signal Propagation **58**
6.4: Signal Propagation from Short Clock Field Pulses **61**
6.5: Magnetic Force Microscopy **65**

7: Dynamics Experimental Methods for Investigating Nanomagnetic Logic
7.1: Stroboscopic X-ray Magnetic Circular Dichroism **68**
7.2: Time-Resolved PEEM Experimental Setup **69**
7.3: Signal Propagation Dynamics in Nanomagnetic Logic Chains **73**

8: Spin-Transfer Torque and Energy-Efficient Switching
8.1: Spin-Transfer Torque Magnetic Random Access Memories **78**
8.2: The Spin Hall Effect in Metals **80**

8.3: Two-Bit Free Layers using Configurational Anisotropy **84**

9: Dynamic Experimental Methods for Investigating the Spin Hall Effect

9.1: Optical Second Harmonic Generation **88**

9.2: Time-Resolved SHG Experimental Setup **93**

9.3: Detection of Spin Accumulation on Bare Platinum due to SHE **96**

10: Conclusion 100

References 101

A: OOMMF Programs

A.1: Exploring Configurational Phase Diagrams **105**

A.2: Characterizing Switching Magnetic Fields **106**

A.3: Applying Piecewise Linear Magnetic Fields **109**

B: MATLAB Programs

B.1: Exploring Chains with Second-Order Anisotropy **112**

B.2: Reading and Processing SPE Images **115**

B.3: Generating OOMMF Image Atlases **118**

C: Python Programs

C.1: Efficient Multi-Threading in OOMMF **122**

D: Fabrication Techniques

D.1: Bi-Layer Lift-Offs with Lift-Off Resist **123**

D.2: Surface Planarization with Spin-On Dielectrics **126**

Acknowledgements

I would like to thank my advisor for his guidance and for the freedom to pursue knowledge. I am grateful for the opportunities to explore the breadth and depth of my disciplines both academically and practically. I was fortunate to have been granted a proper graduate experience.

For their contributions to my work that include training, teaching, discussions, resources, and direct assistance, I would like to acknowledge the members of the research group of professor Jeffrey Bokor, the members of the research group of professor Sayeef Salahuddin, the members of the research group of professor Eli Yablonovitch, the members of the research group of professor Ramamoorthy Ramesh, the staff of the Advanced Light Source at Lawrence Berkeley National Laboratory, the staff of the Center for X-ray Optics at Lawrence Berkeley National Laboratory, the staff of the Experimental Systems Group at Lawrence Berkeley National Laboratory, the staff of the Molecular Foundry at Lawrence Berkeley National Laboratory, the users and staff of the Marvell Nanofabrication Laboratory at the University of California, the staff of the Cory Hall Machine Shop at the University of California, the members of the Ion Beam Technology group at Lawrence Berkeley National Laboratory, the faculty of the department of Physics at the University of California, the faculty of the department of Electrical Engineering at the University of California, the faculty of the department of Materials Science at the University of California, the staff of the Engineering Research Support Organization at the University of California, and the programs that have funded my work.

Finally, for their love and support in life, I would like to thank my friends and family.

Chapter 1. Introduction

Energy usage and waste is a significant challenge to modern societies worldwide. On the one hand, much effort and progress has so far been made toward sustainable energy generation. On the other hand, more efficient use of available energy has been another major focus of research and development. Especially for situations limited by energy generation throughput (whether by supply, demand, or cost) or energy storage capacity (for battery-powered mobile devices), efficiency is very important. For example, electric lighting has improved by almost a factor of twenty[1-3]. However, even more tremendous has been the rapid progress in integrated electronics, which has seen multiple orders of magnitude in improvement[1,2,4]. Unfortunately, this pace of scaling is now at an end[5,6] and growing compute power demand (both on the infrastructure side due to cloud computing and the consumer side due to mobile devices) results in an increasing interest in energy-efficient electronics[2,7].

Some promising visions toward more efficient devices are found in proposals of spin devices[8,9] (spintronics). Such devices take advantage of the intrinsic spin degree of freedom of electrons and are intended to supplant complementary metal-oxide-semiconductor (CMOS) devices. Use of ferromagnetic elements is very common in spin devices, since they fundamentally provide a couple of advantages. The first is non-volatility, which rids devices of the need for standby power in order to retain information. The second is lower switching energy, which arises due to the strongly-interacting nature of spins[4,10]. Simulations have shown that at least fundamentally, spin switches need not dissipate more energy than the thermodynamic limit[11,12]. Additionally, optical control of spins has been demonstrated[13,14] and may lead to sophisticated devices integrating multiple new technologies.

This work investigates the performance of a particular spin logic device, the physics of a phenomenon that relates spin and charge, and the shape properties of nano-scale ferromagnets. It also documents many specific experimental, fabrication, and simulation details so that others may benefit by either continuing the work or applying the methods elsewhere.

Chapter 2. Spin Logic Systems

1. Field-Coupled Nanomagnetic Logic

Spin logic has a rich variety of different designs. We introduce a selection of designs categorized into two classifications. We describe designs that use magnetic fields (stray fields) for interactions between logic elements in this section. In the next section, we describe designs that use carriers of spin torque for interactions between logic elements. The descriptions presented here will review at a high level how various architectures perform logic operations.

Field-coupled nanomagnetic logic (NML) uses discrete nanomagnet islands arranged in ordered patterns. The gaps between islands are small enough so that the stray field interactions between islands are significant. In some variants known as magnetic quantum-dot cellular automata[10,15] (MQCA), the islands are small and are treated as single-domain. In these variants, interconnects are formed from line-like arrangements of field-coupled islands called chains and gates are formed from intersection-like arrangements of field-coupled islands. In other variants known as perpendicular nanomagnetic logic[13] (pNML), the islands are large enough to form domains and can have a wide range of shapes. We will use the term NML to refer to all of the above field-coupled designs.

Figure 2.1 indicates the stray field directions around a magnetic dot (approximately a dipole field) as well as two basic configurations of a pair of dots. If we take the magnetic moment of any given dot projected along the easy anisotropy axis to represent a binary state, then we can map the magnetic moment up and down states to represent digital zero and one. Due to the Zeeman interaction from stray-field coupling, the pairwise configurations shown in figure 2.1 become logically equivalent to an inverter and a buffer. Respectively, these two pairwise arrangements are referred to as antiferromagnetic coupling and ferromagnetic coupling. Interconnects can thus be formed from either a straightforward extension of the buffer or any even number of cascaded inverters. To

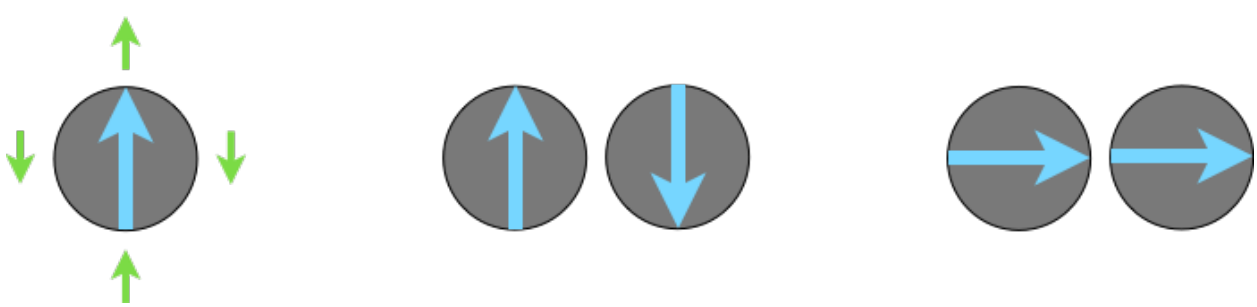

Figure 2. 1: A magnetic dot (left) with its magnetic moment (blue) and stray field (green) indicated. A pair of field-coupled dots can be an inverter (center) or a buffer (right).

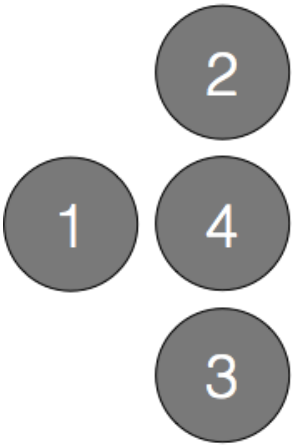

1	0	0	0	0	1	1	1	1
2	0	0	1	1	0	0	1	1
3	0	1	0	1	0	1	0	1
4	0	1	1	1	0	0	0	1

Figure 2. 2: Layout (left) of MLG with inputs labeled 1, 2, and 3 and output labeled 4. Based on equal stray field coupling from each input, the truth table (right) for the output is produced. The leftmost (blue) column indicates the island whose state is given in the row. Setting input 1 to 0 reduces it to an OR gate. Setting input 1 to 1 reduces it to an AND gate.

perform Boolean logic, NML makes use of the majority logic gate[1,15,16] (MLG) shown in figure 2.2. The gate has three inputs surrounding an output magnet such that each input contributes equally to the output. Since there are an odd number of binary inputs, there is always a majority contribution from the inputs that determines the output state. The truth table is given in figure 2.2 and we note that the functionality of either AND or OR binary logic functions can be reproduced by holding the unused input constant.

In comparison with charge-based logic, notable advantages[1] of NML include low switching energy, non-volatility, and radiation-hardness. Calculations for energy dissipated per switching event falls into the tens of k_BT range[1,4,11,17], while non-volatility eliminates leakage dissipation and thus further reduces power usage. Unfortunately, slow speed is an inherent disadvantage[5,10,18] and poor reliability[7,19] is currently a challenge. For MQCA specifically, race conditions[8,16] are also a complicating issue. In pNML designs, race conditions are eliminated but speed is even slower due to use of domain wall motion[10,16].

Due to out-of-plane anisotropy in pNML, if planar arrangements are used the only pairwise arrangements are of the antiferromagnetic coupling type. Each island has specifically engineered coupling sites known as artificial domain wall nucleation centers[11,20] (created by focused ion beam irradiation) that have lower coercivity compared to the rest of the island[13,20]. When influenced by the stray field of a nearby island, a small applied field parallel to the stray field would nucleate a domain at the coupling site, while an equally small applied field antiparallel to the stray field would not. An arrangement of a coupling site of one island next to part of another island (that is not a coupling site, since otherwise the islands would switch each other) forms an inverter[10,21]. An MLG of essentially the same geometry as in MQCA can still be

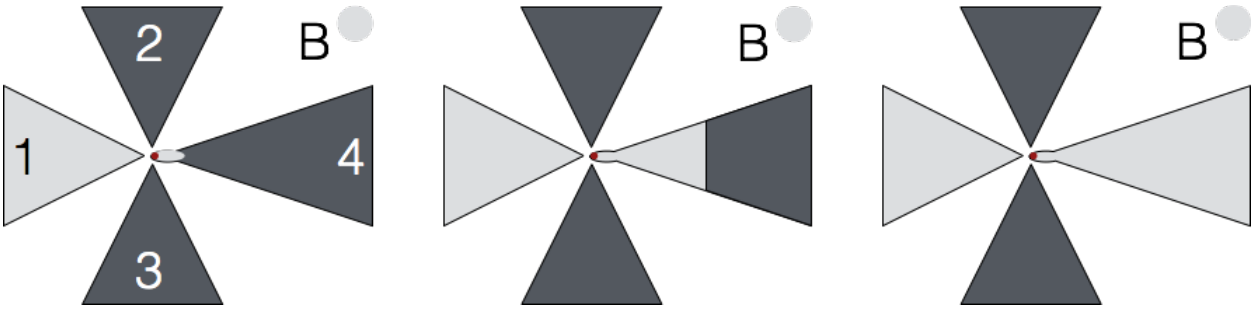

Figure 2. 3: A pNML MLG with inputs labeled 1, 2, and 3 and output labeled 4. Light gray and dark gray areas indicate opposite out-of-plane magnetization. The dot labeled B indicates the direction of applied field. The red speck indicates the coupling site. The progression of switching goes from left to right. B causes a domain to nucleate at the coupling site (left), which then expands (middle) by domain wall motion through magnet 4 until the whole magnet switches (right). The signal thus propagated from left to right.

constructed using a coupling site on the output magnet. Figure 2.3 shows the operation of the pNML MLG as well as the domain wall motion. The combination of the applied field and domain wall motion allows a single island to be an interconnect equivalent in pNML, since the nucleated domain grows to span the entire island. A two-layer MLG[13] that uses both ferromagnetic and antiferromagnetic coupling has also been demonstrated in pNML.

To implement a digital computation system, five device requirements[1,16] (sometimes known as the fundamental tenets) need to be satisfied. These are: functionally complete logic set, non-linear response characteristics, devices that can be concatenated, devices that provide signal gain, and well-defined signal directionality. NML has been demonstrated to satisfy all of these tenets[1]. The combination of the inverter and MLG form a complete Boolean logic set. The switching behavior of magnets is non-linear as observed in typical hysteresis curves. The stray field of one magnet controls the switching of another magnet and thus magnets can be concatenated. Demonstrations of fan-outs[11,17] show that one magnet's stray field can control the switching of at least two more, thus providing gain. Demonstrations of signal propagation[10,18] show clear directionality of the movement of information. Satisfying these tenets is an important step in showing that NML can be a viable spin logic system that is worth pursuing further. The original work on NML described in this thesis pertains mostly to MQCA.

2. Torque-Coupled Spin Logic

Many torque-coupled spin logic schemes use spin-transfer torque internally in a device, but use charge currents to interface (through electrical interconnects) between devices. This allows them to be somewhat less exotic and makes for more straightforward integration with CMOS circuits. Presumably, the benefit would be the ability to replace

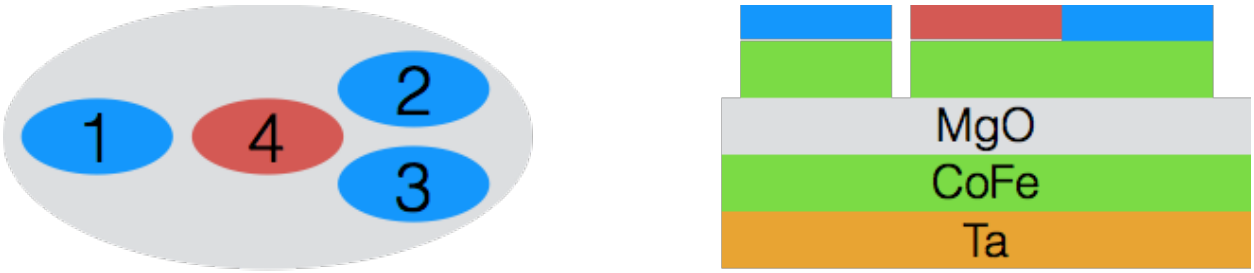

Figure 2. 4: STMG top view (left) and side view (right) with inputs labeled 1, 2, and 3 and output labeled 4. Materials for the stack (spin valve sandwiched between contacts) are indicated by the colors (all green layers are CoFe and red and blue are metal contacts).

certain parts of a CMOS logic circuit with spin logic if the spin logic is better suited for that particular task. Such a spin logic device that is based on the MLG is the spin torque majority gate[19] (STMG). Figure 2.4 shows a cartoon of an in-plane STMG, which consists of four pillars on top of a larger base. Each pillar in combination with the base is a spin valve structure that converts between charge current and spin current. Voltages are applied to the input metal contacts (blue) and the current is measured through the output metal contact (red), all while the base contact (orange) is grounded. The resistance of the output pillar is determined by the majority vote of the input pillars, as in a field-coupled MLG. Alternatively, for an out-of-plane STMG a cross geometry for the base is used, and a pillar is placed on each arm of the cross. Due to non-volatility and re-configurability (as either AND or OR), the STMG may be advantageous in certain circuits.

Another spin logic device that uses purely electrical interconnects is the spin switch[16]. Figure 2.5 shows a cartoon of a spin switch device with the appropriate connections. Designed as a replacement for the CMOS transistor, the spin switch has input and output voltages and a pair of voltage rails (specifically both positive and negative with respect to ground). An applied input voltage passes a current through a spin hall effect metal (blue), which converts charge current to spin current and switches the magnet adjacent to it (green). This magnet is strongly stray field coupled to another magnet separated by an insulator between them (red). This other magnet is part of a spin valve with each of two pillars on top of it. The two pillars are oppositely magnetized so that one spin valve has high resistance while the other has low resistance. The output voltage at the base contact of this structure (orange) thus takes on the value of either voltage rail depending on the base layer magnetization. Switching the voltage rail contacts essentially switches between N and P equivalents. The spin switch can potentially be a low-power non-volatile switch that can also implement reconfigurable logic[16].

A switch design with many similarities to NML is all-spin logic[20] (ASL). ASL also stores bits in nanomagnets, but instead of stray field coupling the magnets are coupled by a non-local spin-transfer torque that flows through a spin-coherent interconnect. Figure 2.6 shows a cartoon of the ASL device with two interconnected bits. Basic operation entails

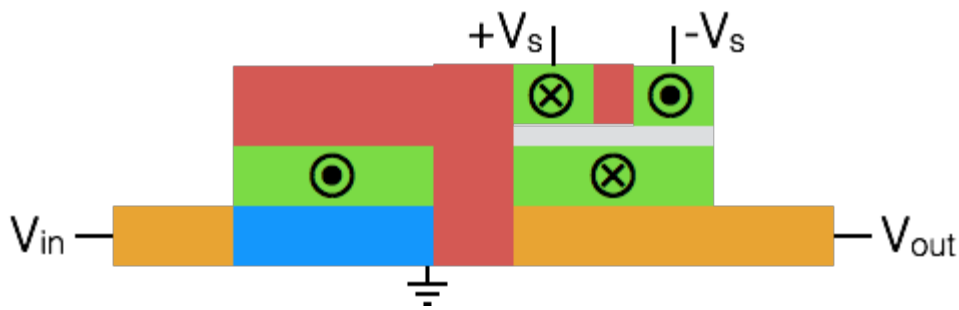

Figure 2. 5: Spin switch with write (left) and read (right) components. The materials are metal contacts (orange), spin hall effect metal (blue), ferromagnet (green), insulator (red), and spin valve spacer (gray). Since the large ferromagnets are strongly coupled, their orientations (black) are opposite each other. Voltage rails (V_s) are usually constant, though can be used as inputs for certain non-Boolean logic operations.

applying clock voltage pulses across one magnet (green, V_1) to generate spin polarization in the interconnect (blue) that switches the other magnet (green) through spin torque. The process is concatenable so that applying another clock voltage pulse across this magnet (V_2) can switch yet another magnet downstream. Isolation layers (red) serve to contain the spin polarization in the region between the two magnets that are intended to be coupled. Tunneling layers (gray) enhance spin injection into the interconnect and inhibit spin absorption from the interconnect. This determines the directionality of the system such that the side with the tunneling layers switches the side without and not vice versa. Structures consisting of 3 input magnets coupled to 1 output can function analogously to an MLG[20]. An obvious advantage of ASL over NML is the added flexibility in choosing the positions of the magnets.

Domain wall logic devices[21] based on current-driven domain wall motion[22] have also been investigated. These devices place a short spin valve on top of a longer magnetic strip containing a single domain wall that separates two regions of opposing magnetization. By applying spin-polarized current (generated by passing charge current through a magnet) through the strip, the domain wall moves and the magnetization under the spin valve can change. Therefore, an output voltage or current is controlled by the direction of current through the strip. Additionally, the domain wall motion requires that a threshold current be reached[21], and so if two inputs contact the strip at either or both ends, binary logic functions can be implemented that depend on the sum or difference of the input currents. Both in-plane and out-of-plane magnets may be used for domain wall logic. Theoretical work[21] predicts low operating voltages but also slow speeds.

Experimental work demonstrating fabricated torque-coupled spin logic devices is somewhat lacking. Moreover, devices using voltage or current as a state variable also inherit the problem of leakage from CMOS transistors. However, we believe that these spin logic systems have at least as much potential as NML if realized devices are consistent with

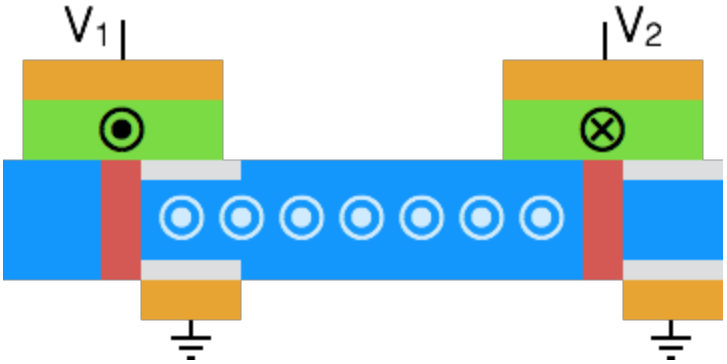

Figure 2. 6: All-spin logic segment with an input magnet (left) and an output magnet (right). The materials are metal contacts (orange), spin-coherent interconnect (blue), ferromagnet (green), spin-isolation layer (red), and spin tunneling layer (gray). Magnetic orientation (black) and spin polarization (white) are shown.

predictions. In general comparison with CMOS, spin logic systems (both field-coupled and torque-coupled) attempt to push non-volatility and potentially low-power switching as advantages while suffering slower speeds as a disadvantage. Thus, for applications that are extremely sensitive to power consumption and not as demanding in performance, spin logic is a promising area of research with efforts that also strongly benefit magnetic memory research.

Chapter 3. Theoretical Models for the Behavior of Ferromagnets

1. The Stoner-Wohlfarth Model

Recent ferromagnetic devices applicable in electronic devices are typically small enough to be considered single-domain. In such magnets, the exchange interactions dominate and the parallel (ferromagnetic) alignment of all spins is energetically favorable. Thus, if we simply assume that all spins in the magnet are exactly parallel so that the magnetization is constant throughout the volume, then the Stoner-Wohlfarth model[23] is valid. The Stoner-Wohlfarth model is purely static (referred to as adiabatic in this work) in the sense that it describes magnets in equilibrium. Figure 3.1 shows a diagram of the canonical model for a magnetic particle with uniaxial anisotropy, in which a particular axis (designated as easy) is energetically favorable. Since u actually indicates an axis rather than a vector, the energy of the interaction between m and u is proportional to $(\hat{m}\cdot\hat{u})(\hat{m}\cdot -\hat{u})$ or $-|\hat{m}\cdot\hat{u}|^2$. On the other hand, B is a true vector and the interaction energy is the Zeeman energy $-\vec{m}\cdot\vec{B}$. Letting K_u be the proportionality constant of the uniaxial anisotropy energy and $\vec{m}=\vec{M}V$ with magnetization M and volume V, the energy density of the particle is:

$$U = -K_u|\hat{M}\cdot\hat{u}|^2 - \vec{M}\cdot\vec{B} \tag{3.1}$$

Using the convention of figure 3.1 with the angular parameterization and letting $\vec{M}=M_S\hat{M}$ we can also rewrite equation 3.1 as:

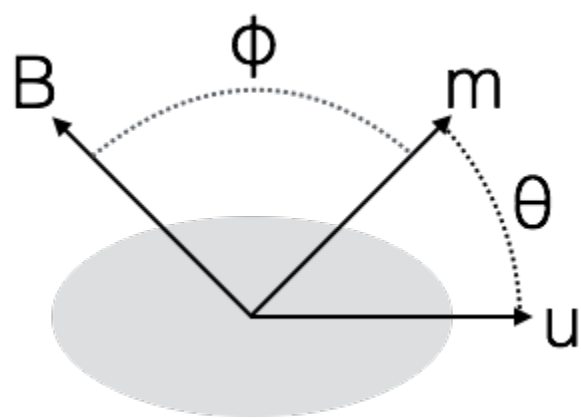

Figure 3. 1: Diagram of Stoner-Wohlfarth uniaxial magnetic particle. The vector u indicates the direction of the easy axis, m indicates the direction of magnetic moment with angle θ to u, and B indicates the direction of applied magnetic induction, with angle ϕ to m.

$$U = -K_u cos^2(\theta) - M_S B cos(\phi) \tag{3.2}$$

Since the magnetization is constant throughout the volume, it only changes by coherent rotation. We can determine the stable equilibrium states of m in an adiabatic approximation by picturing the position (angle) of m as a ball resting on the plot of U and assuming that the ball retains no kinetic energy and thus rolls in the direction −∇U until it comes to rest in a local minimum. The very fundamental ferromagnetic phenomenon of hysteresis can be predicted[23] using this method.

For applications described in this work, the more complex model of adding biaxial anisotropy to a standard Stoner-Wohlfarth magnetic particle has more relevance. Figure 3.2 shows a diagram of the geometry for the special choice of anisotropy axes directions used in this work. The uniaxial easy axis is still u, while the biaxial easy axes are b_1 and b_2. The energy of the interaction between m and b is proportional to:

$$(\hat{m} \cdot \hat{b_1})(\hat{m} \cdot -\hat{b_1})(\hat{m} \cdot \hat{b_2})(\hat{m} \cdot -\hat{b_2}) = |\hat{m} \cdot \hat{b_1}|^2 |\hat{m} \cdot \hat{b_2}|^2 \tag{3.3}$$

Letting K_b be the proportionality constant of the biaxial anisotropy energy, the energy density of the particle is:

$$U = -K_u |\hat{M} \cdot \hat{u}|^2 + K_b |\hat{M} \cdot \hat{b_1}|^2 |\hat{M} \cdot \hat{b_2}|^2 - \vec{M} \cdot \vec{B} \tag{3.4}$$

Using the angular parameterization convention of figure 3.2, we have:

$$\begin{aligned} U &= -K_u cos^2(\theta) + K_b sin^2(\theta) cos^2(\theta) - M_S B cos(\phi) \\ &= -K_u cos^2(\theta) + \frac{K_b}{4} sin^2(2\theta) - M_S B cos(\phi) \end{aligned} \tag{3.5}$$

Finally, adopting the convention used in the rest of this work that all anisotropy energies

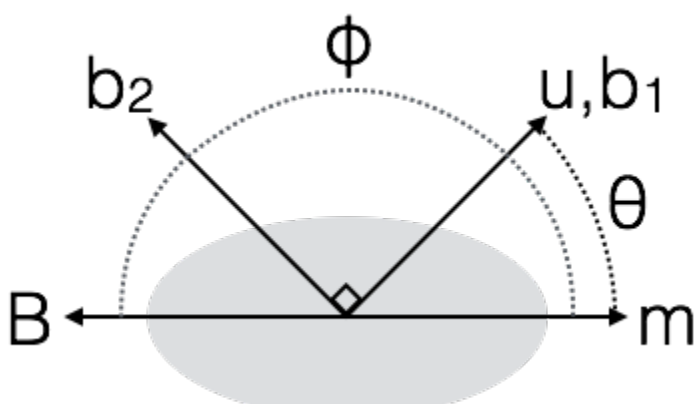

Figure 3. 2: Diagram of Stoner-Wohlfarth magnetic particle with both uniaxial and biaxial anisotropy axes, where the biaxial axes b_1 and b_2 are orthogonal and the uniaxial axis u is parallel to one of the biaxial axes b_1 so that u, b_1, and b_2 are contained in one plane.

are negative and therefore replacing $sin^2(2\theta)$ by $sin^2(2\theta) - 1 = -cos^2(2\theta)$ we end have:

$$U = -K_u cos^2(\theta) - \frac{K_b}{4} cos^2(2\theta) - M_S B cos(\phi) \tag{3.6}$$

Alternatively, we can see the combination of uniaxial and biaxial anisotropy as a second-order power series expansion of a more general anisotropy function. Due to time-reversal symmetry[24], only the even powers of sinusoids can be used in order to satisfy spatial inversion symmetry for the anisotropy energy density $F_{anis}(\theta) = F_{anis}(\theta + \pi)$. We choose F_{anis} to be even so that the expansion is in terms of cos^2. If we align the anisotropy axes as in figure 3.2, then we can drop the phases and we end up with:

$$\begin{aligned} F_{anis} &= K_0 + K_1 cos^2(\theta) + K_2 cos^4(\theta) \\ &= K_0 - \frac{K_2}{4} + (K_1 + K_2) cos^2(\theta) + \frac{K_2}{4} cos^2(2\theta) \end{aligned} \tag{3.7}$$

To match our earlier formulation requires the following substitutions: $K_2 = -K_b$; $K_0 = \frac{-K_b}{4}$; $K_1 = K_b - K_u$.

Finally, we introduce the quantity of anisotropy field[25] H_{anis}. For a purely uniaxial case it is $\mu_0 H_{anis} = \frac{2K_u}{M_S}$ and for a purely biaxial case it is $\mu_0 H_{anis} = \frac{2K_b}{M_S}$. The anisotropy field is the amount of magnetic field needed to either rotate the magnetization to the hard axis or reverse the magnetization along an easy axis (in the process rotating through at least one hard axis since coherent rotation is assumed).

2. The Landau-Lifshitz Equation

The Landau-Lifshitz equation treats the time dynamics of magnetic moments. Unlike the Stoner-Wohlfarth model, this equation also applies to the continuum case when magnetization is non-uniform[26]. This equation expresses both Larmor precession and energy dissipation. For magnetization M, effective magnetic field H_{eff}, gyromagnetic ratio γ, and phenomenological damping constant α, the Landau-Lifshitz equation is:

$$\frac{\partial \vec{M}}{\partial t} = -\frac{\gamma}{1+\alpha^2} \vec{M} \times \vec{H}_{eff} - \frac{\gamma\alpha}{M_S(1+\alpha^2)} \vec{M} \times (\vec{M} \times \vec{H}_{eff}) \tag{3.8}$$

The effective magnetic field has contributions from external fields as well as magnetic anisotropy (both crystalline and shape) and exchange interactions. Equation 3.8 is an explicit form of the completely equivalent (but implicit) equation 3.9, known as the Landau-Lifshitz-Gilbert (LLG) equation:

$$\frac{\partial \vec{M}}{\partial t} = -\gamma \vec{M} \times \vec{H}_{eff} + \frac{\alpha}{M_S} \vec{M} \times \frac{\partial \vec{M}}{\partial t} \tag{3.9}$$

Figure 3.3 shows a cartoon of the vectors and their motion.

To capture the phenomenon of spin-transfer torque (STT) describing the transfer of magnetic moment through charge current, more terms are added to the equation. The result is known as the Landau-Lifshitz-Slonczewski (LLS) equation. For the case of a 2-magnetic-layer device with a spacer (spin valve), the equation describing the free layer magnetization M is[27,28]:

$$\begin{aligned}\frac{\partial \vec{M}}{\partial t} &= -\gamma \vec{M} \times \vec{H}_{eff} + \frac{\alpha}{M_S} \vec{M} \times \frac{\partial \vec{M}}{\partial t} \\ &+ \eta(\hat{M} \cdot \hat{M}_{fix}) \frac{\mu_B I}{eV} \hat{M} \times \left(\hat{M} \times \hat{M}_{fix} + \beta \hat{M}_{fix} \right)\end{aligned} \tag{3.10}$$

Here, M_{fix} is the fixed layer magnetization, I is the charge current, V is the free layer volume, e is the fundamental charge, μ_B is the Bohr magneton, and $\eta(\hat{M} \cdot \hat{M}_{fix}) = \frac{q_+}{A+B(\hat{M}\cdot\hat{M}_{fix})} + \frac{q_-}{A-B(\hat{M}\cdot\hat{M}_{fix})}$ is a function that encapsulates the layer structure into the constants q, A, and B. β is the phenomenological non-adiabaticity constant that describes the inefficiency of spin current absorption. Note that the added adiabatic term has the same form as the damping term in equation 3.8. In a typical spin valve structure, if the effective field aligns with the easy axis (for example out of plane due to interfacial anisotropy) and the fixed layer also aligns with the easy axis, then the adiabatic Slonczewski term can be merged into the damping term (and the non-adiabatic term merged into the precession term) as a change in the magnitude of the effective field. Depending on the direction of charge current and whether the free layer is parallel or antiparallel to the fixed layer, this change in effective

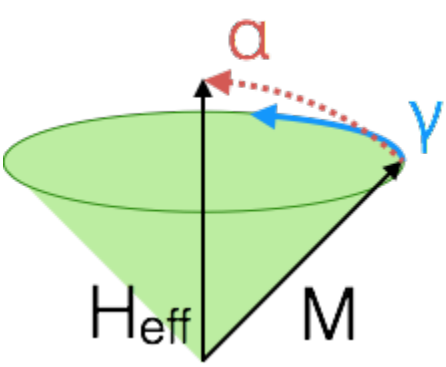

Figure 3. 3: Cartoon of motion of a magnetic moment about an applied field according to the LLG equation. Larmor precession (blue) is around the dark green rim of the cone while Gilbert damping (red) acts to shrink the precession cone to align M and H.

field magnitude can be either positive or negative (and can be to such a degree as to flip the sign of the damping term). For this reason, the added term is also known as the anti-damping term.

In the case of a spin current acting upon a non-uniformly magnetized continuum, the current-driven domain wall motion is described by[29,30]:

$$\begin{aligned}\frac{\partial \vec{M}}{\partial t} &= -\gamma \vec{M} \times \vec{H}_{eff} + \frac{\alpha}{M_S}\vec{M} \times \frac{\partial \vec{M}}{\partial t} \\ &- (\vec{v} \cdot \vec{\nabla})\vec{M} + \frac{\beta}{M_S}\vec{M} \times [(\vec{v} \cdot \vec{\nabla})\vec{M}]\end{aligned} \tag{3.11}$$

Here, v is known as the spin velocity field (with units of velocity). For charge current density J, spin polarization P, and g-factor g, the spin velocity field is:

$$\vec{v} = -\vec{J}P\frac{g\mu_B}{2eM_S} \tag{3.12}$$

The spin polarization is a factor between -1 and +1 calculated with respect to the majority spin direction of the magnet. If spin-up is the majority spin direction then $N_{\uparrow}$ is the number of carriers polarized toward spin-up and:

$$P = \frac{N_\uparrow - N_\downarrow}{N_\uparrow + N_\downarrow} \tag{3.13}$$

Note that equation 3.11 also has a non-adiabatic term that can be combined with the precession term.

Micromagnetics uses discretization of space and time to numerically compute M in a given problem[26,31]. The treatment most often used in this work is a discretized LLG equation acting on a regular grid of finite elements over fixed time steps to produce finite differences. Each grid point (element) is considered to have uniform magnetization (single-domain) of magnitude M_S. To calculate the effective magnetic field, the total energy $E_{total} = E_{exch} + E_{anis} + E_{demag} + E_{zeeman}$ (additional terms such as magnetostriction are of course possible) is first calculated. The combination of the Zeeman energy and anisotropy (both crystalline and interfacial) has the form of the usual Stoner-Wohlfarth energy with $U(M,B,K_i)$ from equation 3.4:

$$E_{anis} + E_{zeeman} = \int_V U(\vec{M}, \vec{B}, K_i)dV \tag{3.14}$$

The volume of integration is the volume of the simulation space. The exchange energy is characterized by the exchange stiffness constant A and favors very gradual spatial variation of magnetization (the constant magnetization assumption of the single-domain model essentially sets exchange energy to 0):

$$E_{exch} = \int_V \frac{A}{M_S^2} \|\vec{\nabla}\vec{M}\|^2 dV \tag{3.15}$$

Here, $\vec{\nabla}\vec{M}$ is the Jacobian matrix and $\|\vec{\nabla}\vec{M}\|^2 = tr\left[(\vec{\nabla}\vec{M})(\vec{\nabla}\vec{M})^T\right]$ is the square of the Frobenius norm. Since each element is single-domain, it is possible to rewrite the exchange energy in another form that is easier to derive the effective field from:

$$E_{exch} = -\int_V \frac{A}{M_S^2} \vec{M} \cdot (\nabla^2 \vec{M}) dV \tag{3.16}$$

Finally, the demagnetizing energy considers the magnetic fields produced by the magnetization and is commonly referred to as shape anisotropy. The demagnetizing field H_D can be found by solving the following Maxwell's equations for the magnetostatic case:

$$\vec{\nabla} \cdot \vec{B}_D = \mu_0 \vec{\nabla} \cdot (\vec{H}_D + \vec{M}) = 0 \tag{3.17}$$

$$\vec{\nabla} \times \vec{H}_D = \vec{J}_f + \frac{\partial \vec{D}}{\partial t} = 0 \tag{3.18}$$

For r as the vector pointing from the integration location to the location of H_D:

$$\vec{H}_D = \frac{-1}{4\pi} \int_V \vec{\nabla} \cdot \vec{M} \frac{\vec{r}}{r^3} dV \tag{3.19}$$

The demagnetizing energy takes the expected form of the Zeeman energy except for a factor of half due to reciprocity:

$$E_{demag} = \frac{-1}{2} \int_V \mu_0 \vec{M} \cdot \vec{H}_D dV \tag{3.20}$$

Once the energy terms are summed to express total energy as a function of M, we can calculate the effective magnetic field as:

$$\begin{aligned} \vec{H}_{eff} &= \frac{-1}{\mu_0} \vec{\nabla}_{\vec{M}} \left(\frac{\partial E_{total}}{\partial V} \right) \\ &= \frac{2A}{\mu_0 M_S^2} \nabla^2 \vec{M} - \frac{1}{\mu_0} \vec{\nabla}_{\vec{M}} U(\vec{M}, \vec{B}, K_i) + \vec{H}_D \end{aligned} \tag{3.21}$$

A few issues arise in optimizing micromagnetic simulations for specific problems. Though it is of course more accurate to use ever-smaller element sizes and time steps, it is also completely impractical given limited computation resources. Instead, spatial grid sizes should be less than the smallest critical length of interest. In nanomagnetism, this is

typically the exchange length so that exchange-related effects can be captured. Time steps should also be smaller than the period of precession about the exchange field. Smaller element sizes demand smaller time steps, as the stronger exchange interactions increase stiffness. If we observe neighboring elements that spontaneously begin oscillating out-of-phase with each other, it typically indicates too large of a time step. Another important issue concerns the choice of damping constant[26]. Though the true (microscopic) phenomenological damping constant α is a material-dependent parameter, the apparent (macroscopic) damping constant α_{app} also depends on grid size. It can be shown using the Cauchy-Schwarz inequality that α_{app} monotonically increases for ever-larger ensembles of spins. Thus, larger grid sizes correspond to larger α_{app} values.

3. The Addition of Thermal Effects

In the absence of thermal fluctuations, a Stoner-Wohlfarth particle would seek and stay at the local energy minimum. However, thermal fluctuations can randomly switch the particle by supplying it with the energy pass over one of its energy barriers. If a single-domain magnet has exceptionally small energy barriers, this spontaneous switching may happen so often that in the time scales of interest it appears to have zero magnetic moment (more precisely, the average magnetic moment integrated over the time period of interest is 0). This phenomenon is called superparamagnetism. The intuition is that larger energy barriers are needed to make single-domain magnets more thermally stable. The formal statement of this is the Néel-Arrhenius equation[32,33]:

$$\tau_N = \tau_0 e^{\frac{E_B}{k_B T}} \tag{3.22}$$

T is the temperature, k_B is the Boltzmann constant, E_B is the energy barrier, τ_N is the average time between thermally-driven switching events, and τ_0 is a phenomenological characteristic time known as the attempt period and is typically in the range 0.1 to 1 ns. In the magnetic memory industry, a common metric is the data retention time, which is equivalent to τ_N. For long-term storage applications such as hard disks, the target is typically 10 years[34], which typically needs an E_B of $60k_BT$. In the purely uniaxial case, the energy barrier is simply $E_B = K_uV$. For the combination of uniaxial and biaxial anisotropy according to equation 3.6 with B = 0, an additional energy barrier forms when $K_b > K_u$ such that local minimums form and the two biaxial easy axes effectively become a major and a minor easy axis. The energy barrier $E_{B\downarrow}$ seen going from the minor to the major easy axis is not equal to the energy barrier $E_{B\uparrow}$ seen going from the major to the minor easy axis:

$$E_{B\downarrow} = \frac{(K_b - K_u)^2}{4K_b} V \tag{3.23}$$

$$E_{B\uparrow} = \frac{(K_b + K_u)^2}{4K_b} V \tag{3.24}$$

The time dynamics of a magnetic continuum at finite temperature is usually treated by adapting the Landau-Lifshitz equations as a stochastic differential equation. The adaptation most relevant to this work is the stochastic LLG equation written as a Langevin equation where a random field is added to the effective field:

$$\frac{\partial \vec{M}}{\partial t} = -\gamma \vec{M} \times [\vec{H}_{eff} + \vec{H}_{noise}(t)] + \frac{\alpha}{M_S} \vec{M} \times \frac{\partial \vec{M}}{\partial t} \tag{3.25}$$

$H_{noise}(t)$ is a Gaussian white noise term that satisfies expectation and correlation properties[31] according to the Einstein relation (fluctuation dissipation theorem):

$$\langle \vec{H}_{noise}(\vec{r}, t) \rangle = 0 \tag{3.26}$$

$$\langle H_{noise,i}(\vec{r}, t) H_{noise,j}(\vec{r'}, t') \rangle = \frac{2k_B T \alpha}{\mu_0 M_S \gamma} \delta_{ij} \delta(\vec{r} - \vec{r'}) \delta(t - t') \tag{3.27}$$

Equation 3.27 states that the noise field is uncorrelated in space and time and uncorrelated between orthogonal spatial components. The discretized version of this treatment is used in micromagnetic simulations in this work.

We have introduced the basic physical models for analyzing the ferromagnetic systems in this work. Many methods used in this work are extensions of the concepts introduced here. However, some of these extensions are not necessarily straightforward, with details that are outside the scope of this work. An example is the discretization procedures used to be able to perform numerical simulations[35]. Further information on these procedures can be found by reading the documentation of the respective software[36].

Chapter 4. Configurational Anisotropy in Nearly-Single-Domain Magnets

1. Edges and Corners of Nearly-Single-Domain Magnets

It is well-known[37] that bulk magnets form domain patterns in order to minimize their demagnetizing energy. As the size of the magnets decrease, the exchange energy increasingly dominates until the magnet is an isolated single spin (an electron). At this point, both the exchange energy and demagnetizing energy vanish. Single-domain nanomagnets are thus an approximation, and some domain patterns are preserved as well (though patterns that change gradually in space are far more energetically favorable to the point where it may be difficult to use the concepts of domains and domain walls in the traditional sense). In this more exact treatment where the magnetization of nearly-single-domain magnets is still spatially non-uniform, the shape anisotropy due to the competition of demagnetizing energy and exchange energy is called configurational anisotropy[38].

It was found by micromagnetic simulation[39] that for square thin-film nanomagnets made of permalloy (an alloy of 80% nickel and 20% iron that has no crystalline anisotropy), the larger sizes had the vortex energetic ground state. As the sizes were reduced and the nanomagnets became nearly-single-domain, the buckle became the ground state. Further reduction toward smaller sizes produced the leaf and flower states. Figure 4.1 shows diagrams that qualitatively depict the magnetic orientations of the states. Most importantly, the leaf configuration has "convex" magnetization curvature with net moment along the diagonal of the square, while the flower configuration has "concave" magnetization curvature with net moment along the side of the square. Whether the leaf or the flower becomes the energetic ground state is determined by the aspect ratio, which is the ratio of the thickness to the side length. It was found[25] that for permalloy, an aspect ratio of around 2.7 is the boundary between the two states up to a critical point near 45 nm side length and 17 nm thickness, where the buckle state enters the phase space. Below around 12 nm thickness, aspect ratios less than the boundary produce the flower state while aspect ratios more than the boundary produce the leaf state. For thicker squares, the boundary is not sharp but instead forms a linear combination of both states.

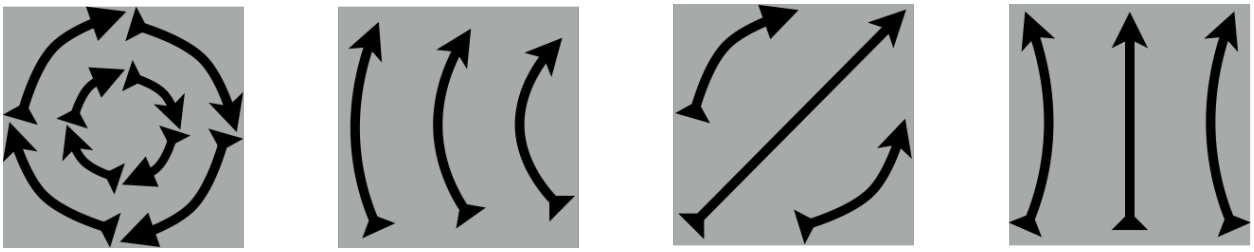

Figure 4. 1: The vortex, buckle, leaf, and flower configurations (left to right).

The phase boundary between ground states can be explained[25] by considering both leaf and flower states as perturbations to a true single-domain state. The regions that are perturbed more develop a larger magnetization difference compared to the single-domain state. These are also the regions that contribute more to the total demagnetizing energy. For the flower, these are the corners. For the leaf, these are the middles of the edges. It follows that removing these configuration-defining regions should make the configuration more unfavorable. Since the flower and leaf have different high-contribution regions, it should be possible to bias a square nanomagnet toward one of the two configurations by removing magnetic material from said regions. To induce the flower, we remove the straight edges. To induce the leaf, we remove the sharp corners. Figure 4.2 shows the magnetic configuration of such shapes. The ground states show curvature, while the unfavorable states are forced using an applied magnetic field and are therefore single-domain.

Another point of view to explain the ground states is to solve equations 3.17 and 3.18 by introducing the magnetic scalar potential and Poisson's equation for the potential[24]:

$$\vec{H} = -\vec{\nabla} A \tag{4.1}$$

$$\nabla^2 A = \vec{\nabla} \cdot \vec{M} \tag{4.2}$$

Equation 4.2 has a form that suggests $\vec{\nabla} \cdot \vec{M}$ is naïvely analogous to magnetic charge density. For the surface normal vector n to the magnet, the boundary conditions (obtained from continuity) and solution are:

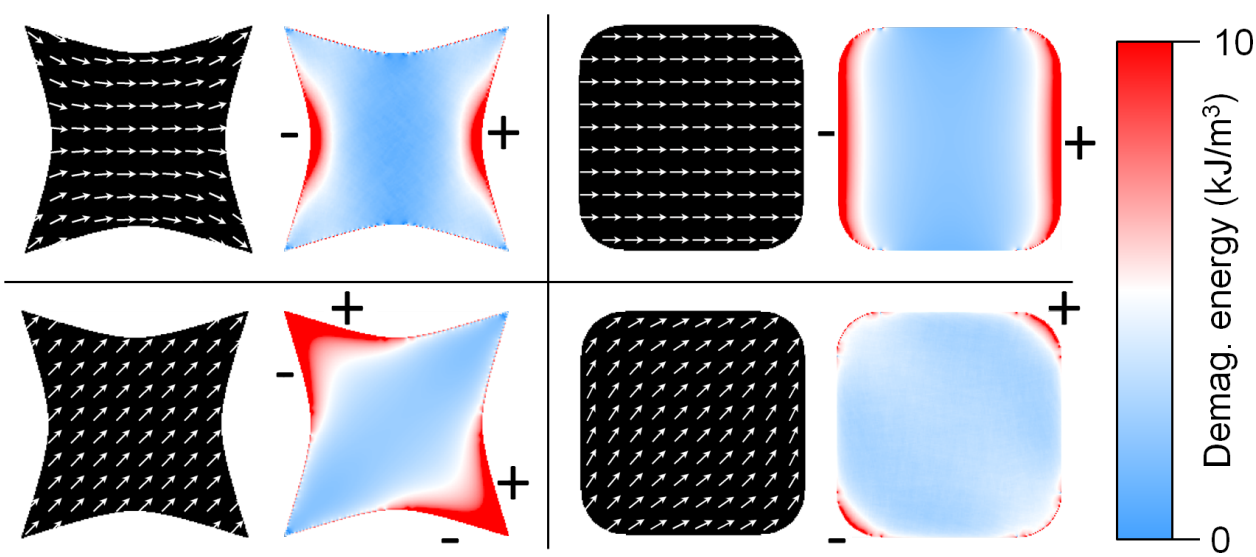

Figure 4. 2: Magnetization configuration and demagnetizing energy (or magnetic charge density) for concave-sided squares (left) and convex-sided squares (right) in the side-aligned configuration (top) and the diagonal-aligned configuration (bottom).

$$\frac{\partial A_{inside}}{\partial n} = \frac{\partial A_{outside}}{\partial n} + \vec{M} \cdot \hat{n} \tag{4.3}$$

$$A(\vec{r}) = \frac{-1}{4\pi} \int_V \frac{\vec{\nabla}_{\vec{r'}} \cdot \vec{M}(\vec{r'})}{|\vec{r} - \vec{r'}|} dV' + \frac{1}{4\pi} \int_S \frac{\hat{n}(\vec{r'}) \cdot \vec{M}(\vec{r'})}{|\vec{r} - \vec{r'}|} dS' \tag{4.4}$$

Here, S is the surface of the magnet and V is the enclosed volume. Analogous to a macroscopic bar magnet with north and south poles, the contributions to the potential can be thought of as microscopic poles. The first and second terms of equation 4.4 are the volume and surface poles, respectively. The configuration that minimizes demagnetizing energy also minimizes the density of poles. The color-mapped diagrams[18] in figure 4.2 show that the forced single-domain configurations produce greater densities of surface poles. Note that these dense-pole regions are the same as the high-contribution regions (from the surface of which we removed magnetic material) mentioned earlier.

The strength of configurational anisotropy was found[18,38] to be fairly strong in nanomagnets: on the order of a few hundred Oe in anisotropy field, and tunable as well by varying shape and dimensions. The potential applications include nanomagnetic memory and logic devices where control over anisotropy is needed or more complex anisotropy is desired.

2. Simulation Study of Configurational Phase Space

We can quantitatively analyze configurational anisotropy by micromagnetic simulation. In this work, we use the Object-Oriented Micro-Magnetic Framework (OOMMF), which is an open-source finite element simulator[36]. A common way to define the elements in OOMMF is to use an atlas, which is an image mapping of mesh cells. Figure 4.3 shows examples of atlases we used to map the adjusted square-like shapes designed for inducing the flower and leaf configurations. Each pixel represents a mesh cell, the colors differentiate properties of the cell (in this case, black or gray is permalloy while white is vacuum), and the image is extruded in the out-of-plane direction to form the mesh (so that each position along the thickness axis looks alike). We started with a 27 nm x 27 nm x 10 nm square magnet (each mesh cell is 1 nm x 1 nm x 1 nm) so that its aspect ratio is 2.7, the nominal phase space boundary between the flower and leaf configurations. Then we removed triangular sections from the middles of the edges and the corners, respectively for concave and convex shapes. Each section removed is an isosceles right triangle with altitude n pixels (for the edges this is the bisecting altitude, while for the corners this is the side altitude) and is recolored to white, where n is a parameter representing the degree of tuning. The black atlases in the figure have n = 2, while the gray atlases have n = 4. Though

these designs do not optimally minimize demagnetizing energy, they are simple to define especially in the context of discrete cubic elements.

Following the simulation script in appendix A.1, we chose standard permalloy parameters: saturation magnetization of 8 x 10^5 A/m and exchange stiffness of 13 x 10^{-12} J/m. An apparent damping constant of 0.02 was used (0.01 is usually considered the true damping constant of permalloy), though larger values would also have worked since the simulations are purely relaxation toward a ground state. We started each simulation with the magnetization uniformly oriented toward an angle of $\frac{\pi}{8}$ with respect to the edge (the angle halfway between the net magnetic moments of the flower and leaf configurations). We then allowed the system to relax at zero temperature until the maximum rate of change of any mesh cell's magnetization is less than 1 degree per nanosecond. Once this point was reached, the simulation terminated and stored the result as the ground state. We performed a large number of these simulations in a parameter spaced that included different values of n for both concave and convex shapes as well as different thicknesses varying in steps of 1 nm. To better parallelize the simulations for single-threaded OOMMF installations on multi-core processors, we used the script in appendix C.1 as a launcher for the simulations.

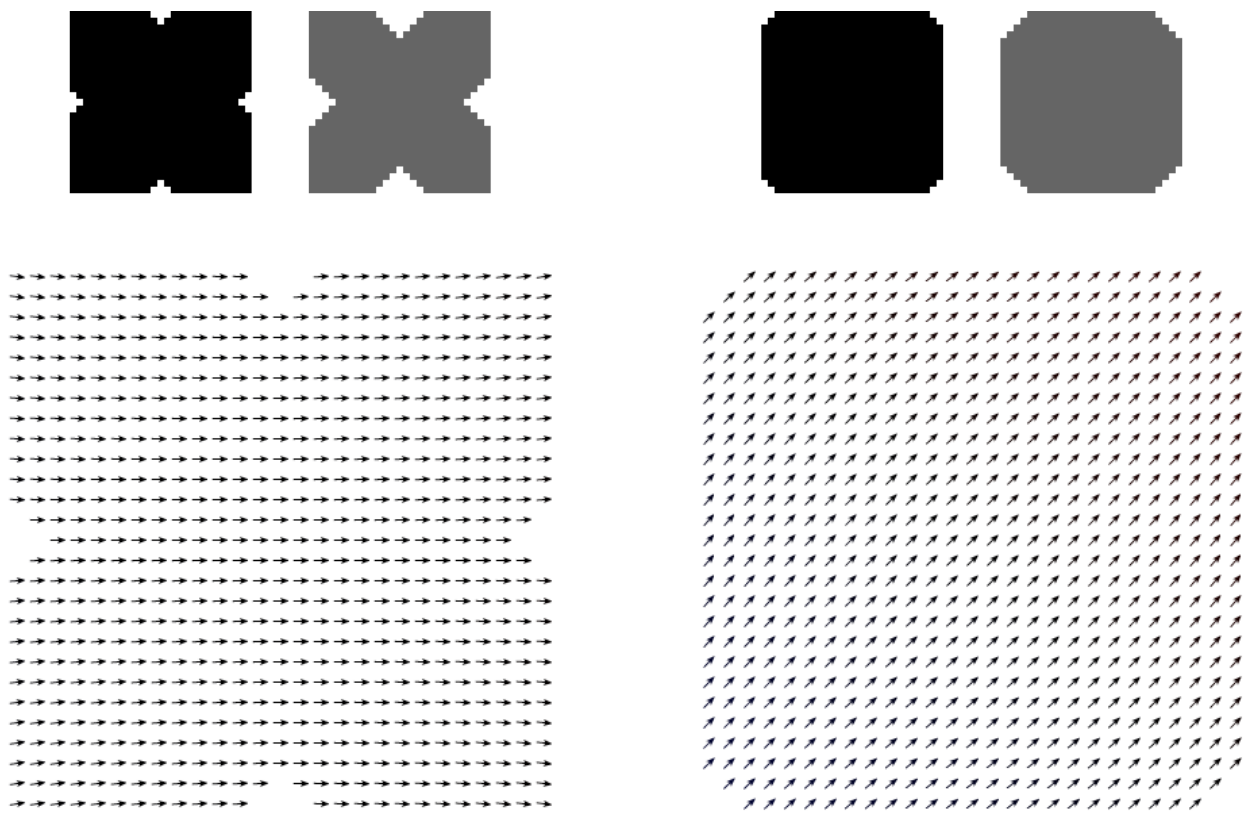

Figure 4. 3: OOMMF simulations for shapes that induce the flower (left half) and the leaf (right half). The ground state magnetization configurations (bottom) and atlases (top, black) as well as atlases for stronger effects (top, gray) are shown.

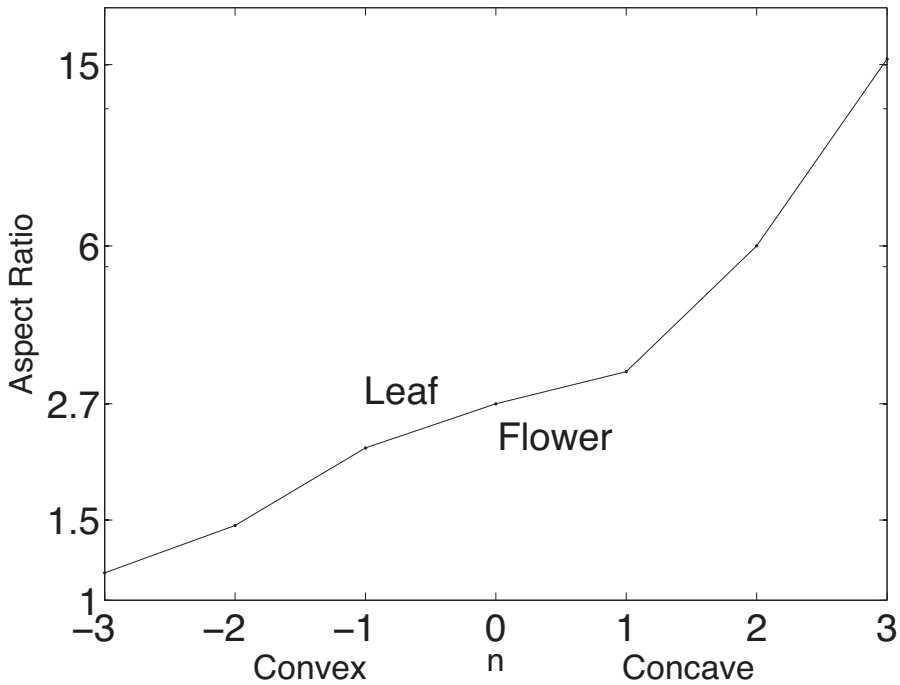

Figure 4. 4: Phase space diagram for convex and concave adjustments of squares with aspect ratio equal to the side length divided by the thickness. The independent parameter n is related to the number of mesh cells removed from the square.

Figure 4.4 shows how the configuration phase space changes when the square-like shape is tuned in the manner described above. The point at n = 0 represents a perfect square and has a phase boundary at 2.7 aspect ratio, as expected. The figure shows that at this aspect ratio, making the shape more concave induces the flower state while making the shape more convex induces the leaf state. In addition, the phase boundary changes with n so that in general, the flower is more favorable for concave shapes while the leaf is more favorable for convex shapes. Using this technique, we can engineer the orientation of a nanomagnet's anisotropy axes for various thicknesses.

3. Design of Nanomagnet Shapes for Nanomagnetic Logic

As is, the adjusted square-like shapes used in section 4.2 have applications in magnetic memory due to the ability to store four distinct states (two bits) and the ability to engineer the energy barrier height. For magnetic logic, the ability to combine configurational anisotropy with more conventional shape anisotropy has important applications. For example, we can use a flower configuration-inducing shape that is also elongated along one of the easy axes. This still provides two orthogonal axes along which stable flower configurations form, but one such axis is easier than the other. In other words, this combines a uniaxial shape anisotropy with a biaxial configurational anisotropy.

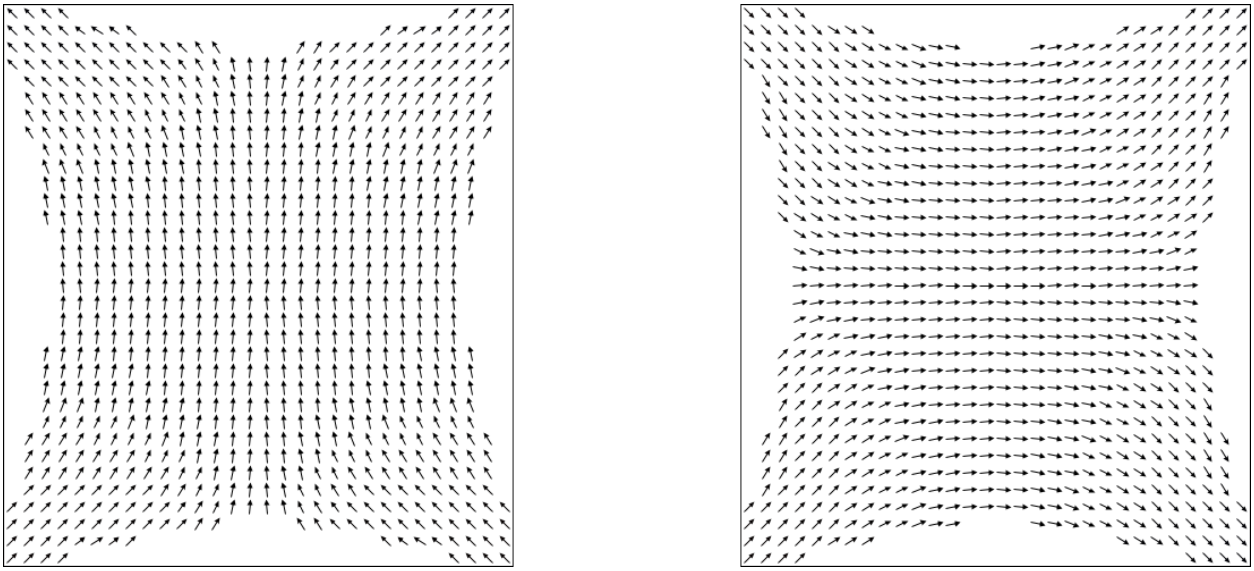

Figure 4. 5: Flower magnetization configurations for elongated concave nanomagnet found by OOMMF along the strong easy axis (left) and the weak easy axis (right).

The configurations of such a shape are seen in figure 4.5. The application of similar shapes is to provide meta-stability for a between-state that is neither pointing up nor down. This state would therefore be digitally equivalent to a state that represents no binary information. This application is further described in section 5.1, which refers to it as the null state.

Figure B.1 shows a simplified version of the same concept intended for easier nanofabrication. The 4 protrusions from the rectangle can be separately exposed with higher dosage in order to better reproduce the desired shape. The figure also shows a biased version of the shape that introduces an asymmetry so that the easy axes are not orthogonal. This is achieved by adding two extra protrusions (corners) on opposite sides in an inversion-symmetric manner. A similar effect can be achieved for the other easy axis by making one protrusion different from the other (and taking care of the opposite side in an inversion-symmetric manner). These shapes with effectively non-orthogonal easy axes find applications in fixed input magnets[40] and biased magnets (which can be used in the B-gate construct[8]) for NML.

4. Simulation Extraction of Anisotropy Constants

For use in designing NML, it would be useful to characterize nanomagnets with complex anisotropies in terms of more simple parameters. One such example is the combination of uniaxial and biaxial anisotropy mentioned in section 4.3. Though the anisotropy profile is more complicated than purely uniaxial and biaxial, the approximation can be sufficient to engineer with. There are several ways to make this approximation. For

example, we can take up to second order the series expansion terms of the anisotropy profile. Though this may be the most natural way, we take a different approach here.

Given an energy density expression as in equation 3.6, we first assume that the magnet rests along the weak easy axis (which exists if $K_b > K_u$). We then find the magnitude of the applied magnetic field along the direction of the strong easy axis needed to switch the magnet. In the adiabatic model, this occurs when the energy density is purely non-increasing along the entire path taken from weak easy axis to strong easy axis. A saddle point (unstable equilibrium) forms along the path for the smallest field magnitude needed. If the energy density U is parameterized in terms of only the angle θ of the magnetization, then we can solve for the conditions necessary for this point by:

$$\frac{\partial U(\theta)}{\partial \theta} = 0 \tag{4.5}$$

$$\frac{\partial^2 U(\theta)}{\partial \theta^2} = 0 \tag{4.6}$$

The switching magnetic induction B_S required for the magnet becomes:

$$B_S = \frac{4}{3M_S}\sqrt{\frac{(K_b - K_u)^3}{6K_b}} \tag{4.7}$$

Note that the requirement $K_b > K_u$ appears naturally if B_S must be real.

Now assuming that the magnet rests along the strong easy axis, we find the magnitude of the applied magnetic field along the direction of the weak easy axis needed to switch the magnet. By the same arguments and methods, we find that the switching magnetic induction B_C required for the magnet becomes:

$$B_C = \frac{4}{3M_S}\sqrt{\frac{(K_b + K_u)^3}{6K_b}} \tag{4.8}$$

Unlike the series expansion approximation described above, this approximation preserves the exact switching field values while being less accurate about the overall shape of the anisotropy profile. We believe that this is a better approximation for engineering

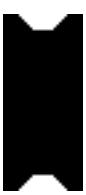

Figure 4. 6: OOMMF atlas design used to find switching field magnitudes.

NML as switching fields are fairly fundamental and pervasive design parameters. Now given the expressions for these switching fields in terms of anisotropy constants, we used OOMMF to find the switching fields and then invert equations 4.7 and 4.8 numerically to solve for the anisotropy constants. We used atlases similar to that of figure 4.6 but of varying lengths (the vertical dimension). This design closely resembles the lithography mask design given in figure B.1 (concave magnet) but with angled inside edges of the protrusions. This feature more accurately resembles the true shape of the magnets after nanofabrication. Each simulated magnet was 12 nm thick, 150 nm wide, and the length varied from 300 nm to 510 nm. Standard permalloy material parameters and zero temperature were used. We followed the simulation script of appendix A.2 which used the following procedure: first initialize the magnetization along the assumed initial state and allow it to equilibrate to form a configuration, then apply the switching field and allow it to equilibrate, and finally remove the field and allow it to equilibrate. We varied the magnitude of the applied field in a series of simulations for each value of magnet length to find the smallest field magnitude that produces a switched final state.

Figure 4.7 plots the switching field magnitudes for the range of magnet lengths simulated. For the switch from weak easy to strong easy axis (blue), the values are accurate to 0.1 mT. For the switch from strong easy to weak easy axis (red), the values are accurate to 1 mT. The values themselves show that it may take nearly 50 mT to reset (or clock as section 5.1 refers to it) nanomagnets of this geometry, while up to 4 mT of stray field coupling may be required for them to switch each other. As the processes of resetting

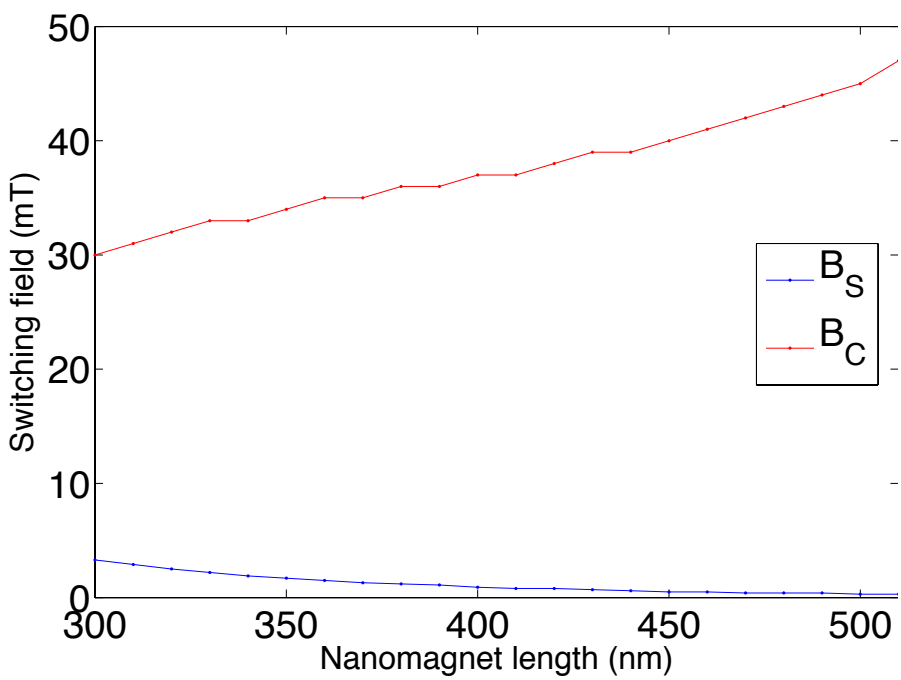

Figure 4. 7: Switching field magnitudes for magnets of atlas design from figure 4.6 with various lengths. B_S switches from weak easy to strong easy axis and B_C vice versa.

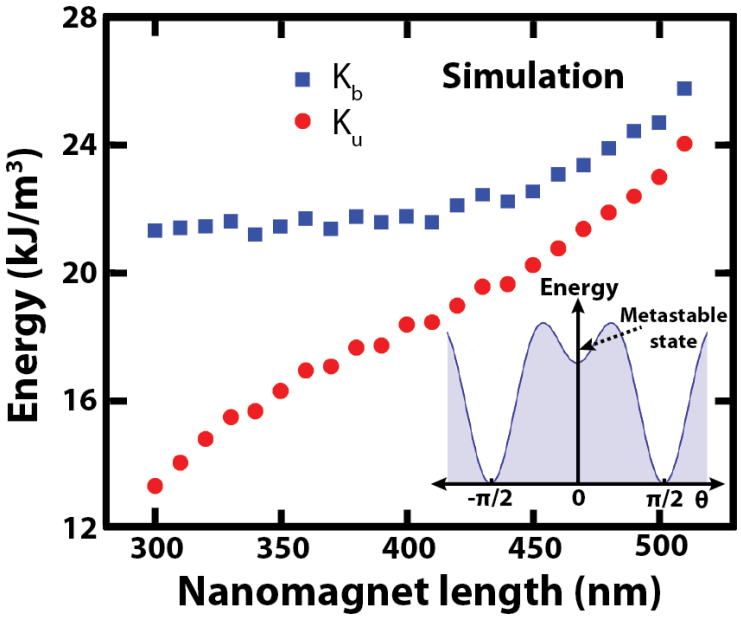

Figure 4. 8: Effective anisotropy constants for magnets of atlas design from figure 4.6.

and magnet-to-magnet coupling are very central to NML, these numbers are useful for designing NML systems. We chose to use these same nanomagnet dimensions in our experimental work.

Figure 4.8 shows the anisotropy constant values calculated from the values in figure 4.7. For magnets shorter than 450 nm in length, the biaxial anisotropy increases very slowly with length while the uniaxial anisotropy increases much more rapidly with length. This follows the intuition that longer magnets have more uniaxial shape anisotropy, while the biaxial configurational anisotropy is determined more by the geometry of the edge cutouts. For magnets longer than 450 nm, we believe the approximation may start to break down as the anisotropy constant values approach each other.

5. Magneto-Optic Kerr Effect

We investigated the net anisotropy of ensembles of nanomagnets using the magneto-optic Kerr effect (MOKE). The magnetization of a material affects its birefringence. MOKE measures the portion of this linear in magnetization using the reflection geometry. We will present two treatments that consider different perspectives but result in the same effect. Consider for a magnetic material the relations for Larmor precession and magnetic auxiliary fields ($\bar{\bar{\mu}}$ denotes a 2nd rank tensor):

$$\frac{\partial \vec{M}}{\partial t} = -\gamma \vec{M} \times \vec{H} \tag{4.9}$$

$$\vec{B} = \mu_0(\vec{H} + \vec{M}) = \overline{\overline{\mu}}\vec{H} \tag{4.10}$$

Assuming that both M and H take the form of a static term (parallel to each other as expected in equilibrium) superposed with a plane wave[41], equations 4.9 and 4.10 can be explicitly solved to first order in the plane wave term for the permeability tensor. Alternatively, consider the electric auxiliary field relation and the expansion of the polarization density to first order in magnetic field:

$$\vec{D} = \epsilon_0\vec{E} + \vec{P} = \overline{\overline{\epsilon}}\vec{E} \tag{4.11}$$

$$\vec{P} = \epsilon_0\chi_0\vec{E} + \epsilon_0\mu_0\chi_1\frac{\partial\vec{E}}{\partial t} \times \vec{H} \tag{4.12}$$

In equation 4.12, the form of the term that is first order in H is determined by time-reversal symmetry[24]. Substituting this equation into equation 4.11 can explicitly solve for the permittivity tensor.

In either perspective, if we use time-harmonic forms to replace the time derivatives, we arrive at a Hermitian constitutive tensor. In general, diagonalizing this tensor gives a basis of complex eigenvectors corresponding to the principal axes (complex components signifying elliptically polarized beams) and real eigenvalues corresponding to the permeability or permittivity experienced by these principal polarizations. For the example cases of the perspectives described above, we may for simplicity choose the z direction for the static magnetic field to produce a tensor of the form:

$$\{\overline{\overline{\mu}}, \overline{\overline{\epsilon}}\} = \begin{pmatrix} r_1 & +\mathbf{i}r_3 & 0 \\ -\mathbf{i}r_3 & r_1 & 0 \\ 0 & 0 & r_2 \end{pmatrix} \tag{4.13}$$

Here, r_i are real numbers. The principal axes are the z axis and a pair of circularly polarized beams of opposite helicity. Thus, for a normally incident linearly polarized beam, we can decompose it in terms of the circularly polarized basis. The two basis components experience different phase velocities for their respective eigenvalues μ_λ and ε_λ:

$$|\vec{v}_{ph,\lambda}| = \frac{1}{\sqrt{\epsilon_\lambda\mu_\lambda}} \tag{4.14}$$

After reflection, the beam is still linearly polarized, but the phase difference accumulated between the two circularly polarized components result in an effective rotation of the polarization axis (the Kerr rotation). If conductivity is introduced so that the material has loss, the amplitude difference accumulated result in an effective polarization ellipticity change (the Kerr ellipticity).

We fabricated arrays of concave square nanomagnets by electron beam lithography, permalloy and aluminum evaporation, and lift-off in Remover PG onto a silicon substrate. The shapes were nominally 100 nm x 100 nm laterally and varied in permalloy thickness from 10 nm to 15 nm. The aluminum capping layer thickness was kept constant at 2 nm. The spacing between magnets (periodicity) was 600 nm, which was far enough so that stray field interactions were negligible. Various degrees of concavity were fabricated, roughly corresponding to the parameter n from section 4.2. In this section, the average distance between the middle of a concave square's edge and the closest point on its bounding square is called the concavity depth. Figure 4.9 shows a scanning electron micrograph (SEM) of some sample structures. Since the sizes of the structures were well below the diffraction limit, MOKE measurements probed the average properties of the shapes.

Figure 4.10 shows a diagram of our MOKE apparatus. Many details about this apparatus are provided in another work[42] and we will only give an overview. A linearly polarized laser beam was incident on the magnetic sample at an angle (so as to form a plane of incidence and reflection) and the magnetization was in the plane of the sample. The longitudinal and transverse components of magnetization produced polarization and reflectivity changes, respectively. The photo-elastic modulator reduced noise as well as separated the rotation and ellipticity components. By using a lock-in amplifier at the modulation frequency, we measured the Kerr ellipticity corresponding to the longitudinal magnetization component.

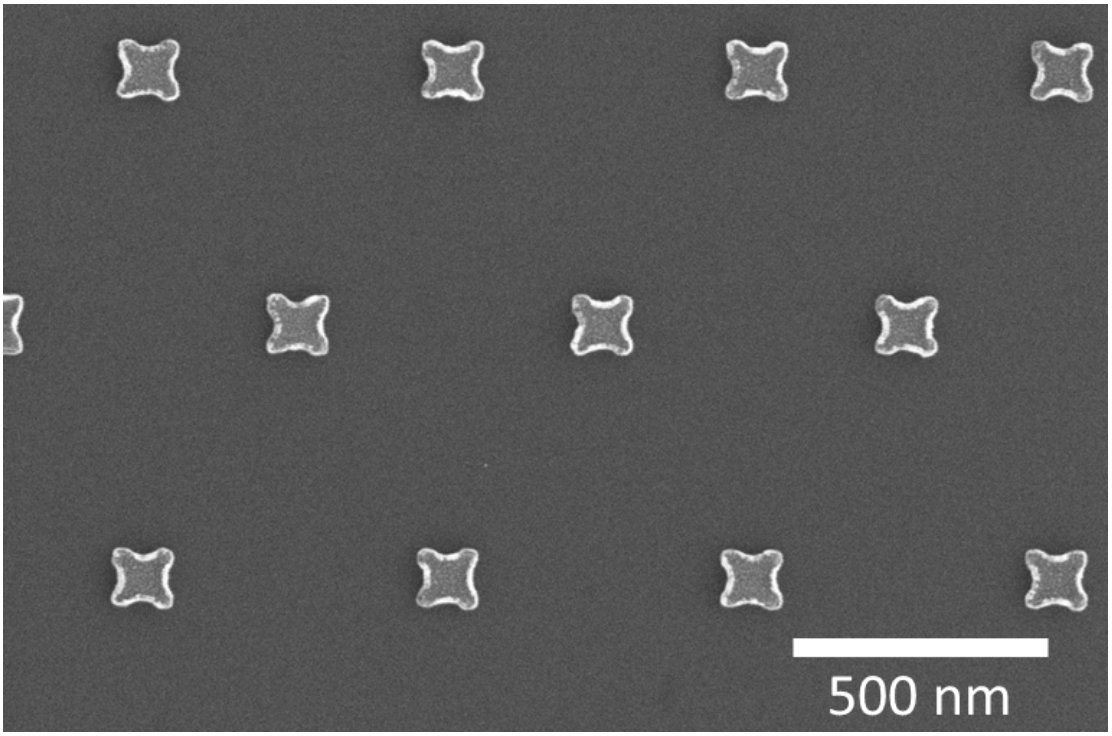

Figure 4. 9: SEM of a part of an array of permalloy concave squares on silicon.

We also introduced a modulation of the applied magnetic field as part of the modulated field magneto-optic anisometry (MFMA) technique[38] used to specifically study configurational anisotropy. We applied a large static field along the direction of transverse MOKE sensitivity, and also applied a small alternating field along the direction of longitudinal MOKE sensitivity. The static field aligned the magnetization parallel to it while the alternating field 'wiggled' the magnetization around this alignment. The more locally stable (steeper energy well) this alignment was, the less the magnetization wiggled. Therefore, the demodulation of the longitudinal MOKE signal with respect to the alternating field frequency was inversely related to the curvature of the anisotropy function along the direction of the static field. Stepping the rotation of the sample around a half circle (the other half is determined by time-reversal symmetry as described in section 3.1) and measuring this curvature at each point resulted in an angular anisotropy profile. In this section, these profiles are plotted as normalized reciprocals of the measured signal, so that larger values represent greater anisotropy curvature and thus greater stability. In simple cases, plot maxima are the easy axes and plot minima are the hard axes.

Figure 4.11 plots the anisotropy profiles for various nanomagnet thicknesses and concavity depths[18]. Particularly noteworthy are the leaf-to-flower transition as thickness increased past 12.5 nm for the 5 nm concavity case, and the leaf-to-flower transition as the concavity increased past 5 nm. These two trends reflect those in figure 4.4. This method of using edge indents to influence configurational anisotropy obviously applies toward shapes beyond squares. Figure 4.12 shows an example for equilateral triangles of side length 120 nm[18]. The anisotropy profile inverts when the edge indents

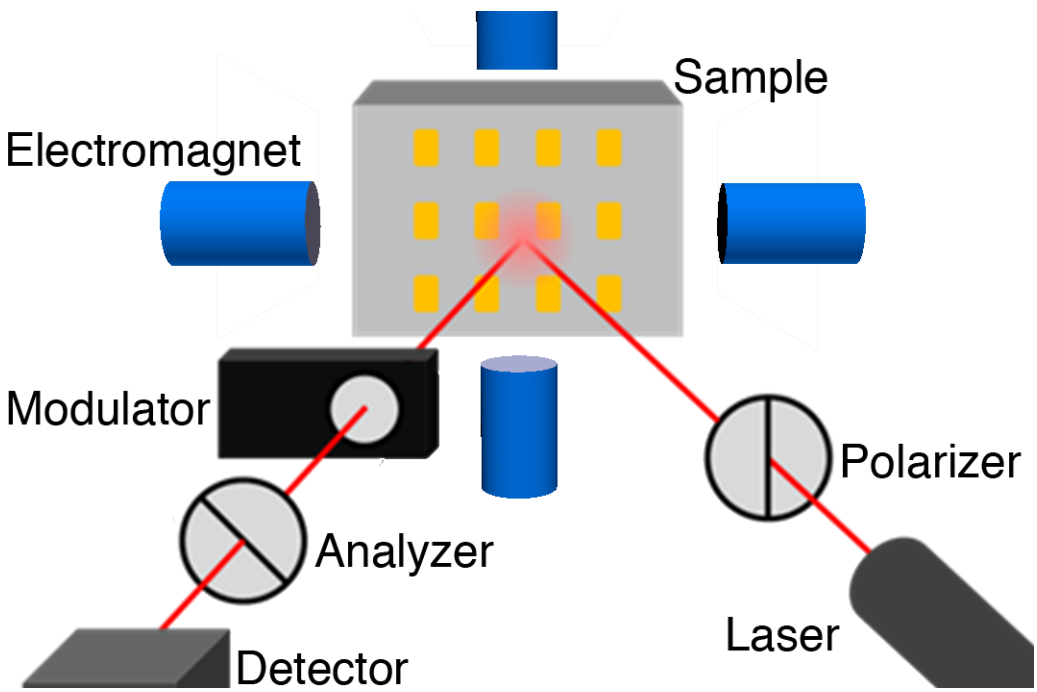

Figure 4. 10: Cartoon of MOKE experimental setup used to measure nanomagnet arrays.

are introduced so that magnetizations tend to align into the corners instead of along the edges.

Along hard axes (where the anisotropy function curvature is negative in the absence of externally applied fields), the anisotropy field can be quantitatively measured. Applying a field B along a hard axis satisfies:

$$\frac{\partial}{\partial\theta}\left[U(\theta) - M_S B\cos(\theta)\right]\Big|_{\theta=0} = 0 \tag{4.15}$$

If the field is the anisotropy field B_{anis}, then the following is also satisfied:

$$\frac{\partial^2}{\partial\theta^2}\left[U(\theta) - M_S B_{anis}\cos(\theta)\right]\Big|_{\theta=0} = 0 \tag{4.16}$$

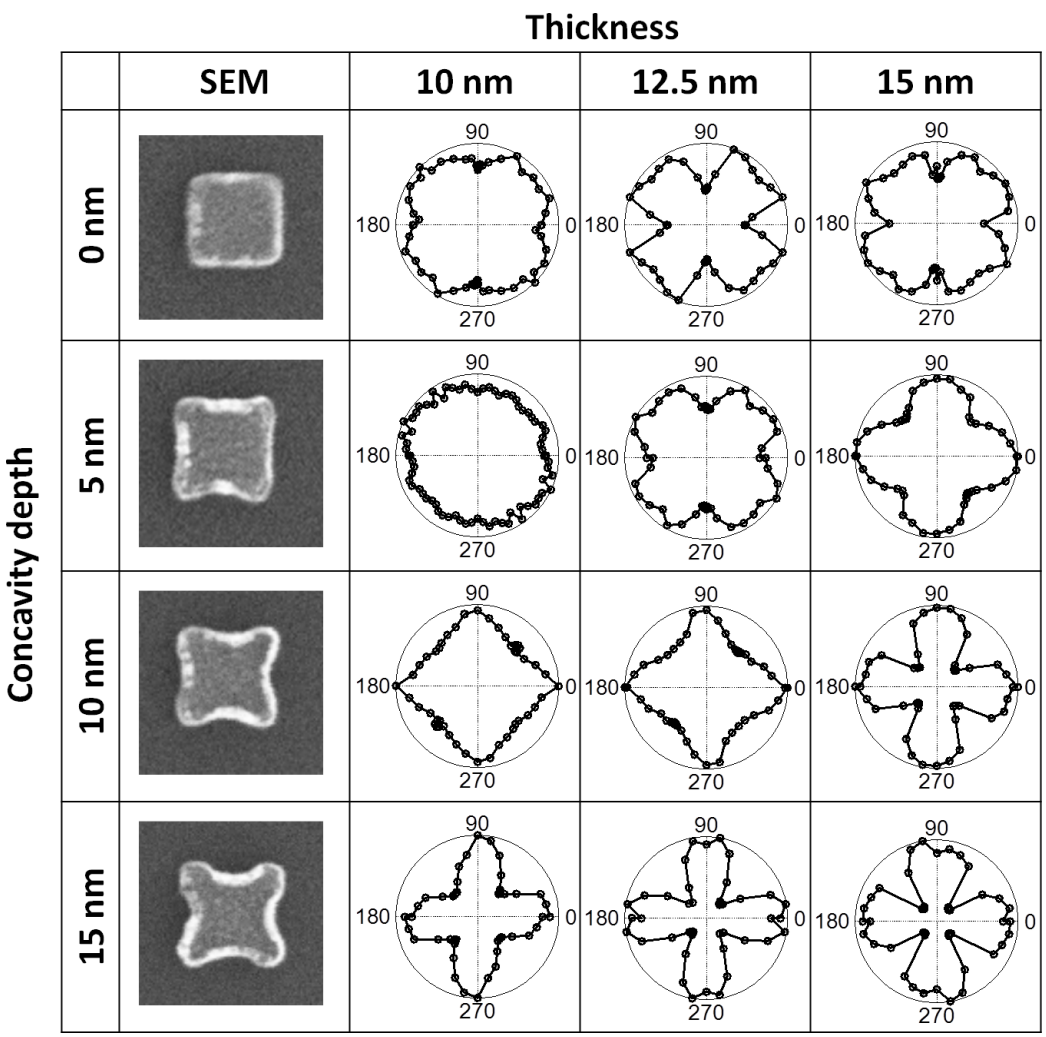

Figure 4. 11: Anisotropy profile table for various concave square nanomagnet arrays measured by MFMA. Maxima indicate easy axes and minima indicate hard axes.

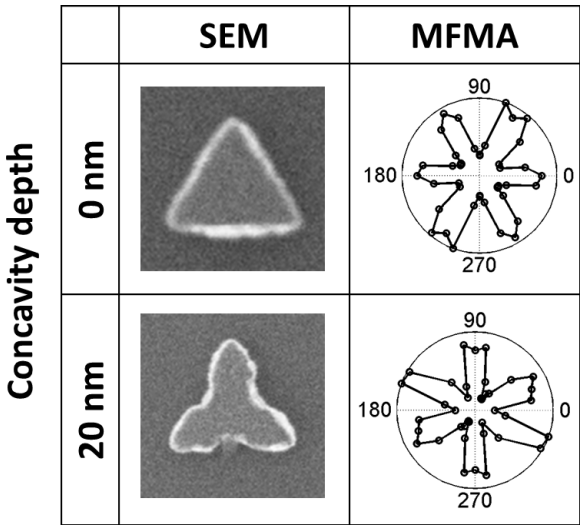

Figure 4. 12: Anisotropy profile table for various concave triangle nanomagnet arrays.

The MFMA magnitude should peak when the applied static field is equal to the anisotropy field since the MFMA response goes as[38]:

$$\left[\frac{\partial^2 U(\theta)}{\partial \theta^2} + M_S B_{anis}\right]^{-1} \tag{4.17}$$

An applied field larger than the anisotropy field results in a positive anisotropy function curvature along that direction. The stronger this static field, the more positive the curvature, which decreases the measured MFMA signal. On the other hand, an applied field smaller than the anisotropy field results in a magnetization that does not orient in that direction (since that direction is still effectively hard). In this regime, the weaker this static field, the lower the measured MFMA signal.

Figure 4.13 plots the MFMA signal magnitude measured along the hard axis versus

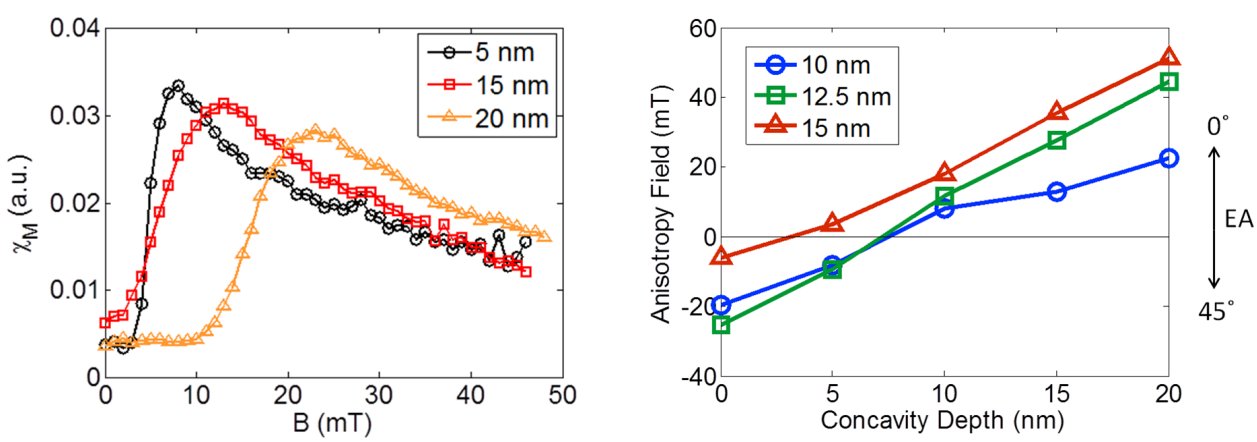

Figure 4. 13: MFMA signal magnitude versus static field for different concavity depths (left) and extracted anisotropy field versus concavity depth for different thicknesses (right).

the applied static field strength (left) for various concavity depths in concave square nanomagnets[18]. The trend of increasing anisotropy field with increasing concavity is consistent with predictions. The figure also plots the measured anisotropy field strength versus concavity depth for various concave square nanomagnet thicknesses. We observe the same trend and in addition note the change in direction (by $\frac{\pi}{4}$) of the hard axis at concavity depths around 5 nm corresponding to the transition from leaf to flower configurations.

Chapter 5. Information Transmission in Nanomagnetic Logic

1. Behavior of Chains in Nanomagnetic Logic

As mentioned previously, chains of nanomagnets for the most part serve the role of interconnects in NML architectures based on coupled magnetic islands. Even the smallest circuits have interconnects, and thus thoroughly studying and developing robust chains are as critical as doing so for gates. Moreover, chains encapsulate many essential engineering questions about the architecture, allowing experimenters to probe the physics of coupling and switching as well as measure key metrics such as speed and reliability. Since chains are such basic elements in the architecture, it is not surprising that they have been the subject of a relatively large number of studies[1,5,7,8,10,15,18,43-49].

The fundamental interaction that chains rely upon to transmit information is stray field coupling (also sometimes called dipolar coupling, though the fields are only dipolar to a rough approximation). The stray field of a typical nanomagnet provides an energetic preference for other magnets placed along an axis orthogonal to its magnetic moment to align antiparallel to that moment. For other magnets placed along the axis parallel to this nanomagnet's magnetic moment, the stray field provides an energetic preference to align parallel to that moment. An ordered series of nanomagnets placed along such an axis forms a chain. Based on the principle of collective energy minimization, the chain favors a particular pair (to account for the magnetization inversion symmetry of the energy) of configurations of magnetic moments. Therefore if the state of any one nanomagnet in the chain is known, then the state of any other nanomagnet is known as long as the chain has minimized its total energy. To transmit a bit of information from one end of a chain to the other, one can thus fix one end, thereby breaking the inversion symmetry, and the result at the other end becomes determined. Figure 5.1 illustrates this concept for two arrangements: a ferromagnetically aligned chain (left) and an antiferromagnetically aligned chain (right). The arrows represent the magnetic moment of each nanomagnet.

If the chain ends up in anything other than this global energy minimum, we consider it to have errors. Many studies[7,43,46,47] suggest that for long enough chains, errors are

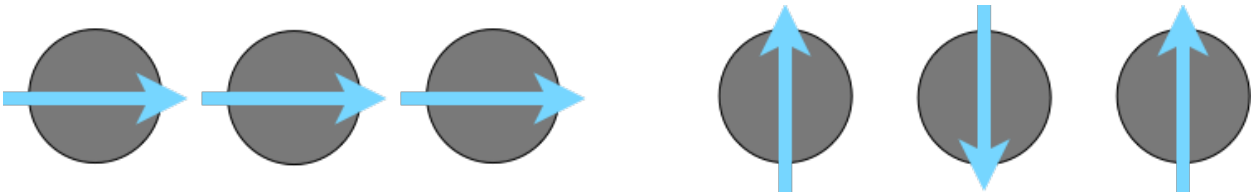

Figure 5. 1: Chain energetic ground states for horizontal (left) easy axes and vertical (right) easy axes.

not only possible, but also probable. A nanomagnet can enter into local energy minimums and become trapped there by its own anisotropy fields. The simplest example of this happens when the fixed end of a typical chain is switched. In typical chains, this event alone would not cause any further switching because the coupling between neighboring magnets is usually too weak compared to the magnetostatic energy of each magnet. Several ways to re-energize chains and seek global energy minimums have been demonstrated. One way, commonly known[45,47] as a 'random walk,' is to allow ambient thermal energy to switch nanomagnets through a random process until all errors are expelled from the chain. As an example, in antiferromagnetically aligned chains a typical error manifests as a ferromagnetically aligned pair of nanomagnets. This frustrated pair of magnets has higher energy compared to non-frustrated pairs, and therefore it is more likely for thermal energy to switch one of the magnets in the frustration. This causes the frustration to effectively spatially translate by one magnet, with direction dependent on which magnet in the pair switches. This movement continues in a random direction at each step until this frustration eventually either leaves through one end of the chain or collides with another frustration, in which case they may annihilate each other. The random movement of the frustration inspired the term 'random walk' for this process. Figure 5.2 illustrates this process in an antiferromagnetically aligned chain for three consecutive steps (from left to right respectively) of movement.

Due to the mirror symmetry of chains, one must employ external forces to limit the directionality of 'random walk' movement. If one wants to transmit one bit from left to right, for example, then one must continue to hold the left end of the chain fixed until all errors are expelled from the chain so that no frustrations can leave the chain through the input end (and thereby switch the input bit). Another serious drawback is the speed at which errors move out of chains, which scales with the square of the chain lengths and is slow for practical chain lengths[45]. Such slow speeds limit the practicality of relying on thermal equilibrium to correct errors in chains.

Another method of pumping energy into chains to induce switching is to apply magnetic fields. Due to similarities with synchronous digital circuits where a clock signal causes latched bits to switch, this process in NML is called 'clocking.' Applying clock fields along both hard axis and easy axis directions have been demonstrated. Hard axis clock

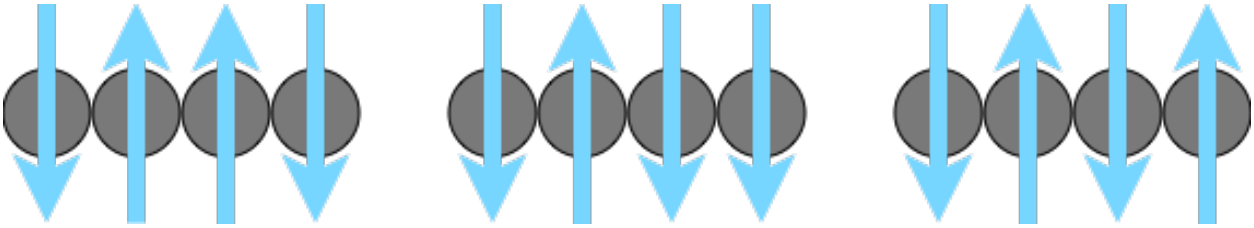

Figure 5. 2: Random walk of an error in the middle of the chain (left) toward the right (center) that eventually leaves the chain (right).

fields act to align all free nanomagnets along a neutral axis from which both information states are equally and easily accessible. If applied very slowly with respect to total switching times, this clocking procedure results in an adiabatic relaxation process analogous to annealing. The input bit, which must be held fixed as the symmetry-breaking element, propagates its bias to all other nanomagnets in the chain while the field is slowly applied. Since switching dynamics are allowed sufficient time to damp out, the chain eventually relaxes into its lowest energy state, with all nanomagnets in mutually reinforcing orientations once the field is finally removed. One of the most common experimental clock schemes, this procedure is easily performed using external magnets. Figure 5.3 illustrates the relaxation process in a chain during and after application of an adiabatic hard axis clock field.

Particularly challenging for this scheme as presented is that perfect reliability cannot be achieved due to thermal fluctuations. Simulations show[7,47] that as chain lengths increase and clock field durations decrease, error probabilities increase to intolerable rates. Chains shorter than five nanomagnets and clock field durations longer than tens of microseconds are required. Both requirements severely limit the practicality of this scheme. A promising solution to these problems is to use both biaxial and uniaxial anisotropies in each nanomagnet to introduce a weaker easy axis along the neutral axis, which would otherwise be the hard axis. Simulations show[5,8,18,44,46] that such a solution helps guard against spontaneous switching from thermal fluctuations. The additional energy well traps the magnetic moment such that it remains stable along the neutral axis, while nearest-neighbor stray field coupling still provides enough bias for each nanomagnet to switch toward the correct orientation. Signal propagation in these types of chains are described[8,44,46] to behave like 'cascades,' though the 'soliton' moniker is also used[50], albeit seldomly. Once all nanomagnets (except the input) are trapped along the minor easy axis, the clock field can be removed without disturbing the orientations of the magnetic moments. The input magnet would then bias its neighboring magnet and cause it to switch, and then that magnet its respective neighbor and so on. This one-by-one sequential switching behavior creates distinct and orderly signal propagation dynamics and gives this scheme its 'cascade' moniker. That the clock field can be removed before signal propagation gains an important advantage for this scheme. Since the clock field only serves the function of aligning nanomagnets toward their neutral axes, greatly reduced

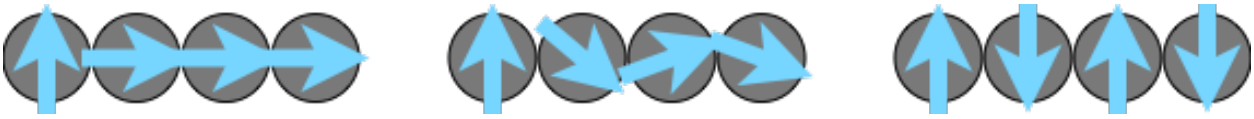

Figure 5. 3: Adiabatic switching during application of a hard axis clock field. Strong field amplitudes align all free magnets toward the neutral axis (left). As the field amplitude decreases, stray field coupling begins to affect the chain (center). After the field is removed, the chain is in its ground state (right).

Figure 5. 4: Non-adiabatic switching after application of a hard axis clock field. Magnets switch one by one (left to right), each exerting its stray field bias on its neighbor to the right.

clock field durations far into the non-adiabatic regimes can be used, resulting in both increased computation performance and increased energy efficiency. Figure 5.4 illustrates the cascade process after application of a non-adiabatic hard axis clock field.

Easy axis clock fields commonly find applications in NML architectures based on larger magnetic shapes with coupling sites. These architectures[10,11,48,51,52] (typically called perpendicular NML) employ magnets with out-of-plane anisotropy, which are irradiated inside some of their coupling sites to create domain nucleation centers. This creates a directionality asymmetry where domain nucleation centers are local coercivity minima and thus switch more easily than neighboring non-irradiated coupling sites, with which they are mutually coupled. Signals typically propagate by domain wall motion and thus chains are not needed, though arrangements of logical inverters that are equivalent to chains have been demonstrated. If one applies an easy axis (out-of-plane) clock field such that the coercivity of domain nucleation centers is exceeded while the coercivity of non-irradiated coupling sites is not reached, then the domain nucleation centers switch due to stray field coupling from neighboring coupling sites and domain wall motion eventually causes the entire magnet to switch. Clock fields in both directions along the easy axis are needed (usually applied in an alternating pattern) so that only the sum of the clock field and stray fields when they are parallel is allowed to exceed the domain nucleation center coercivity. Therefore, the challenge facing this scheme is in controlling the clock field amplitude, stray field coupling strength, and domain nucleation center coercivities to within small enough margins for reliable operation.

2. Analytical Study of Chains of Nanomagnets with Biaxial Anisotropy

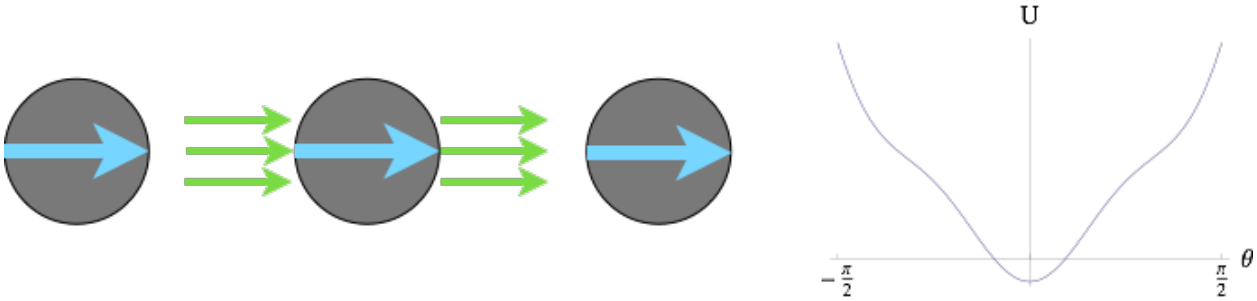

Figure 5. 5: Fields exerted on center magnet by its neighbors, which are aligned with a horizontal neutral axis (left). Sample energy density (right).

Pertaining to the fairly promising scheme of using both uniaxial and biaxial anisotropies in the nanomagnets of chains subject to clock fields in the non-adiabatic regime, a simple physical model that can be easily analyzed yet still provide reasonable approximations to the most important mechanisms is useful for exploring the vast design space that we confront. To this end, we approximate each nanomagnet as a magnetic point dipole of constant magnitude with total anisotropy equal to a combination of uniaxial and biaxial anisotropy. The expression for the energy density of the magnet is:

$$U(\theta) = -K_u sin^2(\theta) - \frac{K_b}{4} cos^2(2\theta) \tag{5.1}$$

θ is the angle of the magnetic moment with respect to the neutral axis, K_u is the uniaxial anisotropy constant, and K_b is the biaxial anisotropy constant. The magnetic field produced by the magnet is the well-known magnetic dipole field:

$$\vec{B}(\vec{r}) = \frac{\mu_0}{4\pi}\left(\frac{3\vec{r}(\vec{m}\cdot\vec{r})}{r^5} - \frac{\vec{m}}{r^3}\right) \tag{5.2}$$

μ_0 is the permeability of free space, m is the magnetic moment, and r is the position vector with respect to the magnet. We assume adiabatic relaxation of magnets in the absence of thermal energy, and therefore no dynamics are captured. We assume that the non-adiabatic clock pulse has the effect of aligning all magnets along the neutral axis, and is instantaneously removed before calculations are made. Though seemingly quite rudimentary, this model can still predict the regions of the parameter space that accommodate properly functioning chains.

We consider an antiferromagnetically aligned chain. After clocking, all magnets are aligned with the neutral axis (horizontal in figure 5.5) resulting in a ferromagnetically aligned configuration. If only nearest-neighbor contributions to dipole field coupling are included, then figure 5.5 represents the state of any one magnet in the chain (excluding the ends) and its neighbors. The center magnet is the magnet of interest and the green arrows represent the magnetic field exerted on it by its neighbors. In this geometry, the magnetic

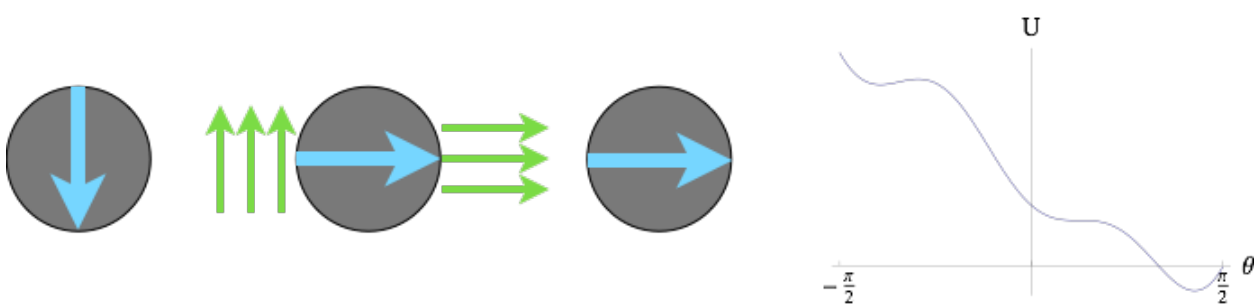

Figure 5. 6: Fields exerted on center magnet by its neighbors, one of which is aligned with a vertical easy axis (left). Sample energy density (right).

field exerted onto the center magnet by each neighbor is along the neutral axis and has magnitude:

$$B = \frac{\mu_0 M_S V}{2\pi r^3} \tag{5.3}$$

M_S and V are the magnetization and volume of each magnet, respectively, and r is the distance between the positions of any two neighbors. As a result of these fields, the expression for the energy density of the center magnet becomes:

$$U(\theta) = -K_u sin^2(\theta) - \frac{K_b}{4} cos^2(2\theta) - 2M_S B cos(\theta) \tag{5.4}$$

In order for this chain to function properly, the center magnet must remain aligned along the neutral axis as long as both neighbors are as well. To achieve this, an energy well corresponding to the minor easy axis must exist along this axis, at θ = 0 due to even symmetry. As we smoothly vary the K_u and K_b parameters, we find a smooth transition

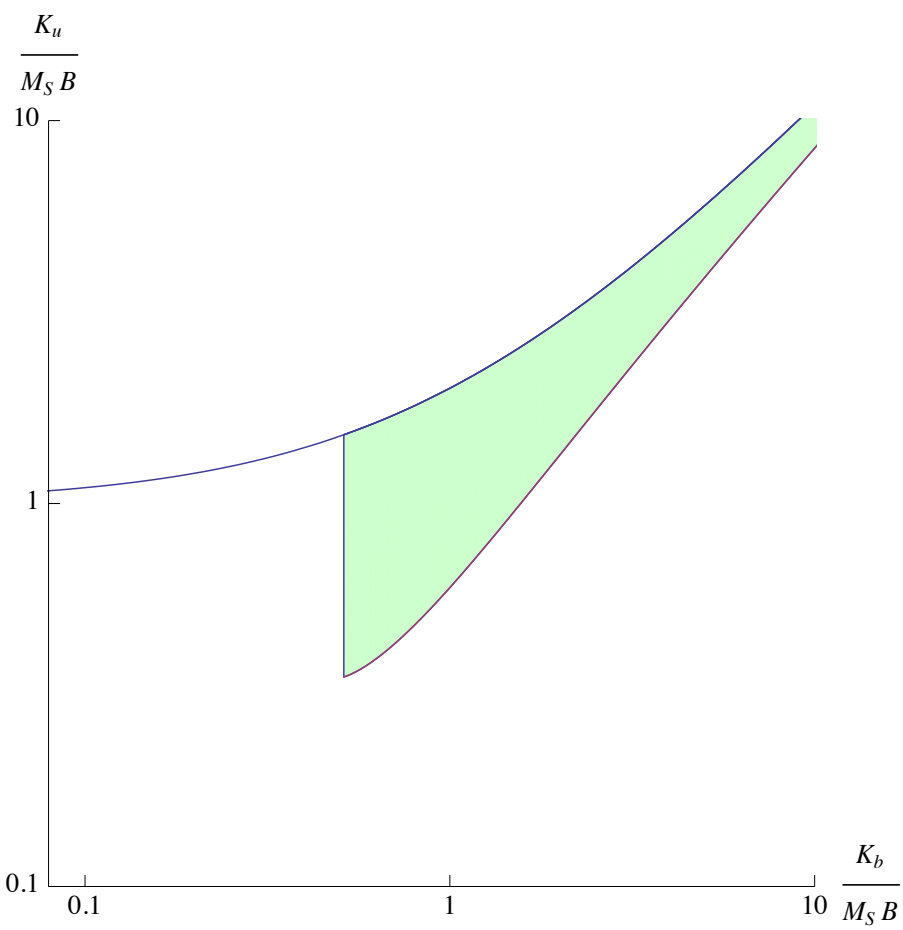

Figure 5. 7: Parameter space producing functioning antiferromagnetically aligned chains (green) according to our analytical model.

between an energy well and an energy hill, which have curvatures of opposite sign from each other. The combination of parameters that correspond to the boundary of transition where the energy well vanishes produces a saddle point at θ = 0, implying that U(θ) satisfies the conditions:

$$\frac{\partial U(\theta)}{\partial \theta} = 0 \tag{5.5}$$

$$\frac{\partial^2 U(\theta)}{\partial \theta^2} = 0 \tag{5.6}$$

The solution corresponding to the existence of the energy well is:

$$M_S B > K_u - K_b \tag{5.7}$$

This inequality agrees with intuition: increasing K_b and decreasing K_u leads to a deeper energy well.

Once a neighboring magnet switches, the state of the center magnet and its neighbors changes to resemble figure 5.6. In this geometry, the magnetic field exerted onto the center magnet by its left neighbor is B/2 along the easy axis. As a result of the sum of the fields from each neighbor, the expression for the energy density of the center magnet becomes:

$$U(\theta) = -K_u sin^2(\theta) - \frac{K_b}{4} cos^2(2\theta) - M_S B \left(cos(\theta) + \frac{sin(\theta)}{2} \right) \tag{5.8}$$

Proper chain functionality demands that the center magnet switch to align antiparallel to its left neighbor. To achieve this, the energy density must be monotonically decreasing as θ increases toward the easy axis energy well. Otherwise, an energy barrier forms that blocks the magnet from rotating toward its easy axis. Assuming the neighboring magnets are fixed (so that the stray fields from the center magnet have no effect), as we smoothly vary the K_u and K_b parameters, we find a smooth transition between an energy barrier and an energy slope. The combination of parameters that correspond to the boundary of

Figure 5. 8: Fields exerted on center magnet by its neighbors, which are aligned with a vertical neutral axis (left). Sample energy density (right).

transition where the energy barrier vanishes produces a saddle point at some θ > 0 in the first quadrant, implying the conditions from equations 5.5 and 5.6 on U(θ). Unlike equation 5.7, where we are able to reduce two equations to one equation and eliminate one variable, the equations in this case cannot be solved to eliminate θ and thus the solution corresponding to an energy slope is a pair of inequalities parameterized by θ:

$$\frac{8K_b}{M_S B} < \frac{1}{2sin^3(\theta)} + \frac{1}{cos^3(\theta)} \tag{5.9}$$

$$\frac{8K_u}{M_S B} > \frac{1}{2sin^3(\theta)} - \frac{1}{cos^3(\theta)} - \frac{3}{sin(\theta)} + \frac{6}{cos(\theta)} \tag{5.10}$$

$0 < \theta \leq \theta_0$ where $\theta_0 \approx 0.228007\pi$ and equation 5.9 reaches its minimum value in the first quadrant at θ_0.

Figure 5.7 plots and shades the region satisfying equations 5.7, 5.9, and 5.10 on a log-log scale as a function of the dimensionless parameter $\frac{K}{M_S B}$ for the biaxial and uniaxial anisotropy constants, respectively on the x and y axes. We observe several interesting results from this plot. First, if we hold the anisotropy constants fixed and increase the coupling strength $M_S B$, the shaded region is wider. This means that stronger coupling allows a greater proportional range of anisotropy constants to operate. If the anisotropy constants practically vary due to fabrication variances, then a wider distribution can be tolerated if coupling is strong. Second, the lower bound terminates at θ_0 but we can of course choose even smaller values of K_b and still find values of K_u that produce functioning chains. However, the coupling is so strong that no energy barrier forms (instead an energy slope always forms) and thus no saddle points are detected by the calculation. We call this region the coupling-dominated region, where the coupling strength $M_S B$ is very strong compared to the anisotropy constant. However, if we hold the coupling strength fixed and decrease the anisotropy constants, we must make an important distinction. The converse, where the anisotropy constant is very weak compared to the coupling strength, is not necessarily desirable. Following the theory of superparamagnetism, we can easily see by

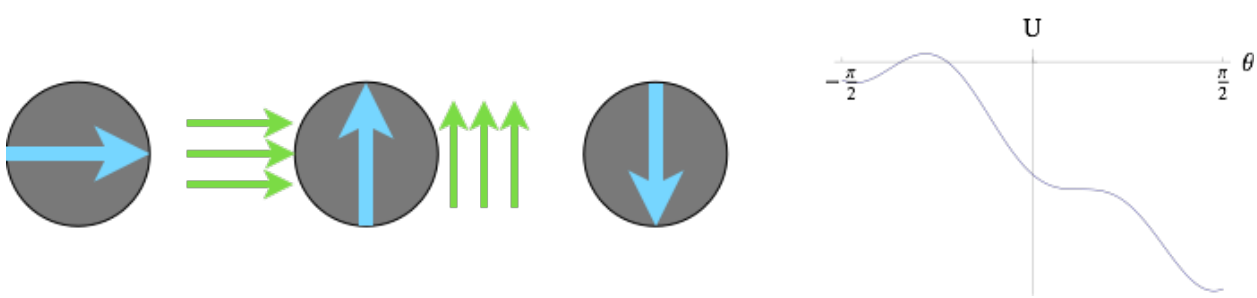

Figure 5. 9: Fields exerted on center magnet by its neighbors, one of which is aligned with a horizontal easy axis (left). Sample energy density (right).

inspecting equation 3.22 that magnets with smaller anisotropy constants are more susceptible to thermal fluctuations, which our model does not incorporate. Third, in the non-coupling-dominated region, the ideal operating region with the greatest proportional parameter tolerance is where K_u is approximately equal to the coupling strength and K_b is approximately the coupling strength divided by $\sqrt{2}$.

We consider a ferromagnetically aligned chain. If clock fields can only be applied globally, then the clock field acts to align the magnets in such a way that their stray fields demagnetize each other, and thus raise each magnet to a higher energetic state. Instead, if local clock fields can be applied, then after clocking all magnets are aligned with the neutral axis (vertical in figure 5.8) resulting in an antiferromagnetically aligned configuration. For the latter case, figure 5.8 represents the state of any one magnet in the chain (excluding the ends) and its neighbors. In this case, the magnetic field exerted onto the center magnet by each neighbor is B/2. Therefore, we can simply replace B by B/2 in equation 5.7 to arrive at the condition for existence of an energy well at θ = 0:

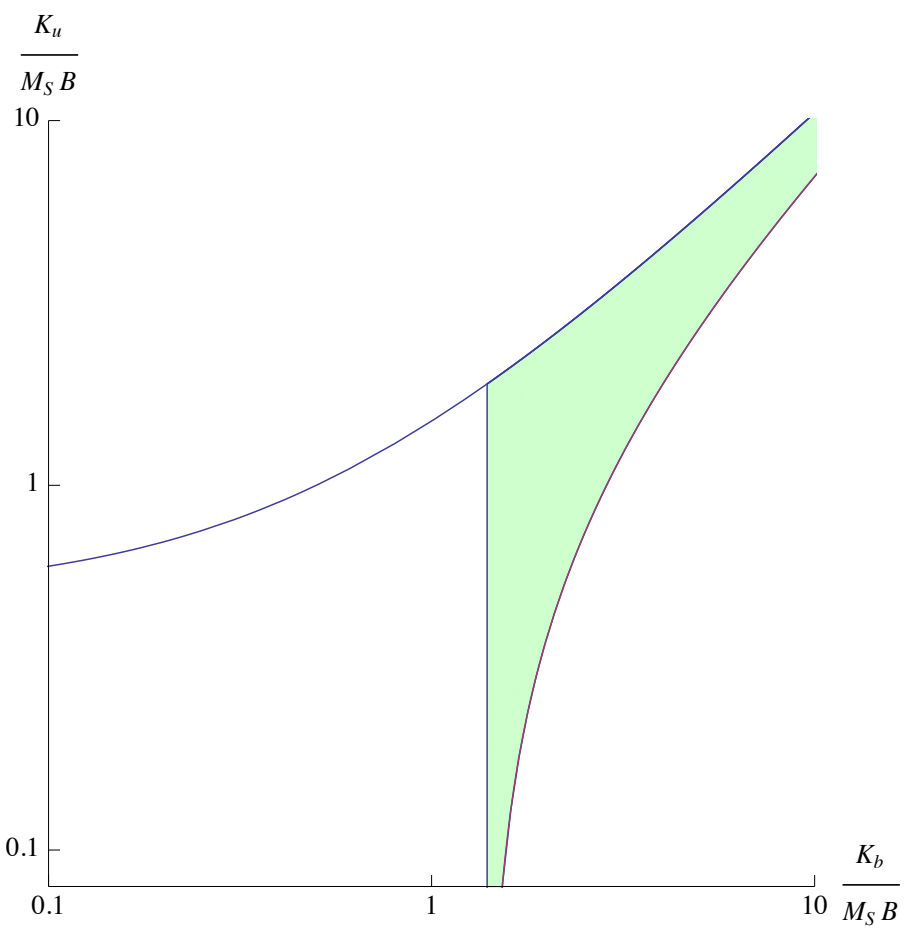

Figure 5. 10: Parameter space producing functioning ferromagnetically aligned chains (green) according to our analytical model.

$$\frac{M_S B}{2} > K_u - K_b \tag{5.11}$$

Once a neighboring magnet switches, the state of the center magnet and its neighbors changes to resemble figure 5.9. In this geometry, the magnetic field exerted onto the center magnet by its left neighbor is B/2 along the easy axis. As a result of the sum of the fields from each neighbor, the expression for the energy density of the center magnet becomes:

$$U(\theta) = -K_u sin^2(\theta) - \frac{K_b}{4} cos^2(2\theta) - M_S B \left(\frac{cos(\theta)}{2} + sin(\theta) \right) \tag{5.12}$$

Proper chain functionality demands a vanishing energy barrier and thus a saddle point at some θ > 0 in the first quadrant, implying the conditions from equations 5.5 and 5.6 on U(θ). The solution corresponding to an energy slope is a pair of inequalities parameterized by θ:

$$\frac{8K_b}{M_S B} < \frac{1}{sin^3(\theta)} + \frac{1}{2cos^3(\theta)} \tag{5.13}$$

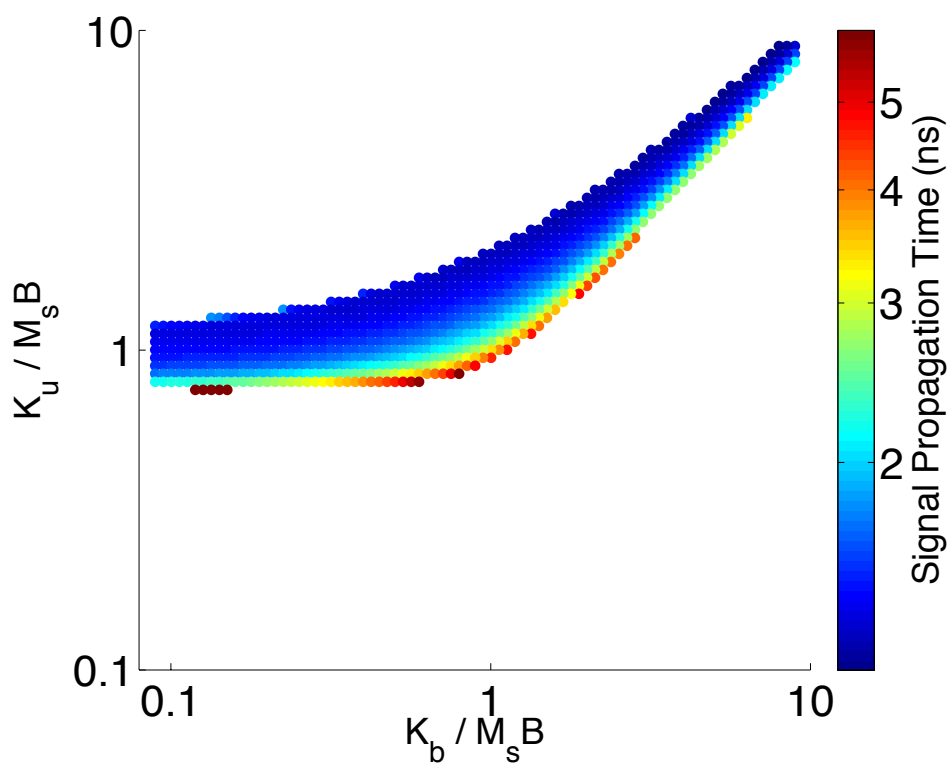

Figure 5. 11: 0 K macro-spin parameter sweep for 50 nm x 50 nm x 12 nm magnets with 20 nm gaps between them identifying working antiferromagnetically aligned chains.

$$\frac{8K_u}{M_S B} > \frac{1}{sin^3(\theta)} - \frac{1}{2cos^3(\theta)} - \frac{6}{sin(\theta)} + \frac{3}{cos(\theta)} \tag{5.14}$$

$0 < \theta \leq \theta_0$ where $\theta_0 \approx 0.151172\pi$ and equation 5.14 reaches 0 in the first quadrant at θ_0 (that is, this restriction is equivalent to requiring that K_u be non-negative).

Figure 5.10 plots and shades the region satisfying equations 5.11, 5.13, and 5.14 on a log-log scale as a function of the dimensionless parameter $\frac{K}{M_S B}$ for the biaxial and uniaxial anisotropy constants, respectively on the x and y axes. Similar arguments about θ_0 and wider anisotropy constant distribution tolerance for stronger coupling apply as before. In this case, in the non-coupling-dominated regime the ideal operating region with the greatest proportional parameter tolerance is where K_u is approximately equal to the coupling strength and K_b is approximately $\sqrt{2}$ times the coupling strength.

3. Simulation Study of Chains of Nanomagnets with Biaxial Anisotropy

We can improve on our crude model of chains by using numerical macro-spin simulations based on a discretized stochastic Landau-Lifshitz-Gilbert equation. Compared to our analytical model, additional physics such as three spatial dimensions, time dynamics, thermal fluctuations, and non-nearest-neighbor coupling are all captured in these

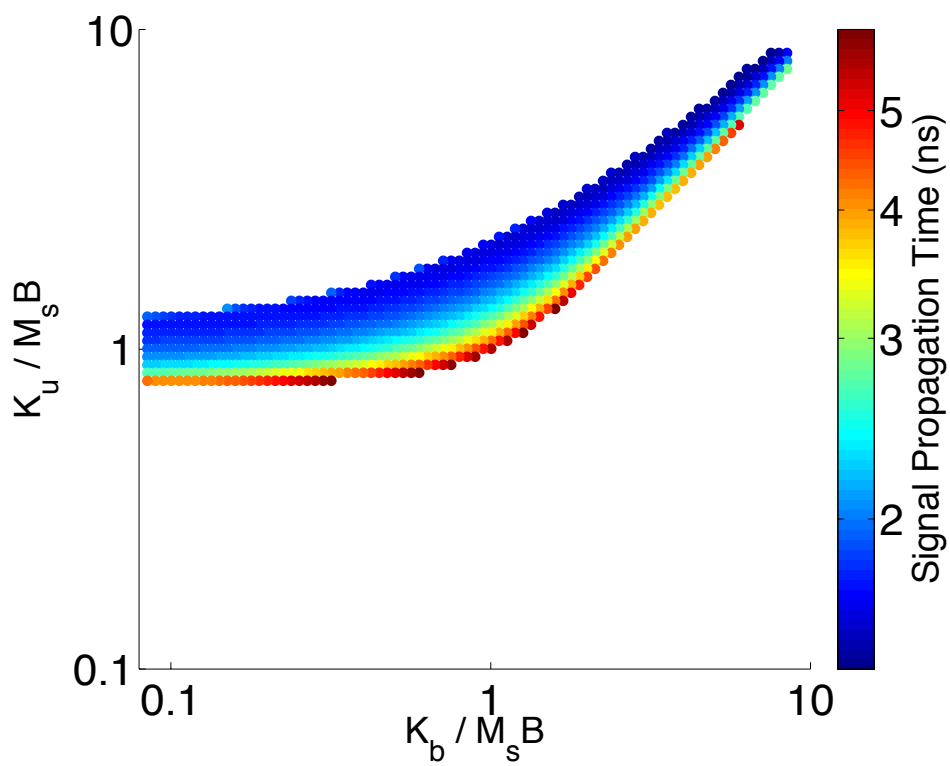

Figure 5. 12: As figure 5.11 but for 150 nm x 150 nm x 12 nm magnets with 30 nm gaps.

simulations. Employing the program from appendix B.1, we simulated both antiferromagnetically and ferromagnetically aligned chains at various sizes, spacings, and temperatures for a logarithmically spaced parameter space of the anisotropy constants. We chose standard permalloy material parameters and an apparent damping constant of 0.1. The volume of each magnet was calculated as a rectangular prism, though the demagnetizing field was calculated for a general ellipsoid. Unlike our analytical model, effects of the thickness of each magnet were accounted for here. In order to specify our own anisotropy constants, we created all magnets as circular disks to remove in-plane shape anisotropy, and then added the corresponding anisotropy fields onto the demagnetizing fields. We treated the effect of the clock field as effectively starting each simulation with all magnets (except the input) ideally aligned as intended by the clock field and applying no further magnetic fields. All simulations included a chain of 12 nanomagnets as well as a fixed input[18] (due to magnetization inversion symmetry, the results should not depend on which bit is chosen as input) and a fixed block[49] (to assist the final magnet in the chain such that figure 5.5 is representative of its surroundings). We allowed each simulation to run for a maximum of 6 ns of simulation time. If a pair (K_b, K_u) of anisotropy constant values produced no errors, then it was considered to produce properly functioning chains.

Figure 5.11 plots the properly functioning anisotropy constant pairs in an

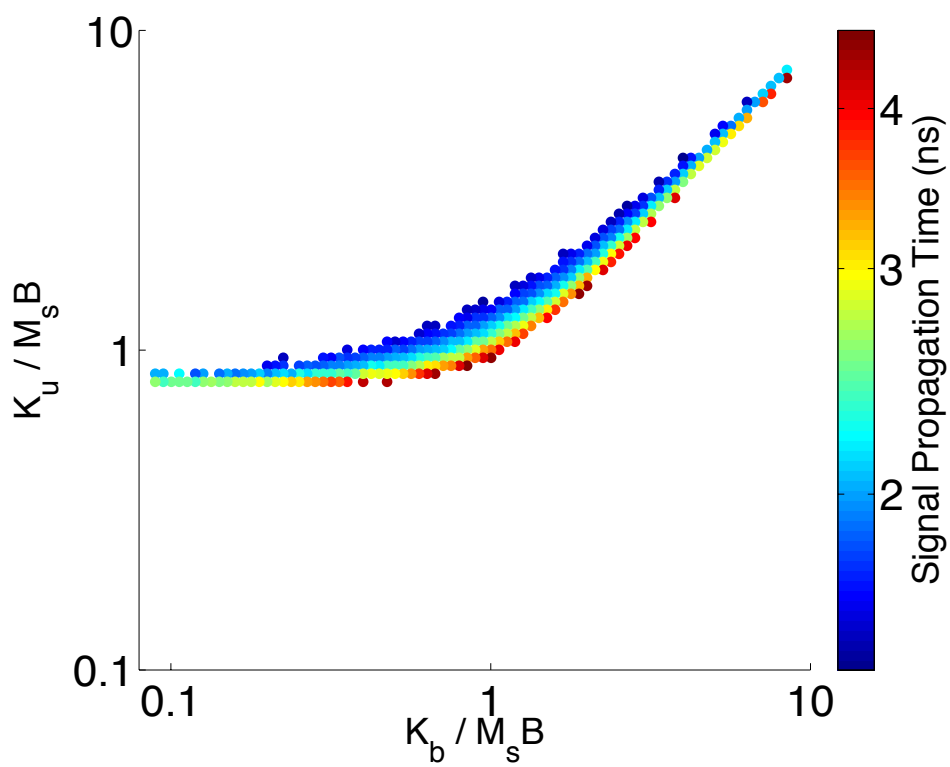

Figure 5. 13: 300 K macro-spin parameter sweep for 50 nm x 50 nm x 12 nm magnets with 20 nm gaps between them identifying working antiferromagnetically aligned chains.

antiferromagnetically aligned chain for 50 nm x 50 nm x 12 nm magnets with 20 nm gaps between them and at 0 K. The total signal propagation time through the chain is logarithmically indicated on the color scale. The shape and scale of the colored region is comparable to that of figure 5.7, except the coupling-dominated region appears as well.

A few interesting features resulting from our macro-spin model are worth mentioning for the sake of comparison with our analytical model. First, at 0 K one would expect that an energy well along the neutral axis is not necessary. However, the region has a similarly shaped upper bound on K_u suggesting the contrary. In our macro-spin model, this bound is due to non-nearest-neighbor coupling (specifically, next-nearest-neighbor coupling, since the stray fields of next-nearest-neighbors act against those of nearest-neighbors). Though the strength of next-nearest-neighbor coupling is far weaker than that of nearest-neighbor coupling, during the process of signal propagation a given magnet interacts with its next-nearest-neighbor before its nearest-neighbor, and hence an energy well is needed. Second, the lower bound of the region occurs at somewhat higher K_u resulting in an overall narrower region. Our explanation for this is twofold. Since we terminated all simulations at no more than 6 ns of simulation time, chains that may eventually switch correctly are discarded as being too slow. For a fixed K_b, decreasing K_u should result in a slower switching process since the effective field H_{eff} on which $\frac{dM}{dt}$ depends would also decrease. The color scale indicating signal propagation time shows

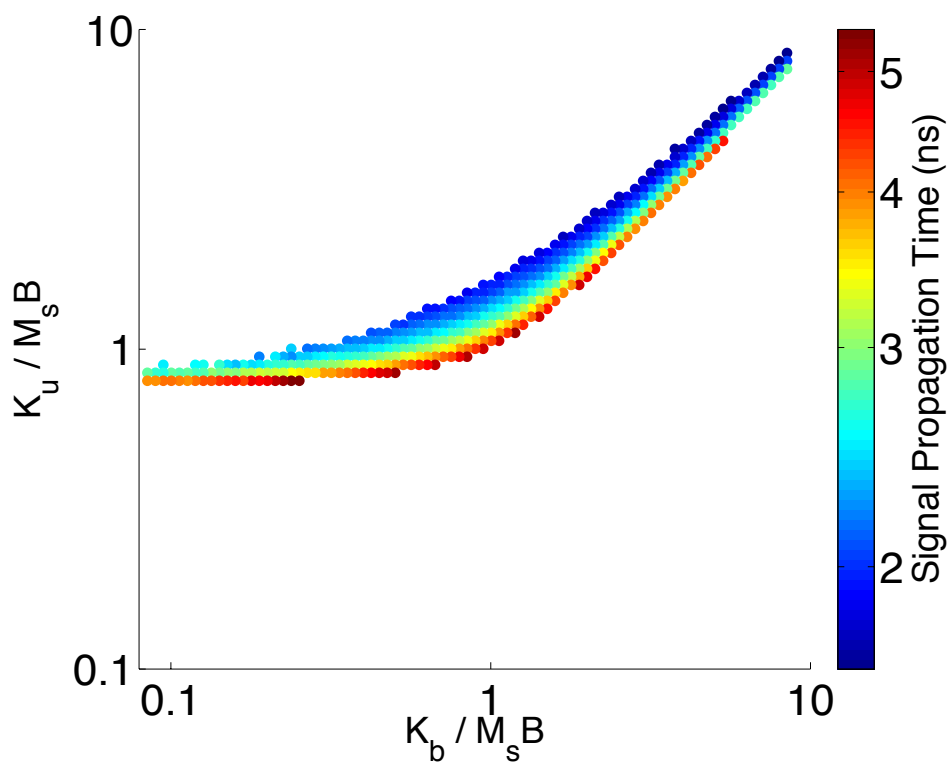

Figure 5. 14: As figure 5.13 but for 150 nm x 150 nm x 12 nm magnets with 30 nm gaps.

that this is a continuous and monotonic dependence. In addition, since next-nearest-neighbor coupling acts against nearest-neighbor coupling as mentioned above, the effective coupling strength between neighbors is lower (though only by a small portion) than assumed in our analytical model.

Figure 5.12 is a similar plot to figure 5.11 where the only parameters changed are the size of the magnets (to 150 nm x 150 nm x 12 nm) and the spacing between them (to 30 nm). Our analytical model did not depend on these parameters in any way except for the coupling field B, which we used as a scaling factor for the anisotropy constants. The high degree of similarities between these two figures shows that scaling the anisotropy constants by the coupling strength mostly accounts for the differences in dimensions. Other effective differences resulting from the different dimensions are the demagnetizing factors (the larger lateral dimensions appear as flatter disks) and the effects of thermal fluctuations (thermally assisted switching depends on total anisotropy energy KV rather than energy density). At 0 K, these differences appear to be negligible.

Figures 5.13 and 5.14 are plots using the same dimensions as figures 5.11 and 5.12, respectively, but simulated at 300 K. If a pair (K_b, K_u) of anisotropy constant values produced no errors for 20 simulations (each with randomized thermal fluctuations), then it was considered to produce properly functioning chains. A few interesting features are worth mentioning for comparison with the simulations at 0 K. First, due to the stochastic

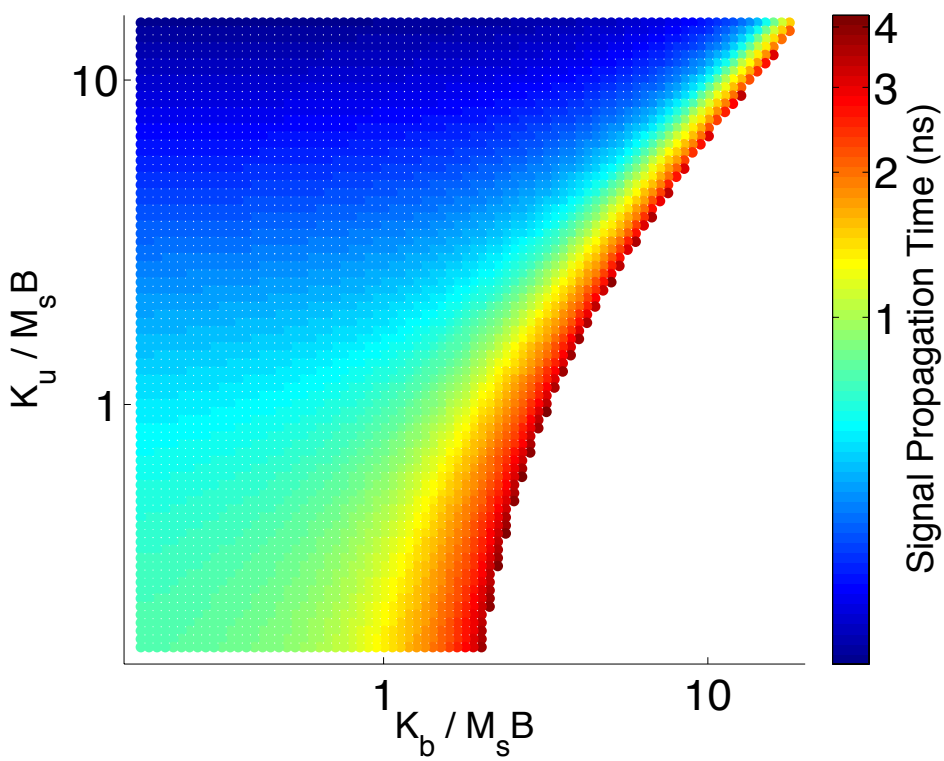

Figure 5. 15: 0 K macro-spin parameter sweep for 50 nm x 50 nm x 12 nm magnets with 38.2 nm gaps between them identifying working ferromagnetically aligned chains.

nature of thermal fluctuations, which contribute to error formation, the boundaries of the colored region are rough. We expect that increasing the number of simulations required for each pair of anisotropy constant values would diminish this effect. Second, the upper bound of the region occurs at much lower K_u values suggesting that the additional neutral axis energy well depth gained as a result is needed to tolerate thermal fluctuations. This agrees with intuition, since we found the upper bound of the analytical result by setting the energy well depth to 0. Third, the width of the coupling-dominated region is significantly narrower. This follows our prediction made using the analytical model regarding superparamagnetic effects. As the anisotropy constants decrease, the anisotropy energy KV decreases leading to an increased capacity for thermal fluctuations to spontaneously switch magnets. This same argument also explains the increased edge roughness of the region in figure 5.13 as compared to that in figure 5.14. Since each magnet's volume is smaller by a factor of 9, the lower anisotropy energy leads to higher susceptibility to thermal fluctuations, which we attributed the edge roughness to above.

Figures 5.15 and 5.16 plot the properly functioning anisotropy constant pairs in a ferromagnetically aligned chain at 0 K for 50 nm x 50 nm x 12 nm magnets with 38.2 nm gaps between them and 150 nm x 150 nm x 12 nm magnets with 76.8 nm gaps between them, respectively. The discrepancy in gap size is to normalize the switching field magnitude with the plots above, leading to an effective $\sqrt[3]{2}$ increase in the distance r between the centers of adjacent magnets. This also helps account in part for common

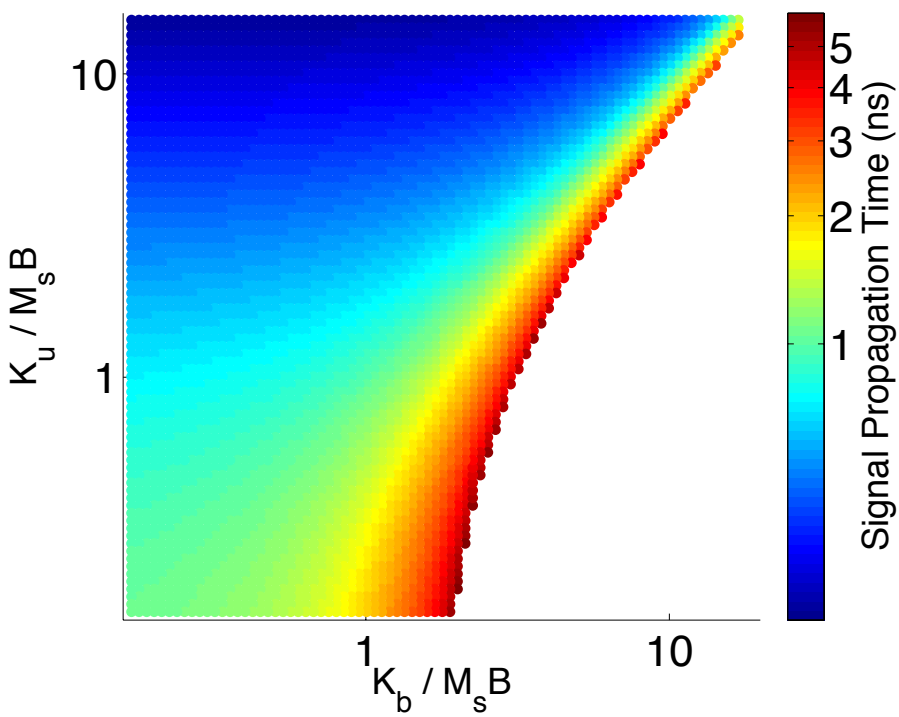

Figure 5. 16: As figure 5.15 but for 150 nm x 150 nm x 12 nm magnets with 76.8 nm gaps.

experimental designs that demand larger r for ferromagnetically aligned chains due to the use of elongated shapes for shape anisotropy. The shape and scale of the lower bound of the colored region is comparable to that of figure 5.10, except the coupling-dominated region appears as well. The interesting feature to note in these plots as compared to the simulation plots above is that there is no upper bound to the region. Since non-nearest-neighbor coupling reinforces nearest-neighbor coupling in ferromagnetically aligned chains, no neutral axis energy well is necessary at 0 K.

Figures 5.17 and 5.18 are plots using the same dimensions as figures 5.15 and 5.16, respectively, but simulated at 300 K. Most notably, the upper bound of the colored region is reintroduced since a neutral axis energy well is needed to tolerate thermal fluctuations. The shape of this region closely resembles a combination of figure 5.10 and a portion of the coupling-dominated region. The upper bound of the region occurs at lower K_u values and the boundaries are rough due to the same arguments as presented for figures 5.13 and 5.14. We also note from comparing the color scales that signal propagation times are exceptionally fast at 0 K as a result of next-nearest-neighbor coupling contributing to switching. At 300 K, signal propagation times are again commensurate with those of the antiferromagnetically aligned case, since next-nearest-neighbor coupling is no longer strong enough to cause switching. The greater edge roughness of the region in figure 5.17 as compared to that of figure 5.18 is explained by the same superparamagnetism argument

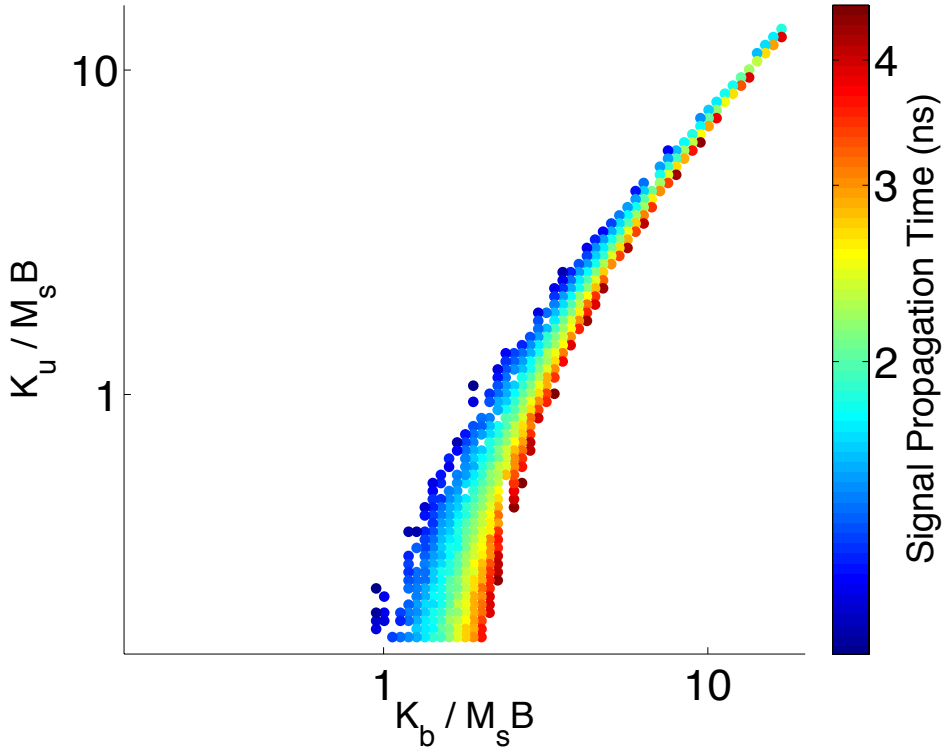

Figure 5. 17: 300 K macro-spin parameter sweep for 50 nm x 50 nm x 12 nm magnets with 38.2 nm gaps between them identifying working ferromagnetically aligned chains.

as above.

Our analytical model generally predicts our simulation results with only minor differences. The macro-spin simulations add value by examining additional trends created by the introduction of time dynamics and thermal fluctuations. Given the results shown here, we chose to restrict more detailed (and computationally expensive) studies of chains to nanomagnets with anisotropy energy densities that are on the order of the stray field coupling strengths.

4. Simulation Study of Chains of Nanomagnets with Configurational Anisotropy

We can improve on our macro-spin simulation model by using a full micromagnetic approach based on a discretized stochastic Landau-Lifshitz-Gilbert equation. Compared to our macro-spin model, additional physics such as the exchange interaction, non-uniform magnetization (leading to configurational anisotropy), and non-uniform stray field coupling are all captured in these simulations. As a result, we no longer need to add material anisotropy and instead use standard permalloy material parameters, allowing the shape of each magnet to determine its overall anisotropy. We chose an apparent damping constant of 0.02 following the intuition that as mesh sizes become finer, the apparent damping constant should decrease toward the microscopic damping constant. We performed this section's simulations using OOMMF with atlases similar to figure 5.19. Each

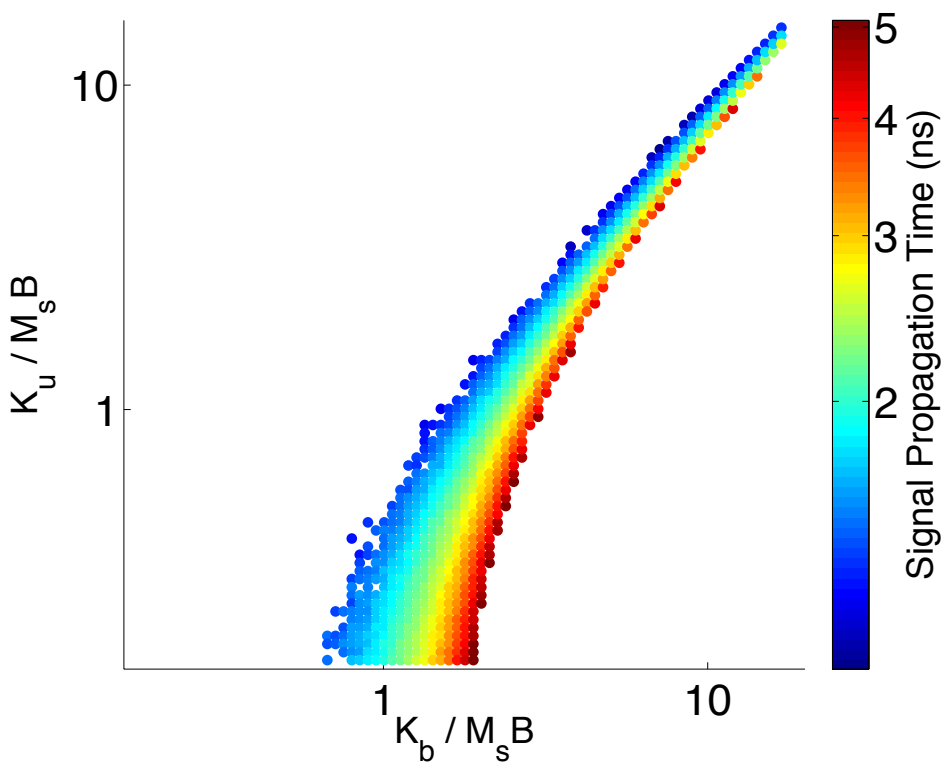

Figure 5. 18: As figure 5.17 but for 150 nm x 150 nm x 12 nm magnets with 76.8 nm gaps.

pixel of the atlas corresponds to a mesh cell of size 10 nm x 10 nm x 12 nm. Each of the 12 magnets in the chain is 150 nm wide and 290 nm long with 30 nm deep indentations along the short edges. We then increased the length of all magnets in increments of 10 nm per set of simulations to sweep through a parameter space of anisotropy strengths. Each atlas also contains an input and a block, both of which are ellipse-shaped.

We performed 3 sets of micromagnetic simulations using the atlas design in figure 5.19. The first set initializes all red, blue, and black pixels with magnetization directed toward the right (an idealized clock as in our macro-spin simulations), and all green pixels directed upward. The chain then relaxes at 0 K for 27 ns of simulation time. The second set is identical to the first set except for a temperature of 300 K. The third set, also performed at 300 K, initializes all red pixels up, all blue pixels down, and all green and black pixels toward the right. Each simulation in this set begins with a piecewise linear clock field oriented toward the right of width 3 ns, rise time 200 ps, fall time 300 ps, and amplitude 84 mT, following the program in appendix A.3. The simulation then runs until a simulation time of 30 ns. We repeated each simulation performed at 300 K 10 times to account for variations from thermal effects. We then recorded the final state of the chain from each simulation and then counted the number of magnets in a row that resulted in the logically correct state (called the propagation distance here), starting from the input (left). Figure 5.20 plots the mean and standard error (standard deviation divided by the square root of the number of samples) of the propagation distance for all 3 sets of simulations.

This plot shows a couple of noteworthy features. Each set of simulation conditions produces an optimal region of dimensions with fairly high propagation distance. This region starts near 340 nm and then tapers off more quickly as conditions more closely mimic reality. According to section 4.4 longer nanomagnets effectively have higher K_u values, thus introducing thermal fluctuations (magneta curve) reduces the upper bound of the optimal region by the same argument as presented in section 5.3. Additionally simulating the pulsed clock field (green curve) consequently introduces thermal fluctuations to the clocking process. We believe that these results are limited in accuracy by the choice of fairly large mesh sizes and time steps. However, we chose a balance between physically meaningful results and reasonable computation times. We also recognize that the design of the blocks cause artifacts. For example, the 0 K (black curve) simulation should attain perfect propagation inside the optimal region, but does not due to too high of a coupling strength between the last magnet and the block. An interesting measurement artifact related to this is the increased noise of the curve at the upper bound, most noticeable in the black curve. Since we observed only the final state of each simulation, any errors involving switching order (in some sense, a causality violation) that

Figure 5. 19: OOMMF atlas design used for micromagnetic simulations.

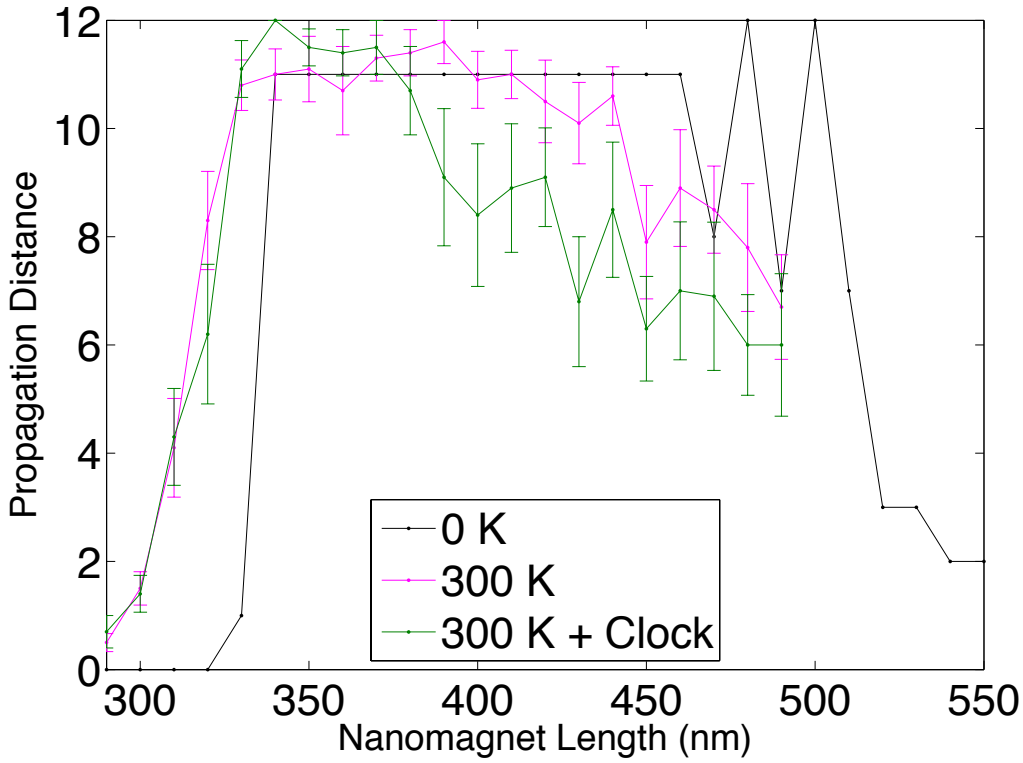

Figure 5. 20: Mean propagation distance of all 3 sets of micromagnetic chain simulations for nanomagnets of width 150 nm and thickness 12 nm.

happen to result in a correct final state become effectively hidden from us. By observing the dynamics, we found that errors nucleating at the output as a result of mutual coupling with the block (which forms a mirror-asymmetric configuration instead of a single domain) primarily account for these false positives. A more sophisticated block design as in section 5.5 corrects this flaw. However, the design used in figure 5.19 is more representative of our experimental designs.

Figure 5.21 overlays the calculated (in section 4.4) parameters of nanomagnets used in the micromagnetic simulations represented by the magenta curve in figure 5.20 on top of figure 5.14 using magenta and black points. The conditions from this set of simulations most closely match those of those from figure 5.14, namely 300 K and an idealized clock. Points achieving a mean propagation distance over 10 are colored magenta, while those otherwise are colored black. Ideally, the magenta segment would overlap the region behind it. The discrepancy in position is a result of differences in behavior caused by both the additional physics captured by micromagnetic simulation as well as the additional simulation artifacts introduced. The discrepancy however is not too large, and gives us confidence that our analytical, macro-spin, and micromagnetic models are all fairly consistent.

5. Signal Propagation Speed in Nanomagnetic Logic

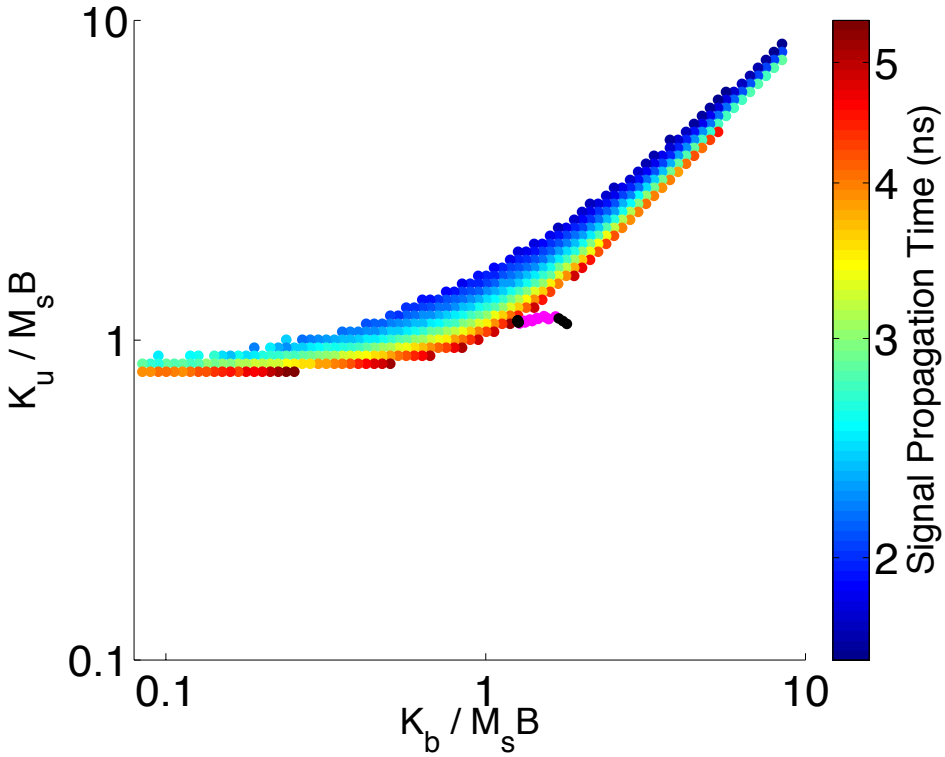

Figure 5. 21: As figure 5.14 but with most similar micromagnetic simulation superimposed (magenta and black). Smaller nanomagnet lengths are toward the right of the segment.

By inspecting the Landau-Lifshitz-Gilbert equation we see that both the effective field H_{eff} and damping constant α influence the switching time of a magnet. Intuitively, since both terms of the equation depend on H_{eff}, increasing H_{eff} would lead to faster dynamics. The most direct way to achieve this is to increase the coupling strength between neighboring magnets, which also has the benefit of increase tolerance against errors. Laterally downscaling is a feasible path for this, as the dipole field strength depends scales as the magnet volume divided by the distance between magnets, which as an overall quantity scales as $\frac{1}{r}$. On the other hand, α affects the relative contributions of precession and damping. Figure 5.22 plots the easy axis component of magnetization for a macro-spin initialized along the hard axis, subject to an easy axis magnetic field, for 3 different values of α. The 3 curves roughly represent underdamped, critically damped, and overdamped regimes, respectively for increasing α. Critical damping "fully" switches the fastest, though the α value depends on geometry and has been calculated for other shapes[26,31]. If full switching is not required, then for in-plane magnets smaller α values were found to switch faster, while for out-of-plane magnets larger α values were faster[31].

Several simulation-based estimates[5,8,15] of the switching time of a single nanomagnet put it in the range of 100 – 150 ps. In the case of the macro-spin in figure 5.22,

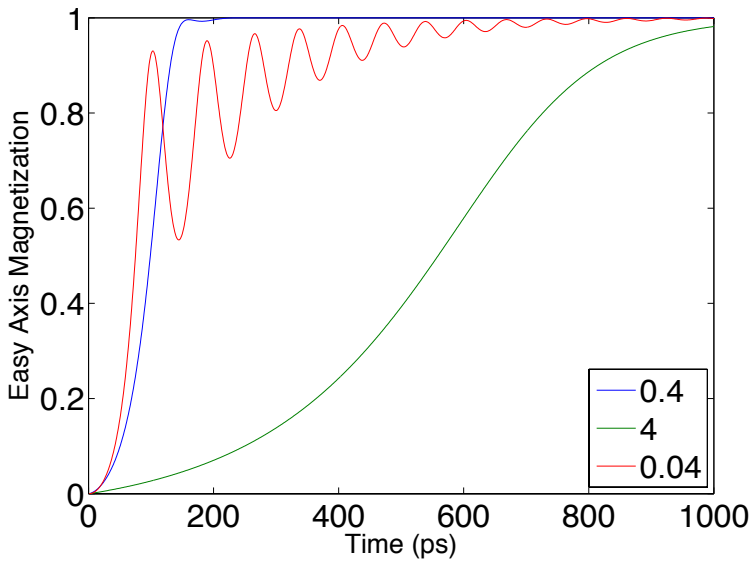

Figure 5. 22: Normalized easy axis magnetization versus time for a 50 nm x 100 nm x 12 nm macro-spin subject to an easy axis field of 5 mT for 3 different α values.

apparent damping constants on the order of 0.1 (as used in section 5.3) produce minimum switching times that also fall into this range. However, switching times slower than 400 ps are also possible and are not necessarily thermally assisted, as evidenced by the 0 K simulations. Figure 5.23 shows a time-series of frames from an OOMMF simulation of a chain of similar design to figure 5.19, but with an improved block design. The size of each nanomagnet is 400 nm x 150 nm x 12 nm fitted to a mesh size of 5 nm x 5 nm x 4 nm. Due to the finer mesh cell size, we chose a smaller time step of 10^{-14} s to prevent exchange interaction related artifacts. The simulation again begins with a piecewise linear clock field as in the green curve of figure 5.20, but with width of 2 ns and amplitude 100 mT. We chose a damping constant of 0.02 and a temperature of 300 K. The frames show the vertical projection of magnetization as blue for up, red for down, and black for none. An average switching time of 390 ps per nanomagnet can be extracted from these frames.

Figure 5.24 demonstrates that arbitrarily long chains can still maintain reliable signal propagation. A faster average switching time of approximately 330 ps per nanomagnet can be extracted from this figure due to the longer shapes. Based on our simulations and predictions made in other works, switching times of a few hundred picoseconds with a lower bound of 100 ps can be expected from NML architectures based on coupled magnetic islands.

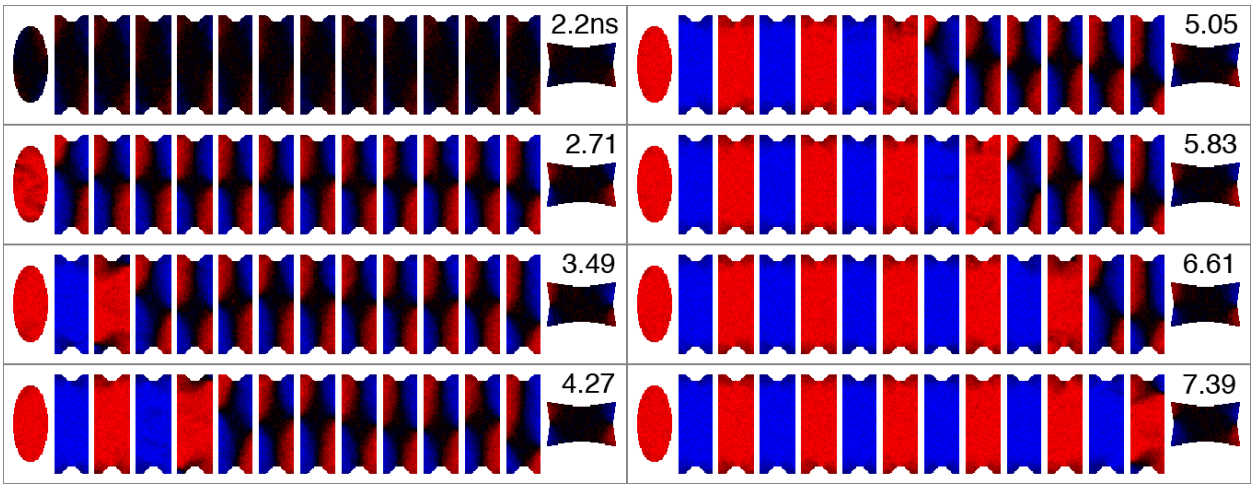

Figure 5. 23: Time-delay snapshots of an OOMMF simulation of a chain showing an average switching time of 390 ps. Simulation performed at 300 K with piecewise linear clock field.

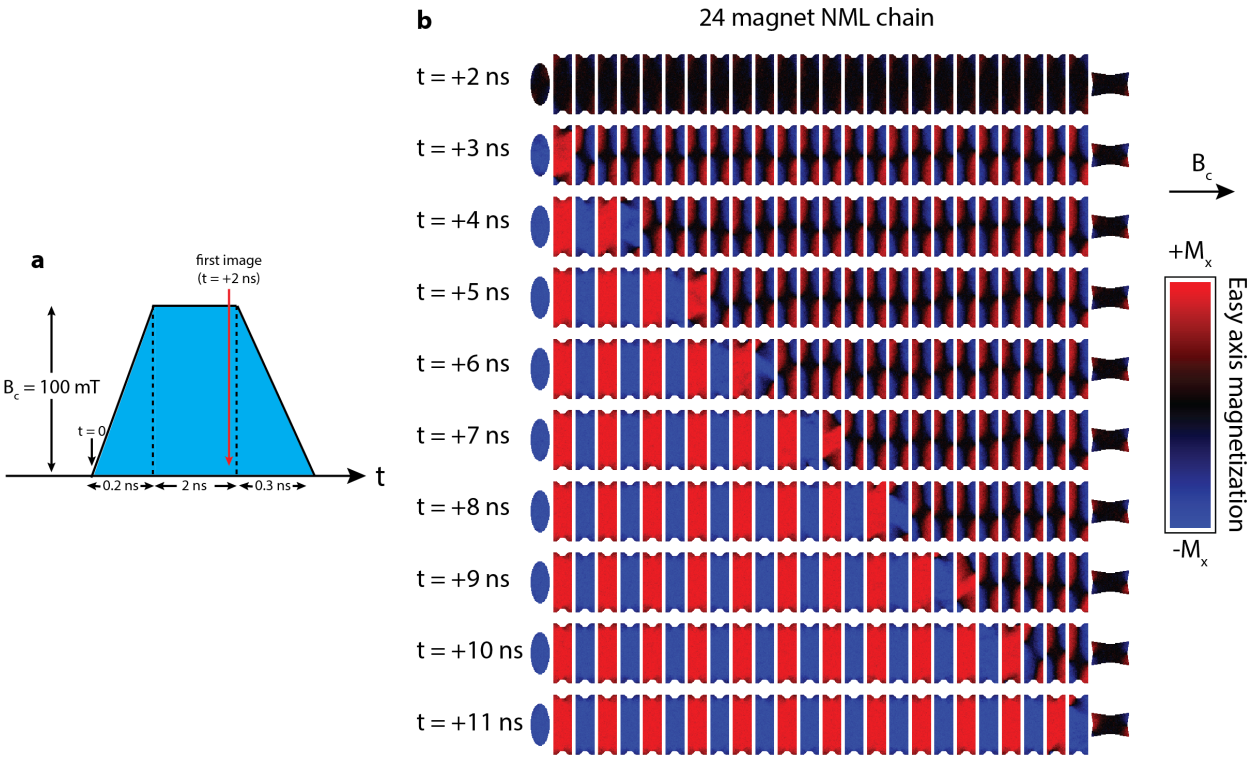

Figure 5. 24: Extension of figure 5.23 toward longer chains. Clock field pattern (left) and time-delay OOMMF snapshots (right) are shown for a 24-magnet chain.

Chapter 6. Static Experimental Methods for Investigating Nanomagnetic Logic

1. X-ray Magnetic Circular Dichroism

X-ray Magnetic Circular Dichroism (XMCD) is a physical effect that allows for the optical probing of spins[53]. Experimental techniques employing XMCD are powerful due to the potential for fine spatial (less than 50 nm) and time (less than 100 ps) resolution combined with non-destructive measurement. At a simplified level, XMCD is the spin-dependent difference in absorption of circularly polarized x-rays in a spin-polarized material. Figure 6.1 gives a more detailed picture of the process for the specific set of materials following the $2p^6 3d^n$ to $2p^5 3d^{n+1}$ transition. An atom may absorb a photon to excite a core-level electron to the valence band. Due to the electric dipole selection rules (LaPorte rules), the spin-preserving transitions between unlike orbitals are allowed through circularly polarized photons, which contribute the conserved angular momentum. The valence band spin splitting as a result of magnetism causes a differing density of available states for transitions of opposite spins. Thus, the transition rate and therefore absorption rate of circularly polarized light becomes spin-dependent. For the $2p_{3/2}$ to 3d and $2p_{1/2}$ to 3d transitions specifically, the designated spectroscopic names are the L_3 and L_2 edges, respectively. Due to spin-orbit coupling, photoelectrons excited through absorption become spin-polarized. Since the spin-orbit coupling for $2p_{3/2}$ and $2p_{1/2}$ are opposite (L+S and L-S), the spin-polarization is also opposite between the two edges. Likewise, reversing the photon helicity also reverses the spin-polarization since the contributed angular momentum is opposite. Therefore, to obtain an XMCD signal that unambiguously detects opposite spins, one must take two measurements between which the spin (magnet) is reversed, the photon helicity is reversed, or a complementary absorption edge is used. The amplitude of the XMCD signal depends on the expectation value of the valence band magnetic moment, the degree of circular polarization of the x-rays, and $\vec{J} \cdot \vec{m}$ where $\vec{J}$ is the photon spin angular momentum and $\vec{m}$ is the magnetic moment. The last-mentioned dependence is derived from symmetry arguments and in effect requires that the magnetic moment have a projection along the optical beam axis. Optical absorption follows the Beer-Lambert law[53] for transmittance T through a material of thickness l and absorption coefficient Σ for light intensities I:

$$T = \frac{I}{I_0} = e^{-\Sigma l} \tag{6.1}$$

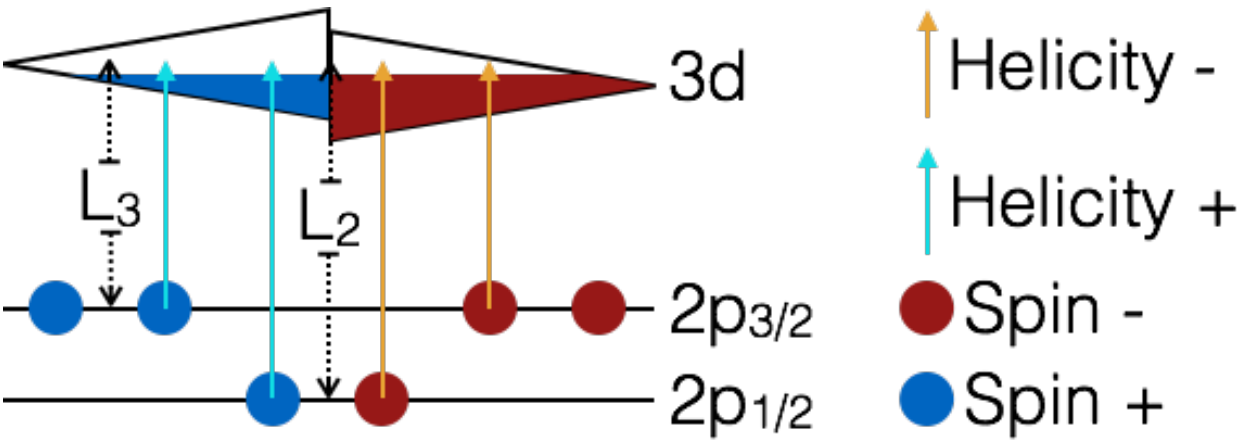

Figure 6. 1: Cartoon of circularly polarized optical transitions in magnetic materials.

Therefore the XMCD signal, which is the difference in spin-dependent absorption coefficients, is recovered by dividing the resulting intensities of the two measurements and then taking the natural logarithm.

We describe the relevant pair of XMCD imaging techniques below. The former is magnetic transmission x-ray microscopy[54] (MTXM). MTXM is a straightforward application of the Beer-Lambert law in which x-rays pass through a magnetic film and attenuate by varying amounts due to the spin-dependent absorption coefficient. An x-ray sensitive camera captures the resulting intensity to form a direct mapping of the transmittance. Figure 6.2 shows a possible configuration, specifically that of XM-1 at the Advanced Light Source (ALS). This tool uses a zoneplate, a diffractive optical element analogous to a lens, to focus x-rays through a pinhole. Since each wavelength has a different focal length, moving this zoneplate with respect to the pinhole in effect acts as a monochromator. The x-rays of the selected wavelength then pass through and attenuate in the sample, where the addition of XMCD forms a magnetically sensitive image. A second zoneplate focuses this image onto a charge-coupled device (CCD), which captures the image.

The latter is Photo-Emission Electron Microscopy[55] (PEEM). PEEM utilizes the

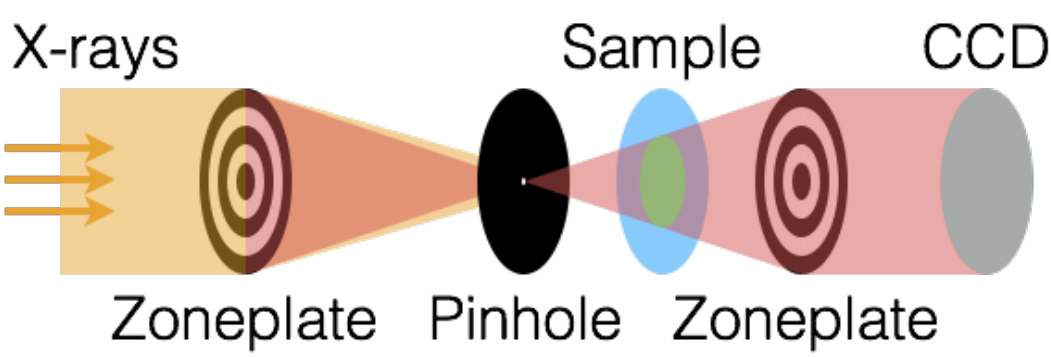

Figure 6. 2: Schematic of XM-1 at the ALS.

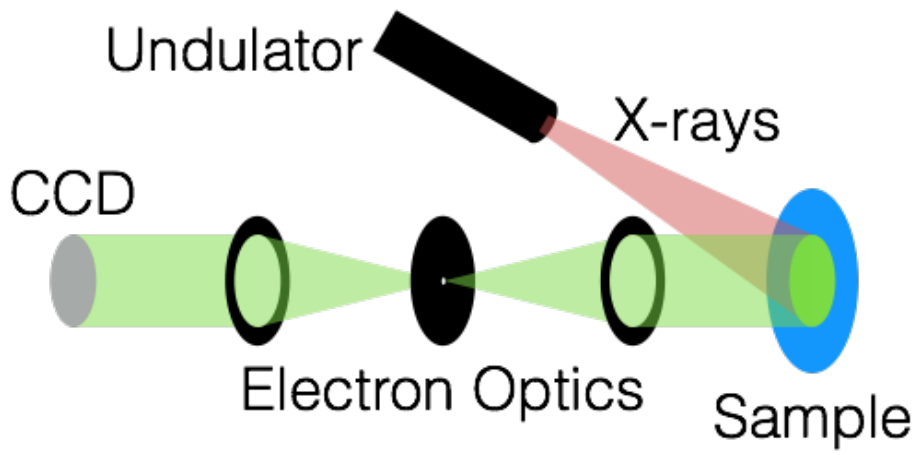

Figure 6. 3: Schematic of PEEM-3 at the ALS.

probability of Auger relaxation of excited photoelectrons, in which some of its energy is transferred to another valence band electron to ionize it into vacuum. From these electrons, inelastic electron scattering further produces ionized electrons, some of which eventually escape the sample surface. It follows that the higher the spin-dependent absorption rate, the more of these electrons are emitted. Electron optics collects these electrons to form an image and focuses it onto a CCD, which captures the image. The ionized electrons travel only a few nanometers in the sample and thus this technique is sensitive only to spins close to the incident surface. Unlike MTXM, PEEM requires a vacuum for the electron optics, but does not require thin, non-opaque samples. Figure 6.3 shows a possible configuration, specifically that of PEEM-3 at the ALS. This tool uses an undulator to provide both polarization control and wavelength selectivity.

2. Thermally Assisted Signal Propagation in Chains

Experimentally demonstrating signal propagation in chains is possible as long as the time scale of measurements is smaller than the time scale of signal propagation through the chain. In this case, a thermally assisted signal propagation process is potentially slow enough for static measurement techniques (with image acquisition times on the order of seconds to minutes). We designed such an experiment[18,46] to verify the possibility of cascade-like signal propagation behavior in chains of anisotropy-engineered nanomagnets. We patterned a sample of chains with 10 nanomagnets per chain, each 150 nm wide and between 300 nm and 450 nm long (all nanomagnets in an individual chain besides the input and block have the same dimensions). This wide range of lengths assures us that at least some chains will show signal propagation on the desired timescale. The gap between nanomagnets was 30 nm and the depth of the indentations was 50 nm. As a control, we also included ellipse-shaped nanomagnets of similar dimensions. This pattern was exposed by electron beam lithography onto PMMA spun on a silicon substrate. 1 nm of

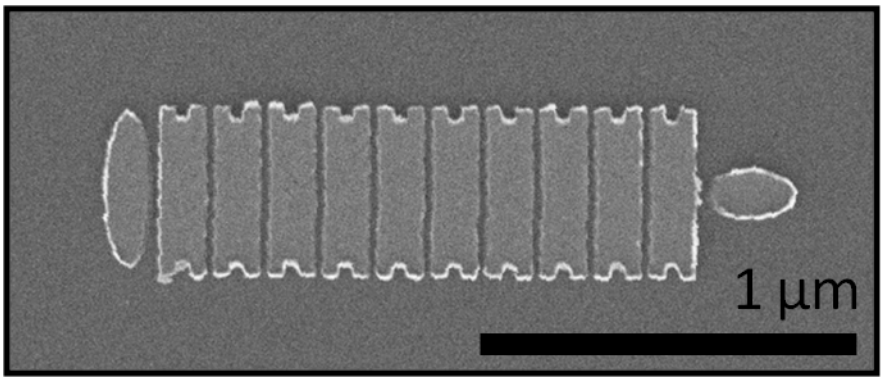

Figure 6. 4: SEM of a chain deposited onto Si, with input on the left and block on the right.

titanium, 13.4 nm of permalloy, and 2 nm of aluminum were then evaporated onto the pattern followed by lift-off in heated Remover PG. Figure 6.4 shows an SEM of one of the chains.

We applied a clock field of 2200 Oe along the horizontal axis of figure 6.4 for approximately 30 s using an external magnet several hours before imaging the sample with PEEM. We captured images of both anisotropy-engineered and ellipse-shaped nanomagnet chains at room temperature. Using the same method of counting as section 5.4, we compiled a plot of average signal propagation distance versus the aspect ratio (length over width) of the magnets in the chain. This plot, shown in figure 6.5, compares anisotropy-engineered (denoted 'concave' in the plot) magnets and ellipse-shaped magnets. Anisotropy-engineered magnets appear to perform better, though we recognize that magnets of the same aspect ratio but of different shapes are not necessarily directly comparable. Specifically, we note that the range of sizes for anisotropy-engineered

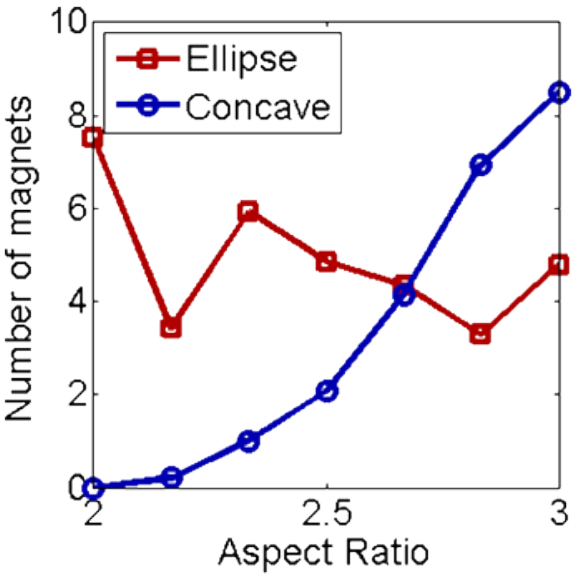

Figure 6. 5: Average signal propagation distance vs. aspect ratio of slowly-clocked chains.

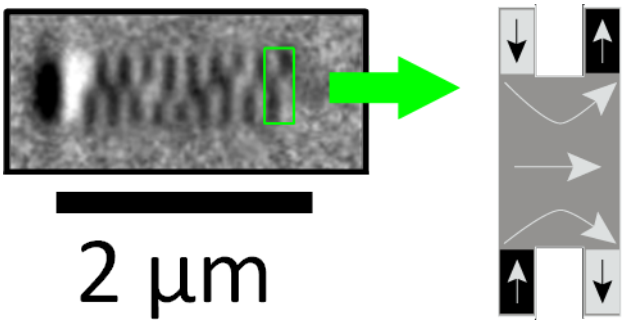

Figure 6. 6: PEEM magnetic contrast image with interpretation of a chain of anisotropy-engineered nanomagnets, of which most are in the neutral state.

magnets cover a portion of the optimal region mentioned in section 5.4. A rigorous (though likely too exhaustive to be experimentally practical) comparison would directly compare the optimal regions for each shape. However, we note that the results for these ellipse-shaped magnets are similar to those studied earlier[7,47] with aspect ratios near 1.5. Furthermore, other studies have also suggested[7,8,18,43,44,46,47] that signal propagation distances are fairly limited in chains of nanomagnets employing standard ellipse geometries. Figure 6.6 shows a magnetic contrast image of a chain displaying direct evidence of the neutral state. This image shows the same domain pattern (derived from the flower state) as predicted in the micromagnetic simulations from section 4.3. This result demonstrates that we achieved the goal of anisotropy-engineering our nanomagnets: to create a stable energy well for the neutral state. Since we applied our clock field several hours before this measurement, these neutral states are stable for at least several hours. To increase the rate of thermally-assisted switching, we heated the sample stage to 120° C. We then imaged the sample periodically (with acquisition time of less than 60 s) to observe thermally-assisted signal propagation over the timescale of hours. The mechanism is as follows: all neutral state magnets with both neighbors also in the neutral state remain stable along the neutral axis for very long timescales. However, if either neighbor switches, its stray field acts to lower one energy barrier (of the neutral axis energy well) and raise the other. According to the equation 3.22, the magnet has a higher probability of hopping over the smaller energy barrier. The experiment is designed such that at room temperature, even this state is stable for hours. However, at 120° C, the magnet hops over the smaller energy barrier at an average rate of several times per hour. Note that we assume and expect all ellipse-shaped magnets to have switched as the clock field was removed, and to no longer switch afterward, even at 120° C. Since the ellipse-shaped input magnets of the anisotropy-engineered chains have mirror symmetry with respect to the axis of the clock field, they effectively act as a random bit input.

Figure 6.7 shows magnetic contrast (the gray scale is a projection of the magnetic moment onto the vertical axis) time-lapse images of a chain that operated in this fashion. This result demonstrates cascade-like (as distinct from magnetic field annealed or

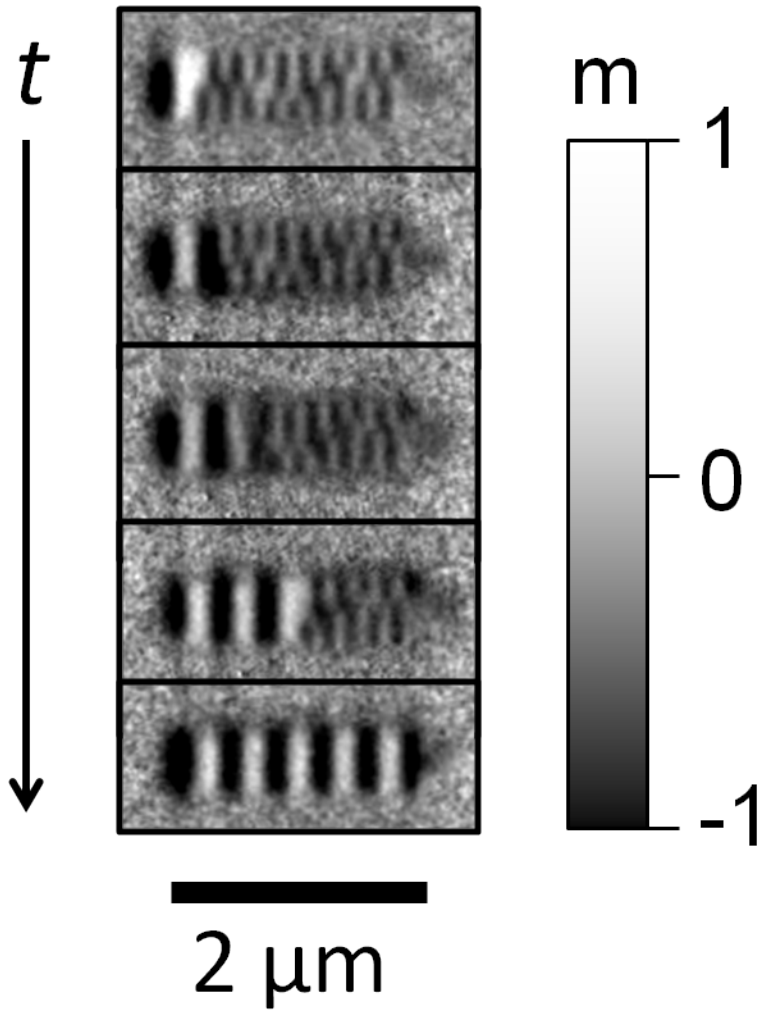

Figure 6. 7: Time lapse PEEM magnetic contrast images of cascade-like signal propagation in a chain. The color scale indicates magnetization along the vertical axis.

thermally driven random walk) signal propagation in chains of anisotropy-engineered nanomagnets as a proof-of-concept. However, several issues limit its usefulness as a practical demonstration. These include the external magnet used for the clock field, the increased temperature required, and the speed of signal propagation. These issues are addressed in follow-up experiments described in later sections, in which room temperature operation using integrated high-frequency clock fields and signal propagation rates near the speed limit are demonstrated.

3. Surface Quality Effects on Signal Propagation

As a step toward integration of clock lines with nanomagnets onto the same sample, we investigated the effects on signal propagation errors from the roughness of the surface

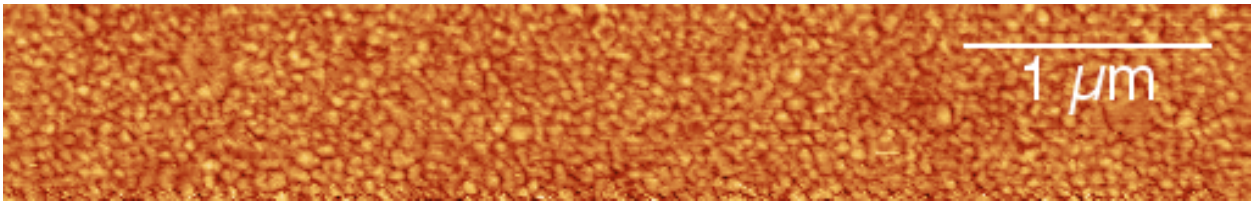

Figure 6. 8: AFM of Cu clock line surface with RMS roughness of 1.6 nm.

interfacing the nanomagnets. We intended to probe chain dynamics at high frequencies using Oersted fields generated by currents in conducting clock lines. This strategy requires that the nanomagnets be deposited onto the clock lines, and other studies[56,57] have mentioned the significance of surface roughness effects. We patterned chains of 12 anisotropy-engineered nanomagnets by a procedure similar to that of section 6.2 except for a permalloy thickness of 12 nm. We deposited these chains onto 6 μm wide, 160 nm thick copper clock lines, which were fabricated by bi-layer lift-off following the procedure in appendix D.1. As a control, we deposited the same pattern of chains onto the substrate, which is 100 nm of silicon dioxide on top of silicon.

Figure 6.8 shows an atomic force micrograph (AFM) of the surface of the copper, the root-mean-square (RMS) roughness of which was 1.6 nm. The roughness of the substrate was lower than 0.25 nm, which is below the resolution of the AFM. Figure 6.9 shows an SEM of a chain deposited over copper, the grains of which are clearly visible. The input magnet has a shape-induced bias toward a particular bit (the overall easy axis has a component parallel to the clock field axis).

We applied a clock field by a procedure identical to that of section 6.2 and then imaged the sample using PEEM to observe the states of chains both on the copper clock lines and on the silicon dioxide substrate. Figure 6.10 shows a direct comparison between chains deposited over the two materials. As an approximate measure of the effects of surface roughness on signal propagation, we compared the number of errors (ferromagnetically aligned pairs of magnets, identified by larger brightly colored white or black spots) observed between chains deposited over the two materials. We found that chains deposited over the rougher material indeed show a significantly larger number of errors.

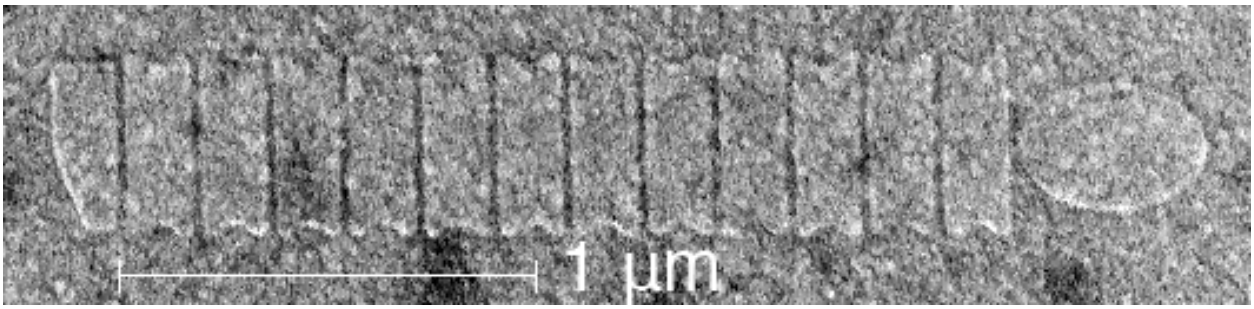

Figure 6. 9: SEM of a chain deposited onto Cu.

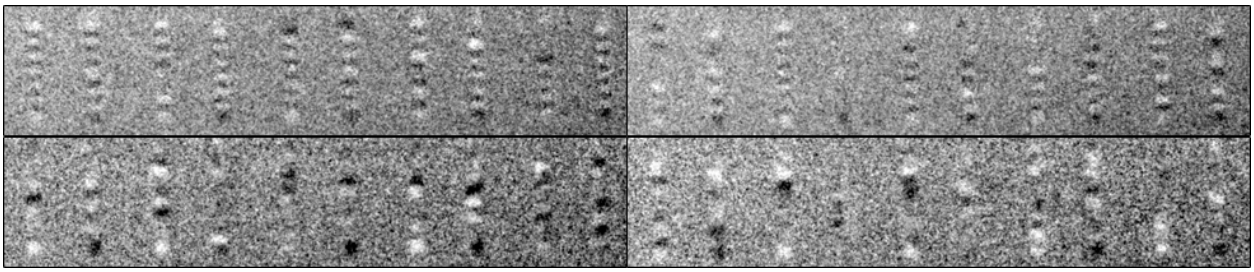

Figure 6. 10: PEEM magnetic contrast images of chains (with chain axis oriented vertically) deposited over the SiO_2 substrate (top) and the Cu clock lines (bottom).

The capacity for improving the surface roughness of thick evaporated films is fairly limited. Instead, we chose to planarize the clock lines by depositing a thin (enough so that the clock field magnitude is still sufficient) layer of additional material on top. Following the procedure in appendix D.2, we fabricated gold clock lines by bi-layer lift-off and spun aluminum oxide phosphate (AlPO) on top to planarize the surface. We switched to gold due to its ability to accommodate the higher thermal budget necessary for curing the spin-on dielectric (copper oxidizes and peels off well below the curing temperature). Figure D.6 shows an AFM of the surface of the gold with spin-on dielectric, the root-mean-square roughness of which was 0.3 nm. Figure 6.11 shows an SEM of a chain deposited over the improved clock line.

We deposited the same pattern of chains onto 160 nm thick gold clock lines with a 45 nm spin-on dielectric planarizing layer (such that the control chains are now on top of spin-on dielectric over silicon dioxide, though we do not expect any significant differences in this regard). We applied the clock field and imaged using PEEM using the same procedures as the copper sample. Figure 6.12 shows the comparison of chains deposited on spin-on dielectric over silicon dioxide and over gold. Note that this figure is not directly comparable to figure 6.10, since a separate fabrication run results in slight lithographic differences. We found that chains deposited over both materials in figure 6.12 contained a far more similar number of errors. We thus confirmed that planarizing the surfaces upon which NML is deposited is critical.

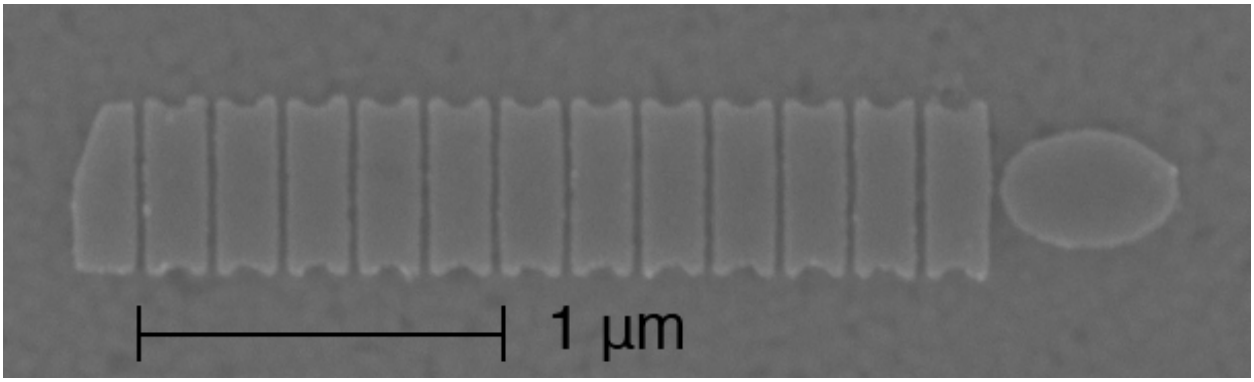

Figure 6. 11: SEM of a chain deposited onto an AlPO layer covering Au.

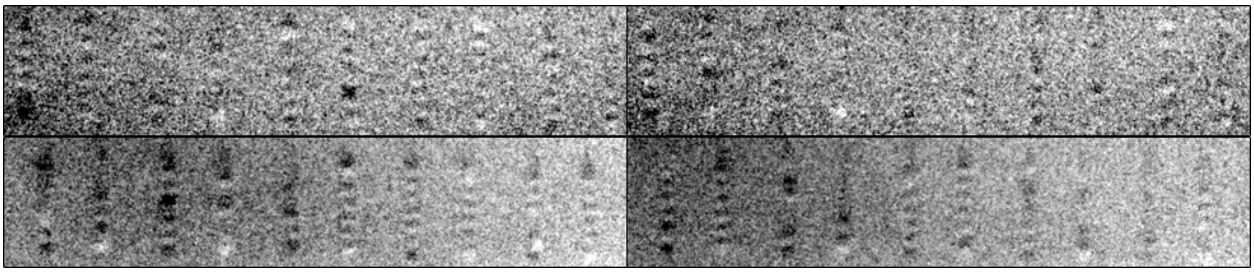

Figure 6. 12: PEEM magnetic contrast images of chains deposited on AlPO over SiO_2 (top) and AlPO over Au clock lines (bottom).

4. Signal Propagation from Short Clock Field Pulses

An alternative to surface planarization is deposition of NML directly onto the substrate and subsequent patterning of the clock lines. If the substrate is thin, a backside or transmission measurement can probe the magnets. We conducted a transmission experiment using MTXM to measure the magnetic states of chains after subjecting them to short clock field pulses. We patterned using electron-beam lithography and lift-off chains of 1 nm titanium and 12 nm permalloy using the same 12-magnet pattern with biased input as in section 6.3 onto a silicon wafer with 100 nm of low stress silicon nitride (Si_3N_4) on both sides, then deposited 6 μm wide clock lines over them by lift-off. The clock lines were comprised of a 1 nm titanium adhesion layer, 150 nm of an alloy of 96% aluminum and 4% copper, and a 10 nm copper capping layer. Aluminum combines a fairly high conductivity with a low atomic number, which was ideal for our experiment in order to provide the largest currents with minimal x-ray absorption. Alloying aluminum with copper increases its resistance against electromigration[58]. The copper capping layer protects the

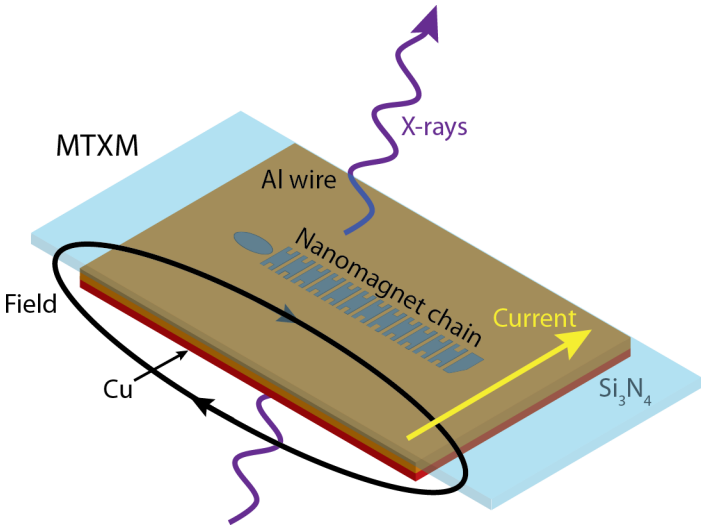

Figure 6. 13: Cartoon of MTXM sample geometries.

aluminum from the alkaline protective coating and its remover solution mentioned below. The side of the wafer on which the above processing is done is designated the front side.

To thin the substrate to a silicon nitride membrane suitable for transmission measurements, we etched the silicon from the back side in the shape of square windows such that the frames of the windows mechanically support the sample. To achieve this, we first coated the front side with ProTEK B3 alkaline protective coating, and then patterned the windows onto the back side. This protective coating withstands many room-temperature acids and heated bases. Next, we etched the windows from the back side silicon nitride using an acid dip. Either phosphoric acid (H_3PO_4) or buffered hydrofluoric acid (HF) works. After removing the photoresist from the back side, the silicon nitride acts as an etch mask for the silicon substrate. We etched the silicon using heated potassium hydroxide (KOH) anisotropic wet etch, which selectively stops on silicon nitride. Finally, we stripped the alkaline protective coating using ProTEK Remover 100. This fabrication process was developed and performed by the nanofabrication laboratory at the Center for X-ray Optics. Figure 6.13 shows a diagram of the relevant section of the sample, including order of material layers and electric current, Oersted field, and x-ray directions.

We mounted samples into a pocket machined out of a Rogers 4350B printed circuit board (PCB). Silver-plated copper traces on the PCB ran to the edge of the pocket. SPI flash-dry silver paint served both as electrical contacts between the traces and the clock lines on the sample as well as mechanical anchors. An edge-mount SMA connector soldered onto the PCB allowed for direct interfacing with pulse generators. The electrical resistances of the samples averaged 21 Ω. We operated the clock lines in a single-shot fashion by manually triggering an AvTech AVM-4 pulse generator at the largest voltage and pulse width available. Figure 6.14 shows a single-shot voltage pulse delivered to the clock lines as measured (and scaled appropriately) from the monitor output of the pulse

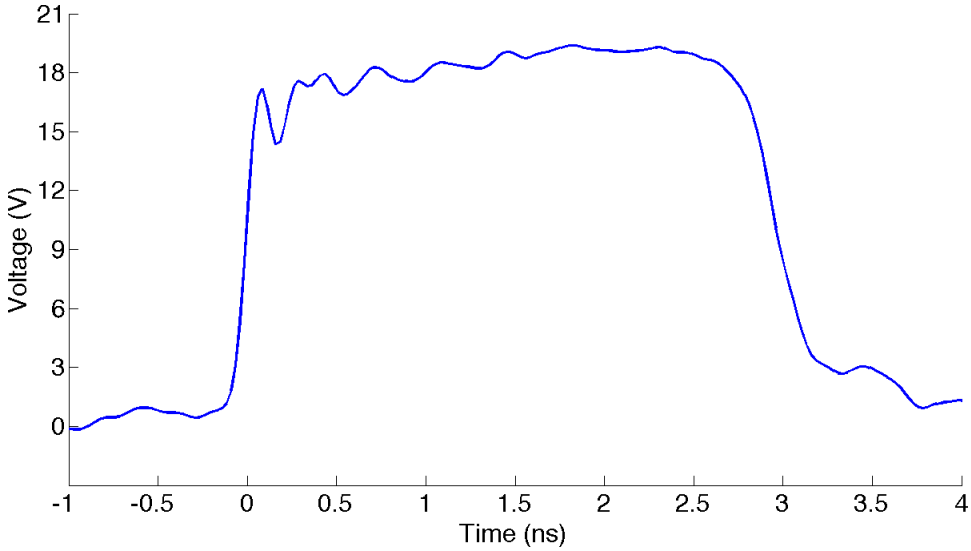

Figure 6. 14: Voltage pulse delivered to clock lines as measured on oscilloscope.

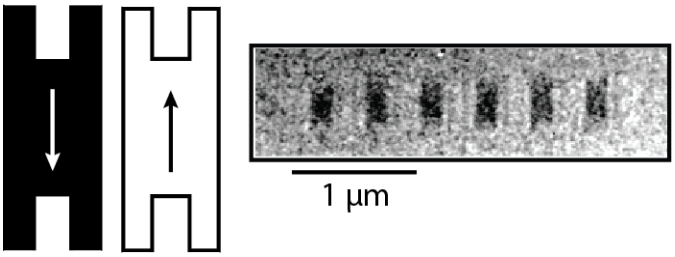

Figure 6. 15: Saturated-reference MTXM image of chain showing correct final state. Areas magnetized 'up' appear to blend into the background.

generator. Due to the close proximity of the magnets to the clock lines, a near-field calculation of the Oersted field is valid. The 18.5 V voltage pulses correspond to 880 mA current pulses. Using the superposition integral[24] (Biot-Savart Law), we calculated the corresponding clock field to be 84 mT. We mounted the sample at a $\frac{\pi}{6}$ tilt from normal incidence, which provides ½ the maximum magnetic contrast (when $\vec{J} \parallel \vec{m}$) but distorts images such that magnets appear $\frac{1}{\sqrt{2}}$ as long.

Several methods of exposing and comparing a pair of images produce magnetic contrast. First, we may reverse the helicity of the x-rays. Without an undulator, this is difficult and may be achieved in part by capturing light from only the top or bottom half of the beam. Since the path of the beam through the optics changes, the illumination pattern on the sample also changes. When the images are compared, the background signals also contribute and thus make interpretation more difficult. Second, we may use both complementary absorption edges. This method suffers the same problem, as the zoneplate is forced to move to shift the focal point and thus the beam takes a different path through the optics. Third, we may switch the magnets. This method produces the best image quality given the helicity constraints.

We use an external electromagnet to saturate all nanomagnets along a particular direction and take a reference image. We then clock the chains by triggering the pulse generator and take another image. Per-pixel dividing the images then shows the areas that are magnetized differently from the saturated state. Figures 6.15 and 6.16 show magnetic contrast images using this method at the iron L_3 edge for an earlier generation of samples containing chains of only 7 nanomagnets which, due to their thickness of 16 nm, produced

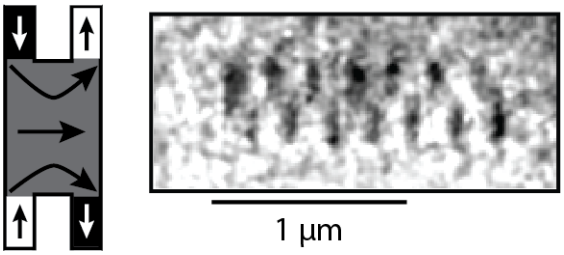

Figure 6. 16: Saturated-reference MTXM image of chain showing neutral state.

the best images. Figure 6.15 shows an example of a chain that correctly propagated a signal, while figure 6.16 shows an example of a chain that remained completely in the neutral state.

A severe issue with the ferromagnet-core electromagnet that was available to us is that the small amount of remanence of the electromagnet core produced a magnetic field large enough to significantly skew the results of signal propagation. An air-core electromagnet would not have any remanence, though would produce less magnetic field. The saturated-reference method is still useful for determining whether the clock fields are sufficient in magnitude and duration to switch chains to the neutral state. If so, some magnets in the chain would switch out of the neutral state such that they are reversed in comparison to their previously saturated state. Magnets that remain in the neutral state also signify sufficient clock fields. We confirmed this in our latest generation of samples, but opted to use the reversed-helicity method due to the effects of electromagnet remanence and accept the more-difficult-to-interpret images that it produced. The sample contained a range of nanomagnet lengths and two chains per value of length. We clocked each pair of chains 10 times and imaged with both helicities after each clock cycle. Image acquisition times were approximately 30 s with the time between clocking and imaging on the same order of magnitude (image acquisition began a few seconds after clocking). Image processing was performed using the program from appendix B.2 and techniques were restricted to sub-pixel alignment, brightness and contrast adjustments, and median noise or Gaussian blur filters. We acquired these statistics for two samples cut from different locations on the same wafer.

Figure 6.17 shows the average signal propagation distance calculated by the same method as section 5.4. Sample 2's curve resembles those of section 5.4, showing the

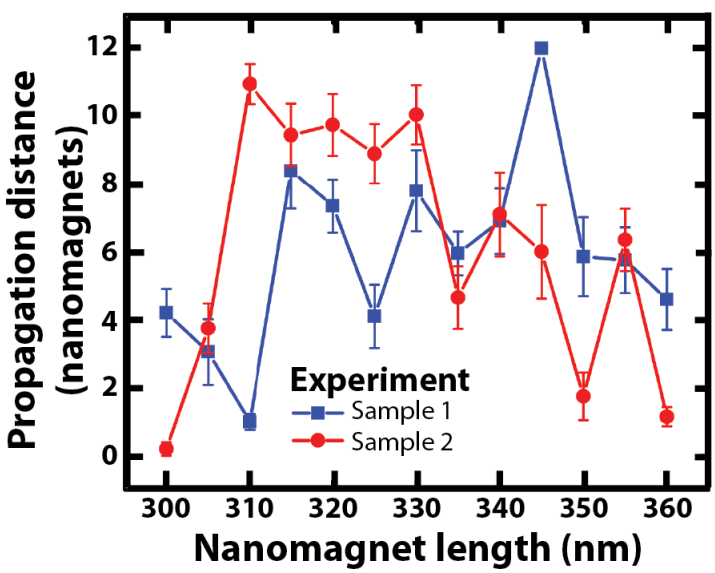

Figure 6. 17: Average propagation distance in chains clocked by 3 nanosecond pulses. Each data point is an average over 2 chains and 10 clock cycles.

optimal range of nanomagnet lengths corresponding to a segment of the optimal region of anisotropies. Sample 1's curve has less resemblance but contains a particular pair of chains of the same nanomagnet lengths that exhibit perfectly reliable signal propagation. We attribute the poor performance consistency to lithographic variations from magnet to magnet as well as sample to sample. However, we do demonstrate a significant improvement in propagation distance for short clock field pulses using cascade-like behavior. This overcomes the predictions of other works[47,49] that showed very large error rates in long chains of ellipse-shaped nanomagnets paired with short clock field durations, particularly beyond five magnets and several μs. Furthermore, it is clear from this data and the design shown in section 5.5 that there is still much room for improvement in both sample processing and geometric design. A signal propagation dynamics experiment using the samples from this section was intended, but the signal-to-noise and signal-to-background levels proved to be too low. Instead, we performed this experiment using PEEM and an alternate sample geometry, described in section 7.2.

5. Magnetic Force Microscopy

Magnetic Force Microscopy (MFM) is a variation on AFM that employs a tip coated with magnetic material to sense magnetic fields produced by a sample. MFM provides fairly high (less than 50 nm) resolution but is not straightforward to interpret because the tip interacts with the sample and can easily disturb the magnetic states of material on the sample. We used low magnetic moment tips coated with 2 nm of cobalt chromium to minimize this effect. The MFM tip scans each scan line in an image twice. On the first pass, the oscillating tip taps the sample while scanning and detects contributions from atomic and magnetostatic forces. On the second pass, the tip lifts up and no longer contacts the sample, detecting only magnetostatic contributions. By comparing the information from the two passes, this method greatly reduces image sensitivity to sample topography. We

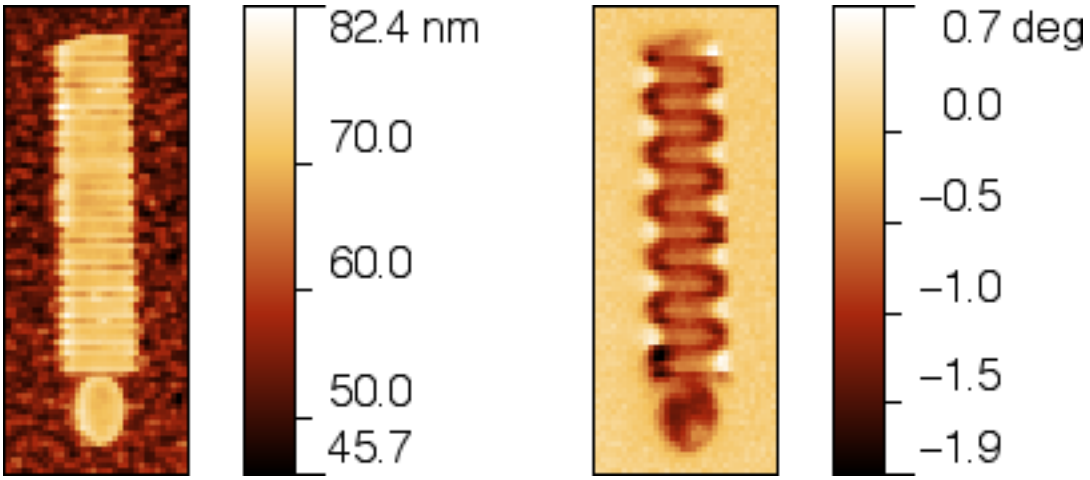

Figure 6. 18: MFM topography (left) and magnetic contrast (right) images of a chain.

detected magnetostatic forces by measuring the oscillation phase of the tip, though other methods of detecting magnetic interaction between tip and sample exist.

In order to perform a signal propagation dynamics experiment using PEEM as in section 7.2, we must use a sample geometry that deposits the magnets onto the surface where x-rays are incident. Therefore, we chose to use a sample prepared as in figure 6.11 where the surface of the clock lines were planarized using spin-on dielectric. We delivered a 100 mT clock field pulse of duration 2 ns using the clock lines and measured the resulting state of the chains by MFM. Figure 6.18 shows both topography (as an AFM would measure) and magnetic contrast images of a chain that showed successful signal propagation. We attribute the background roughness of the topography to PMMA residue from the liftoff process. It is clear by comparing the images that this residue does not contribute any significant magnetic signal. In the magnetic contrast image, we see that MFM detects the locations of the magnetic poles in each magnet, and distinguishes north and south poles by phase. Each magnet shows a bright and dark spot at opposite ends of the easy axis, corresponding to the magnetic poles. We also observe several poles in the ellipse-shaped block magnet, indicating domain structure. This suggests that the anisotropy strength of the block could use improvement. We never observed the domain structure of the neutral state, most likely due to magnetic interaction between the MFM tip and the permalloy. Even the low magnetic moment tip can switch magnets that are in the

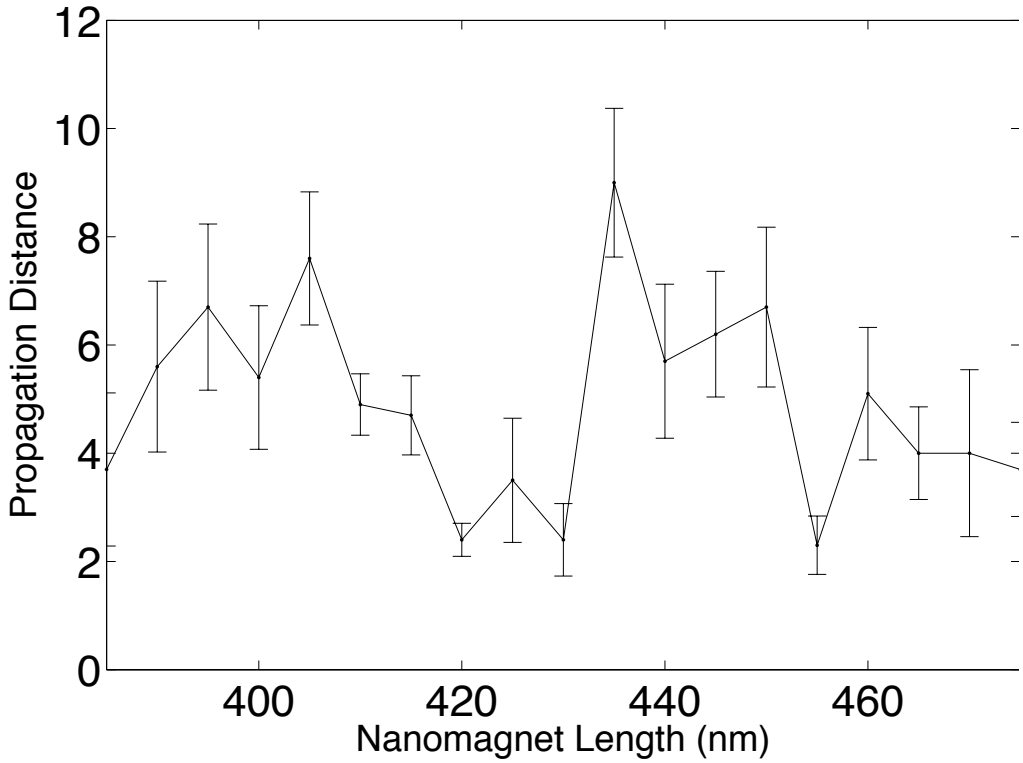

Figure 6. 19: Average propagation distance in chains clocked by 2 nanosecond pulses. Each data point is an average over 2 chains and 5 clock cycles.

neutral state. For this reason, MFM is far from ideal for studying NML containing weakly stable magnetic states. However, it is sufficient as a supporting measurement to help verify that a sample is capable of exhibiting signal propagation. We clocked this sample 5 times and measured the magnetic state of the chains using MFM several hours after each clock cycle.

Figure 6.19 shows the average signal propagation distance calculated by the same method as section 5.4. It is apparent by comparison with figure 6.17 that the chains on this sample perform fairly unimpressively. The fabrication method used for these samples may have contributed additional complications. For example, since the aluminum capping layer does not cover the permalloy sidewalls, the magnets can oxidize close to the sidewalls. Additionally, the amount of PMMA residue may suggest other potential processing issues. Nevertheless, we found a few individual chains (no two chains of the same length) that showed consistently high signal propagation distance, suggesting that further engineering work is capable of significantly improving performance.

Chapter 7. Dynamic Experimental Methods for Investigating Nanomagnetic Logic

1. Stroboscopic X-ray Magnetic Circular Dichroism

Stroboscopic methods, also known as pump-probe, provide the ability to take time-resolved measurements as long as the acquisition time is less than the time resolution needed. They achieve this by controlling the time delay between excitation (pump) of the sample and measurement (probe), and then consistently repeating the pump-probe cycle with the same time delay. As a result, the state of the sample at that particular time delay with respect to the excitation is measured many times. Therefore, any random effects are effectively averaged over many cycles so that only effects with better than random probability manifest. If the time delay is then scanned as an independent variable, the average time response of the sample is measured. Figure 7.1 shows a schematic of the structure of stroboscopic methods.

The ALS can operate in a mode called 'two-bunch' to accommodate stroboscopic experiments[59]. In this mode, the storage ring contains two groups (bunches) of travelling electrons, where each bunch is equivalent to 17.5 mA charge current. The x-rays produced by each bunch are used as the probe, and each bunch has a pulse duration of 60 ps and a delay (repetition period) of 328 ns from the previous bunch. Therefore, a pump triggered by the bunches with a controllable trigger time delay is needed to perform stroboscopic measurements. The typical 'multi-bunch' storage ring mode has an equivalent charge current of 500 mA, so 'two-bunch' mode only offers 7% of the typical x-ray intensity. This poses significant signal-to-noise challenges that must be considered when performing stroboscopic measurements. Both MTXM and PEEM can be operated in a stroboscopic fashion. However, given the already constrained state of magnetic contrast in MTXM images of our samples, the only option to obtain useable images would have been to use significantly thicker magnets (to such a degree that very different behaviors would result). In addition, simply scaling up image acquisition time was not feasible at the XM-1

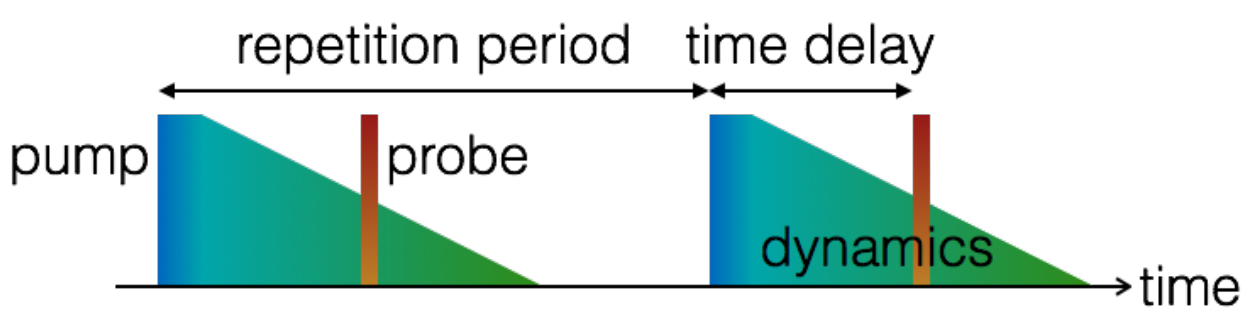

Figure 7. 1: Cartoon of the structure of stroboscopic methods.

due to drift of the x-ray spot position. Though MTXM would have been the simpler technique due to the air ambient, we instead chose to use PEEM for stroboscopic measurements.

The high vacuum ambient of PEEM presents several significant challenges with respect to electrically pumping a sample. The electron optics at the PEEM-3 are held near electrical ground while the sample itself is charged beyond -15 kV. Catastrophic damage to the sample, sample holder electronics, and electronics connected from outside vacuum can occur from arc discharge. Therefore, samples must be exceptionally clean and sample holder electronics must be shielded from the electron optics using a conducting cover. In addition, the high-voltage electrical feedthroughs at PEEM-3 terminate in fairly lengthy sections of bare wire that contact the sample holder. Consequently, very short electrical pulses cannot be delivered from pulse generators outside vacuum to the sample due to distortion. Furthermore, sample holder heating in vacuum must be properly compensated for using an appropriate heatsink. Otherwise, not only might sample holder electronics be damaged, but also the resulting increase in outgassing can significantly degrade image quality. The primary mechanism for this effect is carbon contamination[60], where carbonaceous molecules adsorb onto the sample and optics surfaces in a process driven by exposure to high-energy photons. The next section describes the choices we made to address these challenges in an electrically pumped and optically probed experiment.

2. Time-Resolved PEEM Experimental Setup

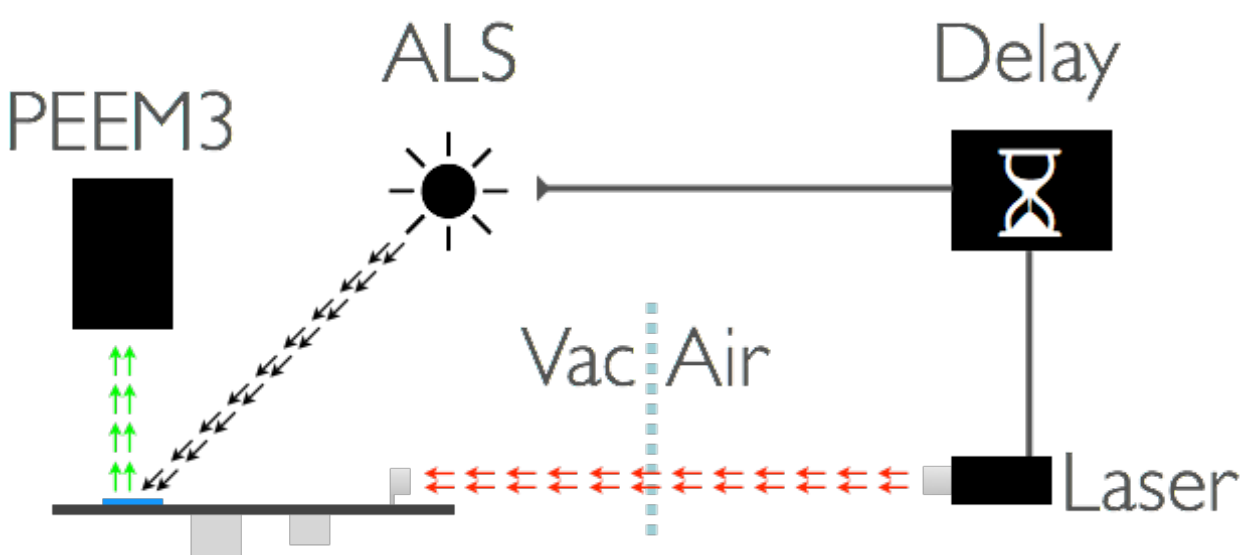

Figure 7. 2: Cartoon of our opto-electronically pumped stroboscopic PEEM setup.

In order to minimize distortion of electrical pump pulses, we bypassed the PEEM-3 electrical feedthroughs by using an optical link between the vacuum chamber and the outside ambient that transmits through an optically transparent chamber porthole. Optoelectronics mounted into the sample holder amplified the optical pump signal into an electrical pump signal. We chose to use the Finisar HFE6392-761 vertical cavity surface emitting laser (VCSEL), which is a high-speed (12.5 Gbps) 850 nm wavelength laser in a compact transmitter optical sub-assembly (TOSA) package. The package is designed for fiber-coupling, but since we needed to transmit through the chamber porthole, we used a microscope objective lens to focus the laser for free-space coupling. On the receiving end of the free-space link we chose to use the Pacific Silicon Sensor AD100-8-TO52-S1 avalanche photodiode (APD), which is a high-speed (2.8 Gbps) 800 nm wavelength peak responsivity photodiode in a compact transistor outline (TO) metal can package. This package embeds the sensor beneath a glass window and stands on through-hole leads to allow adjustment for straightforward free-space coupling. Figure 7.2 shows a simplified schematic of the experimental setup. The ALS produces an electrical pulse (NIM) for each electron bunch that passes by a designated position, and thus each x-ray pulse is accompanied by an electronic signal that can be used for synchronization. We used this signal to trigger a Stanford Research DG645 delay generator, which can be controlled to vary the time delay between pump and probe. We used the delayed signal (ECL) from the delay generator to trigger an AvTech AVM-1-C-P-ECL pulse generator. We drove the VCSEL with the suitably fast (100 ps rise and fall times) pulses produced by the pulse generator. The infrared light

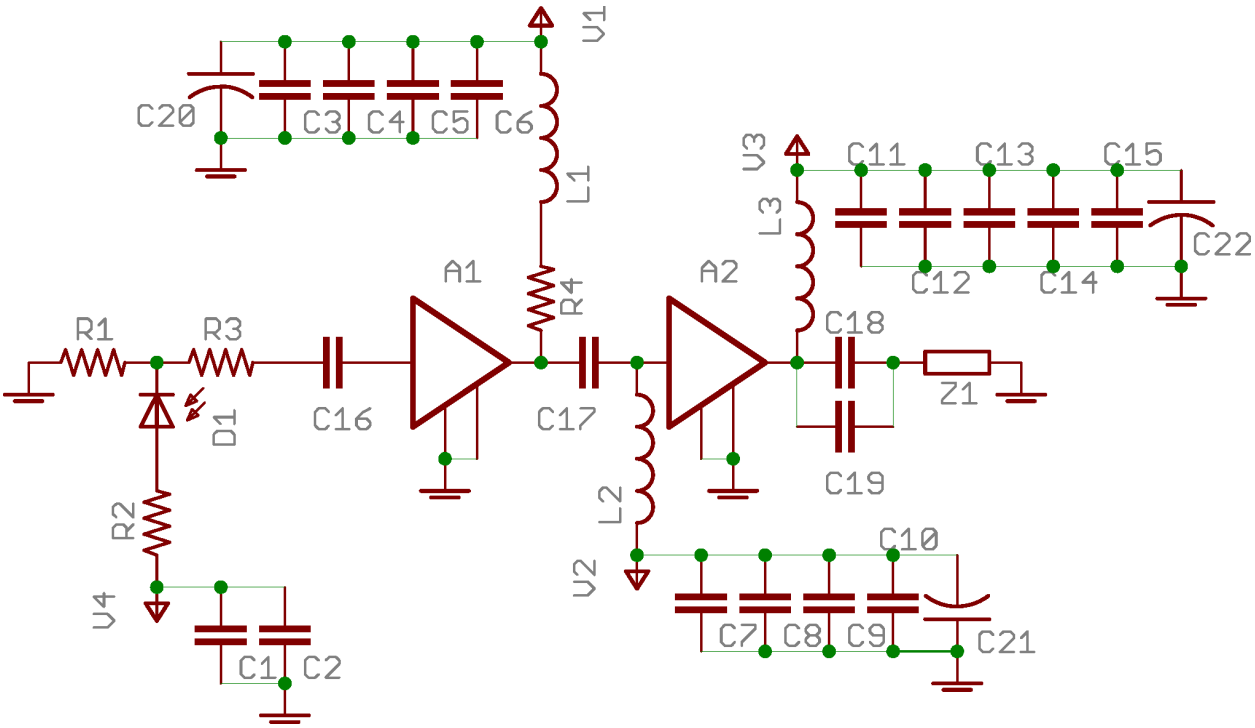

Figure 7. 3: Circuit schematic for pulse amplifier built into the sample holder.

(red) striking the APD produced small currents, which were amplified by sample holder electronics (gray) and pumped through the sample (blue). Meanwhile, x-rays probing the sample generated photoelectrons (green) that were collected by the electron optics.

Figure 7.3 shows a circuit schematic of the sample holder electronics. This circuit is a fairly simple pulse amplifier that does not allow for square-shaped pulses but is physically compact. The APD (D1) drives a sense resistor, whose voltage is amplified by a cascaded combination of a gain amplifier (A1) and a power amplifier (A2). Each stage is separated by a coupling capacitance. All voltage supplies use decoupling capacitors, and voltage supplies which bias amplifiers use choke inductors. The circuit uses 4 voltage supplies in total, which is the maximum number of electrical contacts supported by the PEEM3. Table 7.1 gives the components we used in this circuit. We took many considerations to avoid using materials in the sample holder that outgas carbonaceous compounds, which degrade image quality through carbon contamination. Though most components had ceramic and metal packages, the gain amplifier (A1) came only in plastic packages and was covered-over with Kurt Lesker Torr Seal epoxy before use in high vacuum. The printed circuit board (PCB) was produced by Hughes Circuits using Cirlex (DuPont Kapton) laminate and silver-plated copper layers. The Kapton polyimide laminates outgas less than typical high-frequency hydrocarbon ceramic laminates (such as Rogers RO4000) or Teflon ceramic laminates (such as Rogers RT/duroid). The silver plating helps with adhesion to the lead-free (lead outgasses at elevated temperatures) solder that we used. We chose to use Harris Stay-Brite tin-silver alloy solder with accompanying Harris Stay-Clean liquid flux. We used Kapton-coated wires to connect the sample holder contacts to through-holes on the PCB. Before use in high vacuum, the PCB required a thorough solvent (methanol and isopropyl alcohol) clean and bake-out in a vacuum oven.

D1	Pacific Silicon AD100-8-TO52-S1	C6,C10,C14	100 nF (28+ V)
A1	Hittite HMC476MP86	C15	3 pF (28+ V)
A2	TriQuint T1G6003028-FS	C16,C17	167 pF
R1	430 Ω	C18	47 pF
R2	10 kΩ	C19	8.2 nF
R3	10 Ω	C20,C21,C22	1 μF (28+ V electrolytic)
R4	56 Ω	L1,L2,L3	56 nH (or ferrite bead)
C1	1 nF (150+ V)	V1	7 V
C2	47 nF (150+ V)	V2	-4.2 V
C3,C7,C11	100 pF (28+ V)	V3	28 V
C4,C8,C12	1 nF (28+ V)	V4	-150 V
C5,C9,C13	10 nF (28+ V)	Z1	Sample

Table 7. 1: Component parts and values for circuit in figure 7.3.

Figure 7.4 shows diagrams of the custom sample holder assembly designed to attach to the standard PEEM3 sample holder baseplate (not shown). The sample (blue) electrically contacted the PCB (black) on the top surface via SPI flash-dry silver paint. The APD (green) mounted near the edge of the PCB to avoid being blocked by the aluminum cover (translucent gray). The hole in the cover provided an aperture for the sample to be exposed to x-rays and also for photo-emitted electrons to escape. The cover was electrically grounded to the aluminum sample holder base (dark gray) as well as the baseplate. A layer of kapton (red) acted as an insulating spacer to prevent the cover from electrically shorting the sample. All other electronic components (the amplifiers are light gray in the side view diagram) were soldered to the bottom surface of the PCB. Copper heatsink blocks (orange) with indium foil interfaces conducted heat from the components to the sample holder base and then to the copper nose attached to the end of the base. This nose made direct contact with a liquid nitrogen cryostat filled inside the vacuum chamber in order to keep the electronics at operable temperatures (the baseplates made poor heatsinks). Several design choices (not shown) were also made to assist with alignment issues. The Cirlex PCB was thin and able to flex significantly. We used hard plastic standoffs to ensure that the PCB remained flat and level with the sample holder base. In addition, optimal imaging quality required that the sample be level with respect to the cover and the area imaged be centered within the hole. We adhered a ceramic ring around the sample to help level the cover, and machined slots into the cover to allow for some lateral adjustment. Finally, we attached a textured metal washer around the APD head to scatter laser light. We installed a silicon CCD outside another porthole of the vacuum chamber in order to align the laser more quickly by observing the light scattered from the washer.

The sample design was identical to the gold with spin-on dielectric sample described in section 6.3. The electrical resistance of the sample was measured to be approximately 7 Ω, with voltage amplitudes of up to 7 V (probed using a dummy resistor of equivalent resistance) pulsed across it. Figure 7.5 shows a diagram of the relevant section of the sample. Several experimental operation minutiae are worth mentioning. First, to tweak the alignment of the laser, we measured the current through the drain bias of the power amplifier (A2). Second, the particular power amplifier that we used was normally

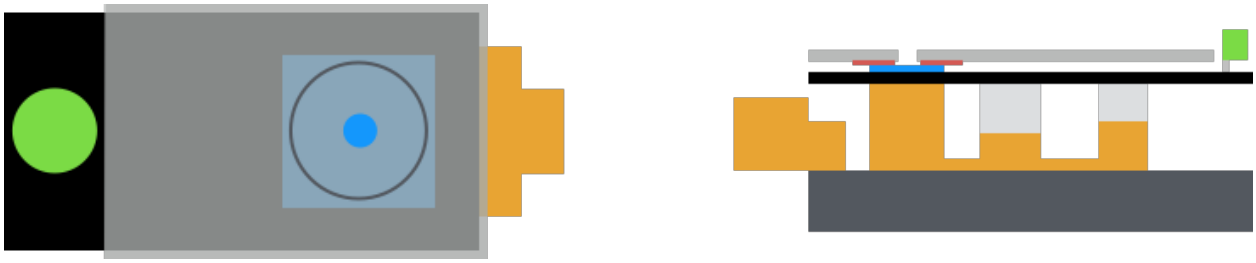

Figure 7. 4: Cartoon of assembled sample holder excluding standard PEEM3 baseplate viewed from the top (left) and the side (right). The baseplate attaches on the bottom.

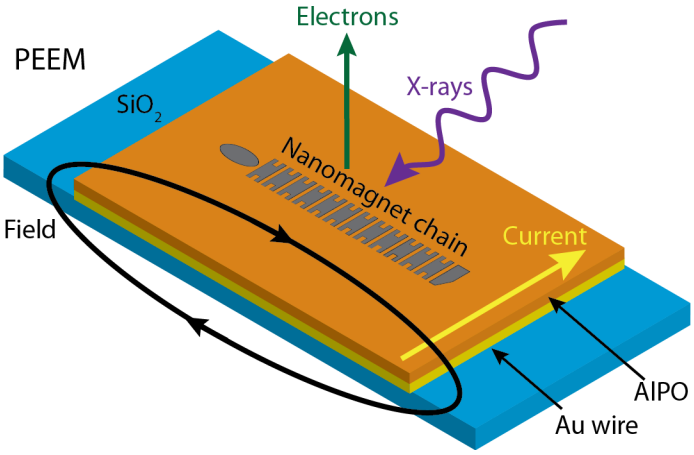

Figure 7. 5: Cartoon of PEEM sample geometries.

on, so that the gate bias (V2) must be applied before the drain bias (V3) to power it up in the off state. Third, the pump pulse had some degree of tunability by varying the pulse width and amplitude of the laser's pulse generator. This provided us some parameter space to tune the balance of pulse width, fall time, and overshoot. Fourth, although a sample temperature probe was not available, we estimated based on the power amplifier's drain current that the sample was near room temperature during measurement. Finally, we sputtered 1 nm of platinum onto the sample prior to measurement to reduce charging, the effects of which are detrimental to image quality.

3. Signal Propagation Dynamics in Nanomagnetic Logic Chains

Using stroboscopic PEEM at the iron L_3 edge, we located the time of the pump pulse by observing Lorentz force effects on photo-emitted electrons. Since the direction of the

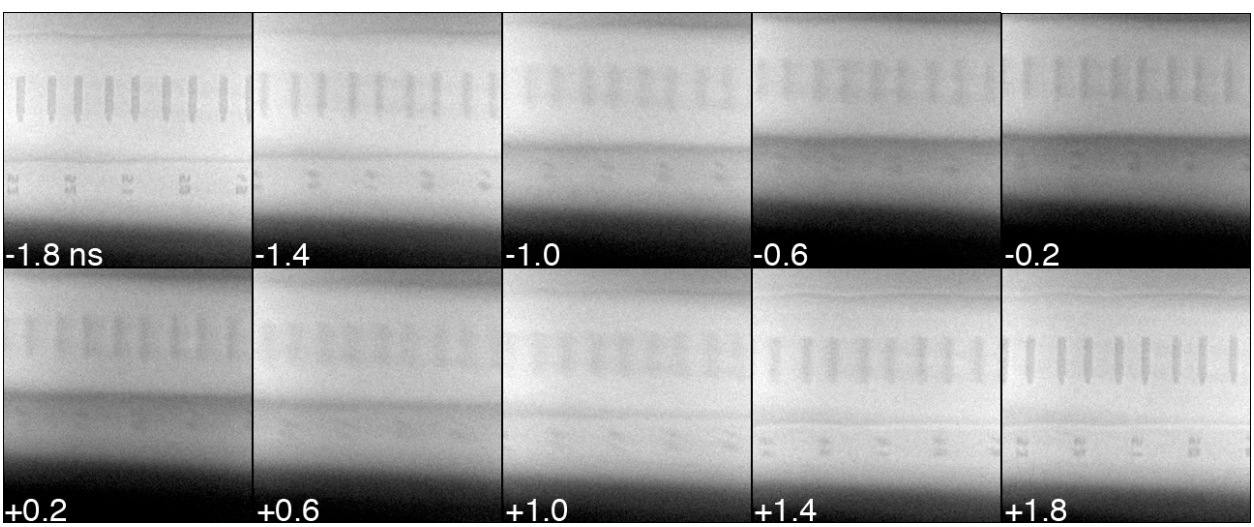

Figure 7. 6: Time-delay raw PEEM images showing Lorentz force effects on imaging.

clock field through which photoelectrons pass was orthogonal to the velocity of the photoelectrons, there was a net drift of the photoelectrons that effectively shifted the image[61]. Two other accompanying effects were apparent as well. The image blurred due to both pump timing jitter and non-uniformity of the photoelectron drift. The image also darkened since the x-ray illumination was optimized for the nominal position and the shifted position had less illumination. Figure 7.6 shows a series of raw PEEM images taken at 10 time-delay steps throughout the main peak of the pump pulse. All image effects mentioned above can be seen, and in addition the illumination change provides a useful characterization tool. We calculated the average illumination of each image and plotted the result versus time delay to obtain the pulse shape, shown in figure 7.7. We understood this to be an approximate representation of the pulse shape, and extracted a pulse width of 2 ns from the plot. It is also worth mentioning that the overshoot was also observed using this method, as shown in the plot. Peak current amplitudes of up to 1 A were estimated for our sample, corresponding to peak clock fields of 100 mT calculated using the superposition integral[24].

Magnetic contrast images were taken using the method of opposite helicities and per-pixel image division as detailed in section 6.4. The sample was mounted at a $\frac{\pi}{6}$ tilt with respect to the x-rays to gain some in-plane magnetic sensitivity, though the photo-emitted electrons are normally incident into the electron microscope. Image acquisition times were 2 to 3 minutes and image processing techniques were restricted to sub-pixel alignment, brightness and contrast adjustments, and median noise or Gaussian blur filters. When the clock field time rate of change $\frac{\partial H}{\partial t}$ is large (at pulse edges), effective magnetic contrast and

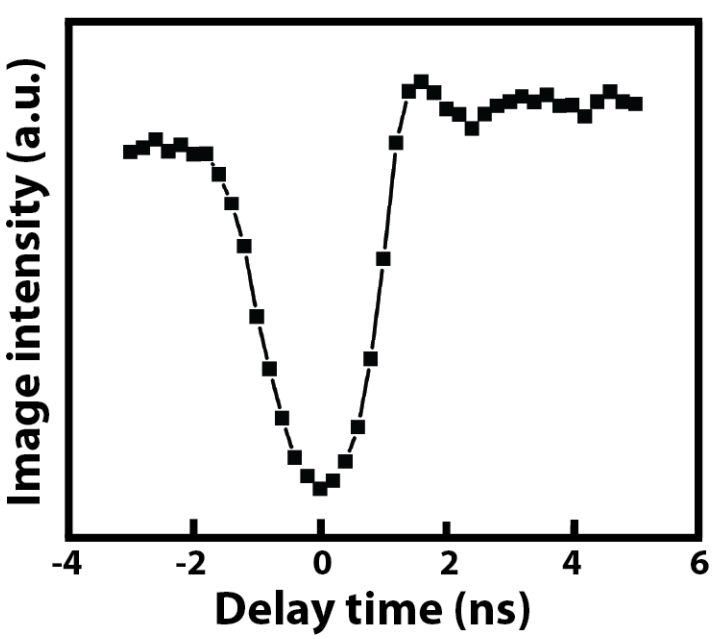

Figure 7. 7: Average raw image intensity versus time delay showing Oersted field pulse.

image resolution were reduced due to the image blurring during these time delays. However, images taken during the peak of the pulse were fairly useable because $\frac{\partial H}{\partial t}$ was small. Thus, we confirmed that clock fields were sufficient by observing the loss of magnetic contrast at the time delay of the pulse peak (though observing cascade-like signal propagation behavior is sufficient evidence as well). Figure 7.8 shows both raw and magnetic contrast images at the pulse peak (which we designated 0 time delay). While the chains were fairly clearly resolved (vertical line segments in the upper half of the raw image) with minimal amounts of added blur, they exhibited no magnetic contrast at all. Meanwhile, the permalloy numerical markers (features spaced horizontally through the center of the image) used for identifying chains retained their magnetic contrast. As this XMCD geometry was not sensitive to the vertical direction of magnetic moment, we took this to mean that the clock field had magnetized the chain along this axis.

We measured the time dynamics of 18 individual chains on one sample and found a clear display of cascade-like signal propagation in only one chain. Though too many errors obscured the process in other chains, observing it in one chain is enough to conclude that engineering for high-speed cascade-like behavior is certainly possible and that reliability and consistency are the major areas that need improvement. Figure 7.9 shows the signal propagation dynamics of this chain and includes our own interpretation of the results due to the low signal-to-noise ratio. Note that the biased input (black feature at the bottom of each frame) spontaneously switches first. Based on the frames 3 through 7 of the figure we

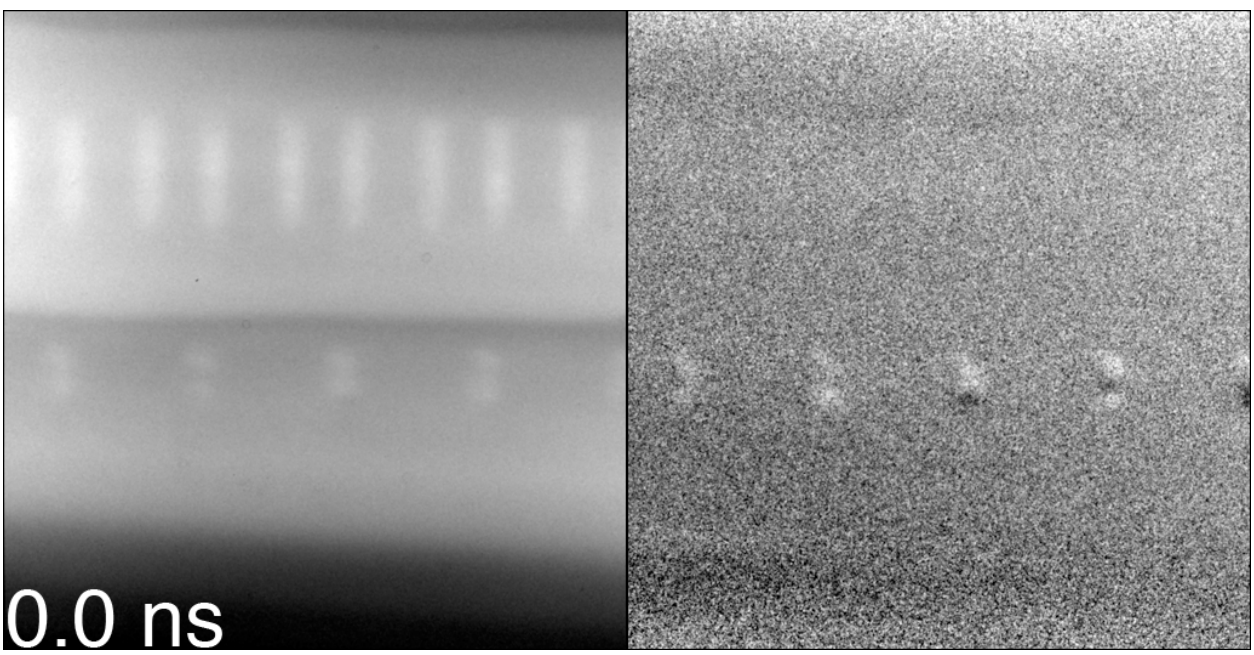

Figure 7. 8: Raw PEEM exposure (left) and reversed-helicity magnetic contrast image (right) taken during the peak of the pump pulse. Chains are white line segment features in the upper half of the raw image while numerical markers run along the center.

can extract an average switching speed of 100 ps per nanomagnet, which is consistent with the fastest speeds predicted[5,8,15]. Errors form in the 3rd and 7th frames of the out-of-order switching kind, which is undetectable in the static measurement techniques used in sections 6.4 and 6.5. Additionally, we note that each magnet appears to take several hundred ps to reach full magnetic contrast. We attribute this effect to jitter in the amount of time that any given magnet takes to switch. This randomness appears due to the effects of thermal fluctuations. In a static measurement, an average signal propagation distance of at least 11 would be reported here, but instead a cluster of at most 6 magnets exhibits proper signal propagation. This highlights the ability for time-resolved techniques to detect error nucleations in chains, although it does not obsolete static techniques, which can gather statistics per clock cycle.

Key to the interpretation of stroboscopic XMCD is the understanding that the images represent the cycle-to-cycle average of the time dynamics. If a magnetic element appears to have no particular magnetic contrast, then the possibilities are that either its magnetic moment is orthogonal to the axis of sensitivity or that it appears white for half of the cycles and black for the other half. In this situation, some assumptions are required to assist with interpretation. We expect that nanomagnets in their neutral state show the 4-domain pattern as in figure 6.6 rather than appear uniformly gray, but due to the poor resolution and signal-to-noise ratio we faced in two-bunch mode we do not see this pattern in our data. Instead, we make use of the expectation that the likelihood of any nanomagnet to switch out of its easy axis without the clock field is extremely low. Especially within the

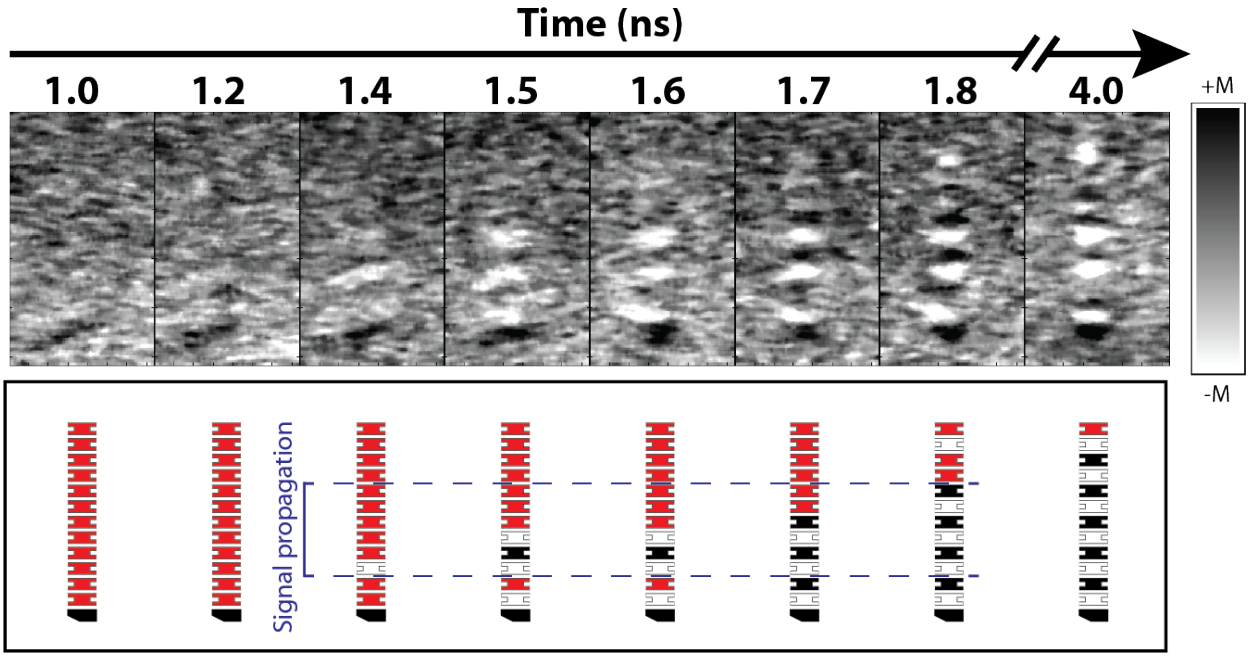

Figure 7. 9: Time-delay series of magnetic contrast PEEM images of a chain exhibiting cascade-like signal propagation behavior. Our interpretation (bottom) shows neutral state nanomagnets as red and highlights the cascade zone.

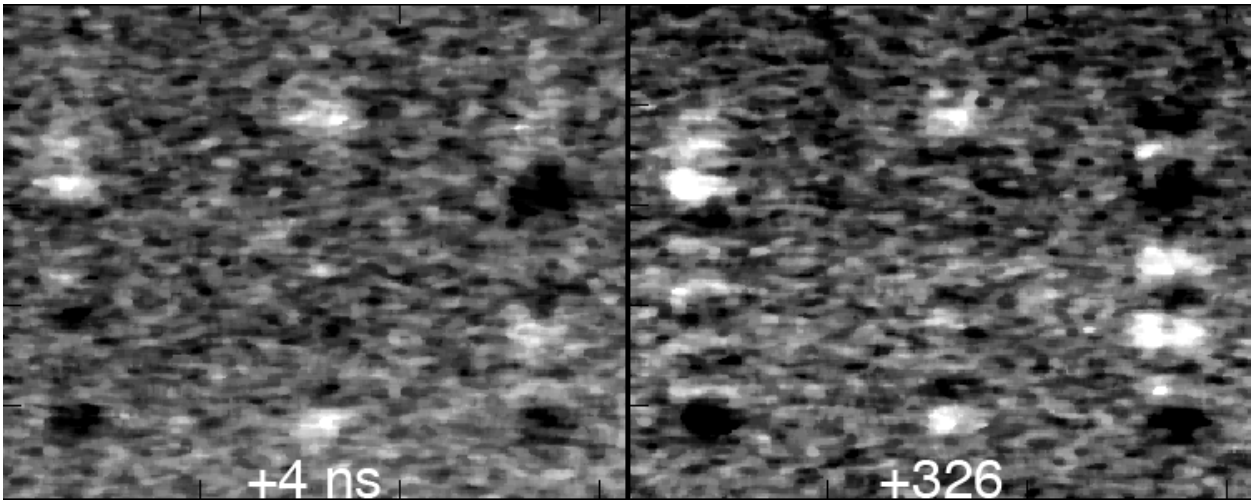

Figure 7. 10: Time-delay magnetic contrast PEEM images of 3 chains exhibiting thermally-assisted switching. Most of the repetition period lapses between the two images, which are taken 4 ns after (left) the pump pulse and 2 ns before (right) the pump pulse.

pump-probe repetition period (clock cycle period) of 328 ns, nanomagnets that are oriented along their easy axis are very stable. Therefore, if at any time a nanomagnet is observed to transition from gray to either white or black, we assume that at all times before that it is in its neutral state. If this observed transition occurs at far longer (1 ns or more while affected by an already-switched neighbor) delays than expected, as exemplified in figure 7.10, then we attribute it to thermally-assisted switching.

We experimentally demonstrate for the first time native-speed cascade-like signal propagation in chains of anisotropy-engineered nanomagnets at room temperature. Based on our theoretical and experimental progress on field-coupled NML, we make a suggestion for the direction of further engineering work on this architecture. We suggest that crystalline (material-dependent) anisotropy be used in place of configurational anisotropy. More specifically, a material with strong out-of-plane anisotropy due to interfacial effects combined with a crystalline cubic anisotropy with one easy axis that is out-of-plane would virtually eliminate defects arising from imperfect lateral patterning. This would also allow nanomagnets to be dot-shaped, which helps with lateral downscaling. Scaled-down nanomagnets benefit from increasing coupling strengths as well as the obvious increased device density. Thus, moving to such a material would quite significantly improve reliability and consistency in field-coupled NML.

Chapter 8. Spin-Transfer Torque and Energy-Efficient Switching

1. Spin-Transfer Torque Magnetic Random Access Memories

A very immediate (already in production) application of nanomagnetism is non-volatile memory. Though many architectures and devices (such as hard disks) exist, we will only introduce magneto-resistive random access memory (MRAM). MRAMs have the potential to replace many other existing memory architectures[62] once its densities and costs scale further. Flash memory and electrically erasable programmable read only memory both have very limited endurance, while MRAM has extraordinarily high endurance as well as faster performance. Dynamic random access memories are volatile, while MRAM is non-volatile (up to a time constant that can be engineered) and offers somewhat faster performance. MRAM may also be used as cache memory in solid-state disks and in the slower parts of the processor cache hierarchy (replacing static random access memories in high-level cache). Most notably, the non-volatility of MRAM presents a major power dissipation advantage over dynamic memories.

The basic storage element in MRAM is a magneto-resistive structure such as a spin valve or a magnetic tunnel junction (MTJ). Figure 8.1 shows the basic structure of the device. A thin layer of material is sandwiched between two ferromagnets[34]. For the spin valve, this material is a metal and the structure exhibits giant magneto-resistance. For the MTJ, this material is an insulator and the structure exhibits tunneling magneto-resistance. In either case, if the two ferromagnets have parallel magnetic moments the electrical resistance through the structure is lowest, and if they have antiparallel magnetic moments the resistance is highest. A simple explanation for this phenomenon is to split conduction through each magnet into parallel spin-up and spin-down channels. Due to the difference in density of states at the Fermi level between the two spin channels, one channel exhibits more scattering and thus less conductivity. Assuming that spin is conserved in the spacer material, the sandwich structure effectively becomes a series combination of two resistances for each spin channel. It is then straightforward to show that arranging the like

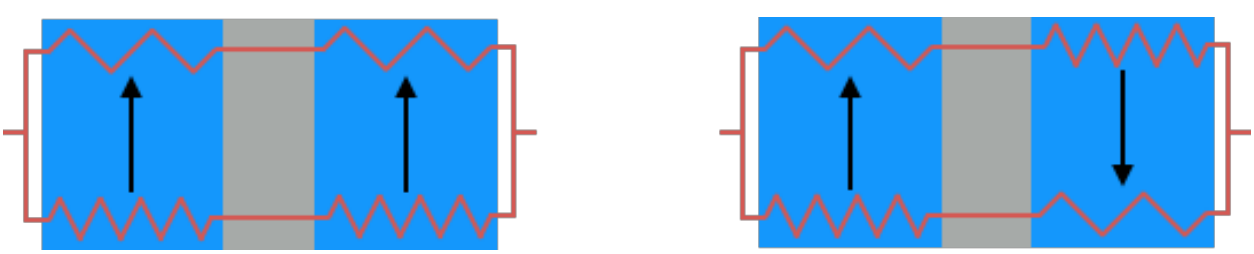

Figure 8. 1: Magneto-resistive junction in low resistance state (left) and high resistance state (right). Magnets (blue), their moments (arrows), and junction material (gray) shown.

resistances in series provides a lower total resistance. Therefore, in a typical device where each magnet has two stable states due to uniaxial anisotropy, one bit can be stored in the resistance state of the structure. Typically, one magnet (the fixed layer) is designed to have higher coercivity so that only the other magnet (free layer) switches.

Early MRAM cells used Oersted fields to switch the free layers. A more energy efficient method is to use spin transfer torque[62], which can be directly applied as electric current through the magneto-resistive junction. Memory devices employing such developments are called spin transfer torque (STT)-MRAMs. Both write and read operations can be achieved by applying current through the junction. A larger current switches the free layer to an orientation determined by the direction of current, and a smaller current leaves the free layer unperturbed while producing a detectable junction voltage. Equation 3.10 (the Landau-Lifshitz-Slonczewski equation) describes the free layer dynamics when subject to a current that passes through a nearby fixed layer. The adiabatic spin torque term is the 'torque-like' term and has the form of Gilbert damping. The non-adiabatic spin torque term is the 'field-like' term and has the form of Larmor precession. By recombining the terms with like forms so that the effective field in each term has an additional component, the dynamic behavior can be understood in a simpler and more familiar manner.

Figure 8.2 illustrates the 'cross-point' (the memory cells are at the crossing points of gridlines) architecture[34] for STT-MRAMs. Bit lines consisting of a 'true' line (BLT) and a 'complement' line (BLC) are binary inversions of each other and establish a voltage across all cells in a column. The polarity of voltage and current reverses if the bit lines switch. Word lines (WL) enable current to flow through each cell in a row. Switching on a word line performs a write or read operation on the entire row, where the bits recorded are determined by the bit line pattern at the time. Only one word line may be active at any given time to prevent overwriting other rows. Thus, operations in this architecture occur in row-sized blocks (as opposed to bit-wise addressing).

An additional improvement in energy efficiency results from using out-of-plane

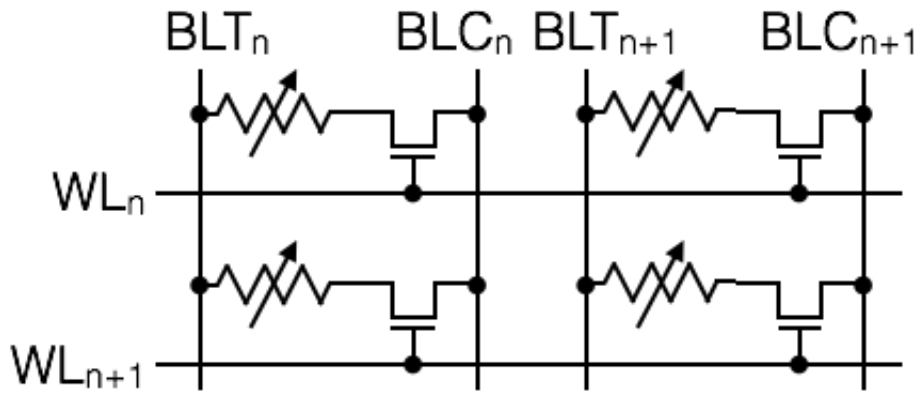

Figure 8. 2: Circuit diagram of 2x2 MRAM cell array.

(perpendicular) anisotropy magnets[34]. In most in-plane magnets, the large demagnetizing fields formed when the magnetization is out-of-plane present a large energy barrier. Due to the precessional motion of switching, the transient out-of-plane magnetization is significant and this energy barrier must be overcome. On the other hand, the lowest energy barrier separating the binary states usually occurs in-plane. Thermal fluctuations only need to overcome this barrier and thus STT switching sees a higher barrier than thermal switching. In typical out-of-plane magnets, the anisotropy is uniaxial (isotropic in-plane) since the shape is circular. The same in-plane energy barrier is encountered by both STT switching and thermal fluctuations, resulting in better efficiency. In addition, the circular shape allows for smaller magnets to be fabricated, which further increases efficiency. Besides using out-of-plane fixed and free layers, perpendicular STT-MRAM otherwise uses the same cell and array structures as shown in figure 8.2.

2. The Spin Hall Effect in Metals

A newer development with the potential for even more efficient switching than STT is the spin Hall effect (SHE) in metals[63]. The SHE originates from spin-orbit coupling and can qualitatively be described as the coupling of charge currents and spin currents in a bulk material. The spin currents lead to an accumulation of spins at the boundary of the material[64]. Figure 8.3 shows a cartoon of the geometry with respect to the cross section of a wire. The direction (sign) of the spin accumulation may be as shown, or opposite depending on the material. If the handedness is as shown, the material has a positive spin Hall conductivity, while the handedness that follows the Oersted field corresponds to a negative spin Hall conductivity. A wide variety of materials have so far been found to exhibit measurable SHE. The metals include platinum[65], beta tantalum[63], beta tungsten[66], palladium[67], gold[68], and copper with bismuth[69], iridium[70], or lead[71] impurities. In addition, measurable SHE has also been found in gallium arsenide[72], bismuth selenide[73] (Bi_2Se_3, a topological insulator), and graphene with metallic adatoms[74].

Several formalisms exist to describe SHE. There are fully quantum mechanical

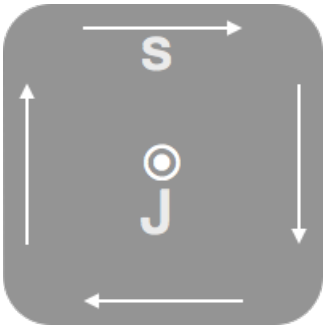

Figure 8. 3: Wire cross section showing charge current (J) and spin accumulation (s).

treatments relating it to the Berry phase[75,76]. A more classical treatment using Boltzmann transport is commonly used[77-79]. Under certain limits, this treatment reduces to an approximation known as 'drift-diffusion', which provides the most intuitive understanding of the physics. To that end, we present here the 'drift-diffusion' approximation[77]. This formalism uses the concept of separate chemical potentials (with units of Volts) for charge (μ_c) and spin ($\vec{\mu}_s$) defined in the following way for net charge density ρ and net spin density $\vec{s}$ (whose direction points along the net spin orientation):

$$\rho(\vec{r},t) = n_c \mu_c(\vec{r},t) \tag{8.1}$$

$$\vec{s}(\vec{r},t) = n_s \vec{\mu}_s(\vec{r},t) \tag{8.2}$$

Here, n_c (with units of charge per volume per Volt) and n_s (with units of action per volume per Volt) are related to the density of states and the explicit space and time dependences are given. These dependencies will be implicit in further references to these parameters. In the context of a metal, the drift-diffusion equations comprise a pair of continuity equations for charge and spin and a pair of coupled equations for charge current $\vec{J}$ and spin current $\bar{\bar{Q}}$, where the first index in Q is the direction of flow and the second index in Q is the direction of spin orientation. When the tensor equations are given in Einstein notation, we have:

$$-\frac{\partial \rho}{\partial t} = \vec{\nabla} \cdot \vec{J} \tag{8.3}$$

$$-\frac{\partial s_j}{\partial t} = \nabla_i Q_{ij} + \frac{s_j}{\tau} \tag{8.4}$$

$$\vec{J} = \sigma_c \vec{\nabla} \mu_c - \sigma_s \vec{\nabla} \times \vec{\mu}_s \tag{8.5}$$

$$Q_{ij} = \frac{-\hbar}{2e} \left(\sigma_c \nabla_i \mu_{sj} + \sigma_s \epsilon_{ijk} \nabla_k \mu_c \right) \tag{8.6}$$

ε_{ijk} is the Levi-Civita symbol, σ_c and σ_s are respectively the electrical and spin Hall conductivities, and τ is a characteristic spin relaxation (spin-flip scattering) time.

Some interesting observations can be made about the form of the equations. Equation 8.6 states that charge chemical potential can generate spin current (SHE). Equation 8.5 states that spin chemical potential can generate charge current (inverse SHE). Equation 8.4 provides a sink term that destroys spin polarization if no spin current is flowing. Importantly, if there is charge current (charge chemical potential gradient) in the metal and no spin chemical potential gradient, then equation 8.6 shows that spin current is created if the spin Hall conductivity is non-zero. Additionally, the generated spin flow, spin

orientation, and charge chemical potential gradient directions are all mutually orthogonal. This leads to the geometry shown in figure 8.3.

We make some assumptions in order to solve for a steady-state spin density distribution in a typical SHE metal wire. Setting all time derivatives to zero, we have:

$$\nabla^2 \mu_c = 0 \tag{8.7}$$

$$\frac{n_s \mu_{sj}}{\tau} = -\nabla_i Q_{ij} \tag{8.8}$$

In addition, we neglect the inverse SHE term in equation 8.5 since it is typically the smallest term ($\sigma_c > \sigma_s$ and $J > \frac{2eQ}{\hbar}$) and it causes J to be non-uniform across the cross-section. Coupling is thus lost from this equation:

$$\vec{J} = \sigma_c \vec{\nabla} \mu_c \tag{8.9}$$

We solve equations 8.6 through 8.9 by assuming the charge and spin currents take the form appropriate to the geometry in figure 8.3:

$$\vec{J} = \begin{pmatrix} 0 \\ 0 \\ J_z \end{pmatrix} \tag{8.10}$$

$$\overline{\overline{Q}} = \begin{pmatrix} 0 & Q_{xy} & 0 \\ Q_{yx} & 0 & 0 \\ 0 & 0 & 0 \end{pmatrix} \tag{8.11}$$

Due to symmetry, the net spin density at the center of the wire is zero. In addition, at the surface no spin current can flow in the direction of the surface normal. Thus the following Dirichlet boundary conditions are imposed:

$$\vec{\mu}_s(x = 0, y = 0) = 0 \tag{8.12}$$

$$Q_{xy}(x = \pm L_x) = 0 \tag{8.13}$$

$$Q_{yx}(y = \pm L_y) = 0 \tag{8.14}$$

The solutions for the charge and spin chemical potentials up to any integration constants are:

$$\mu_c = \frac{J_z z}{\sigma_c} \tag{8.15}$$

$$\vec{\mu}_s = \begin{pmatrix} +\sigma_s J_z \frac{D}{\sigma_c^2} \frac{\sinh\left(\frac{y}{D}\right)}{\cosh\left(\frac{L_y}{D}\right)} \\ -\sigma_s J_z \frac{D}{\sigma_c^2} \frac{\sinh\left(\frac{x}{D}\right)}{\cosh\left(\frac{L_x}{D}\right)} \\ 0 \end{pmatrix} \tag{8.16}$$

$$D = \sqrt{\frac{\tau \hbar \sigma_c}{2 e n_s}} \tag{8.17}$$

There are some noteworthy properties of equation 8.16. First, the maximum spin density occurs at the surfaces. Second, the spin density scales linearly with current density. Third, the spin density flips direction if the spin Hall conductivity changes sign. Our solution is also consistent in form with published one-dimensional calculations[78,79].

Figure 8.4 shows a three-terminal memory device combining an MTJ with SHE that was proposed[63]. The free layer feels a torque due to the spin accumulation at the interface, and the equation of motion for the free layer becomes[77]:

$$\begin{aligned} \frac{\partial \vec{M}}{\partial t} &= -\gamma \vec{M} \times \vec{H}_{eff} + \frac{\alpha}{M_S} \vec{M} \times \frac{\partial \vec{M}}{\partial t} \\ &+ \frac{\gamma}{\mu_0 \tau_e M_S} \vec{M} \times \vec{s} + \frac{\gamma}{\mu_0 \tau_d M_S^2} \vec{M} \times \left(\vec{M} \times \vec{s}\right) \end{aligned} \tag{8.18}$$

Here, τ_e is related to the precession period about the exchange field and τ_d is a characteristic spin dephasing time. Note that equation 8.18 also has a 'field-like' and a 'torque-like' term added onto the Landau-Lifshitz equation. In this device, power efficiency can be improved by scaling down the thickness of the SHE metal to a limit of 2D since the surface spin accumulation magnitude varies as $\tanh\left(\frac{L}{D}\right)$ to reduce total current. In addition, lateral dimensions of the device can continue to be scaled to the same effect. The benefit gained by having three terminals is the spatial separation of write and read

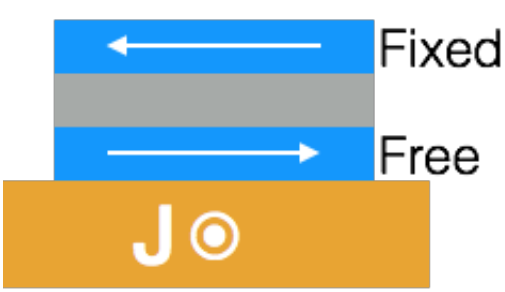

Figure 8. 4: 3-terminal SHE and MTJ combination device.

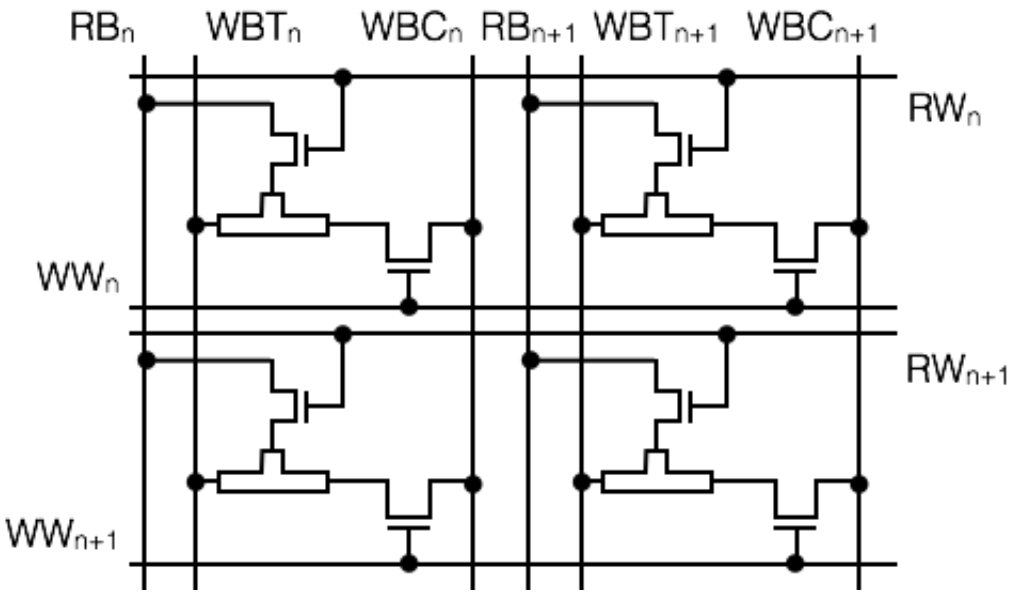

Figure 8. 5: Circuit diagram of 2x2 MRAM cell array using 3-terminal devices.

currents[63]. Large write currents no longer pass through the MTJ, which largely determines device endurance through dielectric breakdown. Therefore, this particular device offers both improved efficiency and reliability. However, we point out that only the in-plane geometry can be used if the torque is applied throughout the free layer relaxation dynamics (since the magnetization damps toward the desired direction, precise control of torque pulse width as required by precessional schemes[80] is not needed). Out-of-plane free and fixed layers would have an unbroken symmetry that prevents reliable switching[81]. Presumably, a cell array architecture that preserves row-wise write and read operations would look like figure 8.5. The original signal lines are now used for writing only, with WW denoting write word lines and WB denoting write bit lines. Similarly, the signal lines for reading are RW for words and RB for bits. Though an extra transistor is required per cell for MTJ resistance sensing, this transistor need not be as large as the write isolation transistor since read currents are small.

SHE also has applications in NML as a direct and energy-efficient replacement for Oersted field clocking structures. Though NML may intrinsically have low energy dissipation, the same has so far not been true of NML clocking mechanisms. Investigations of using SHE[81] as well as other mechanisms[62] for this purpose are already underway. Demonstrating low energy consumption on a larger scale that includes clocking would be a major development for NML.

3. Two-Bit Free Layers using Configurational Anisotropy

We devise a method to store two bits per cell by using the concave square shapes studied in section 4.5. Since the shapes have four-fold symmetry, they have four stable

magnetization states (as is the case for biaxial anisotropy). Readout would still be accomplished using an MTJ, but the orientation of the fixed layer must not align with the anisotropy axes (neither easy nor hard) of the free layer. Otherwise, due to symmetry two of the states would produce the same magneto-resistance since the projection of the free layer magnetization onto the fixed layer magnetization would be the same. To a very good approximation[82], the electrical conductance of the MTJ depends linearly on $\vec{M}_{free} \cdot \vec{M}_{fixed}$. Therefore, we can optimize the conductance digitization of the four states by equalizing the conductance separations between states. For an angle θ between the fixed layer easy axis and either free layer easy axis, we have:

$$\cos(\theta) - \sin(\theta) = 2\sin(\theta) = -\sin(\theta) + \cos(\theta) \tag{8.19}$$

The solution to equation 8.19 is $\theta = cos^{-1}\left(\frac{3}{\sqrt{10}}\right)$. Figure 8.6 shows a diagram of the relative layer alignments and a cartoon of the corresponding conductance levels. For the free layer, one easy axis contains the two central levels while the other easy axis contains the two extremes.

Using configurational anisotropy, we can tune the energy barrier heights, which for this case is equal to $\frac{K_b V}{4}$ (the trivial case of setting K_u to 0 in equation 3.23 or 3.24). Presumably, if $E_B = 60k_BT$ is required for a uniaxial nanomagnet, then by a combination of material anisotropy and configurational anisotropy we can also achieve $60k_BT$ for a biaxial nanomagnet of comparable dimensions. However, more complex treatments[83] of the thermal behavior of nanomagnets are worth considering, especially when concerning more

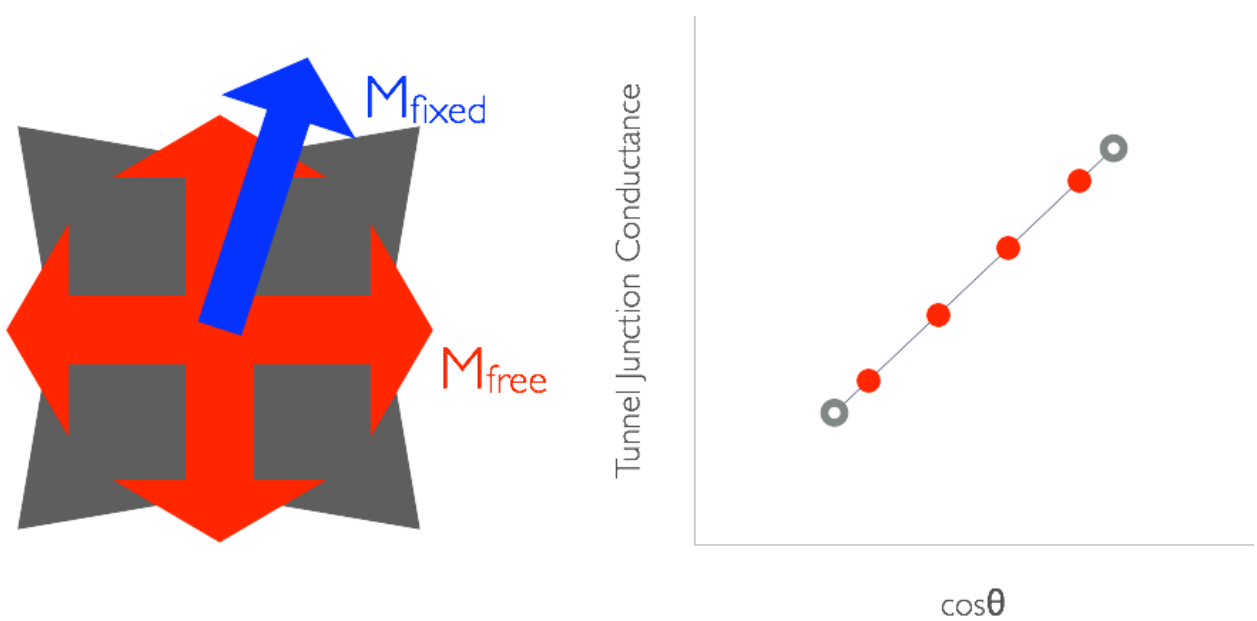

Figure 8. 6: Diagram (left) of the free layer easy axes (red) and fixed layer easy axis (blue) corresponding to the 4 distinct and equally spaced MTJ conductance levels (right).

complex anisotropies. If the data retention time of a magnetic particle depends on the energy barrier heights, then a biaxial magnet that is as stable as a uniaxial magnet must have $K_b = 4K_u$. Since an applied magnetic field equal to the anisotropy field is required to switch the magnet, nothing else considered it would take four times the field to switch the biaxial magnet. In practice, since in-plane free layers are typically limited by their out-of-plane energy barrier this becomes less of an issue. Alternatively, thermal fluctuations may be treated as a stochastic field as in section 3.3. If the data retention time of a magnetic particle depends on the anisotropy field strengths, then a biaxial magnet that is as stable as a uniaxial magnet only needs $K_b = K_u$. In this case, the field required to switch suffers no additional penalty. Since a single switching operation writes two bits (as opposed to a write operation per bit), our design may therefore be up to twice as energy-efficient as a one-bit MRAM.

Figure 8.7 shows the design of a two-bit cell as an extension of the design in figure 8.4. SHE drives switching, but the current can be applied along any easy axis of the free layer by using a cross structure. The applied current pulses would have long enough duration to last through the free layer relaxation, and thus precise control of the pulse width is not needed. In order to sufficiently control the direction of current in the cross area, only one wire (bit line) out of the two in the cross should be conducting at any time, while both contacts in the other wire should be high-impedance. In addition, a write isolation transistor (word line) is needed for each wire in order to set the otherwise conducting wire to high-impedance (which disables write operations, since three SHE contacts out of the four in the cross become high-impedance). A smaller read isolation

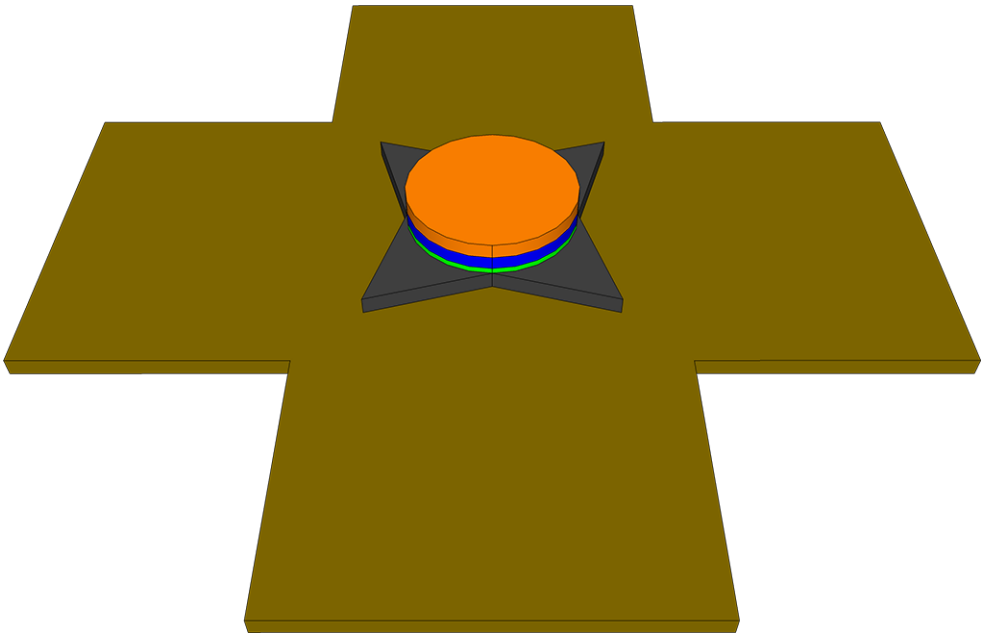

Figure 8. 7: 2-bit MRAM cell using SHE and an MTJ. Shown here are the SHE metal (brown), free layer (gray), spacer layer (green), fixed layer (blue), and top MTJ contact (orange).

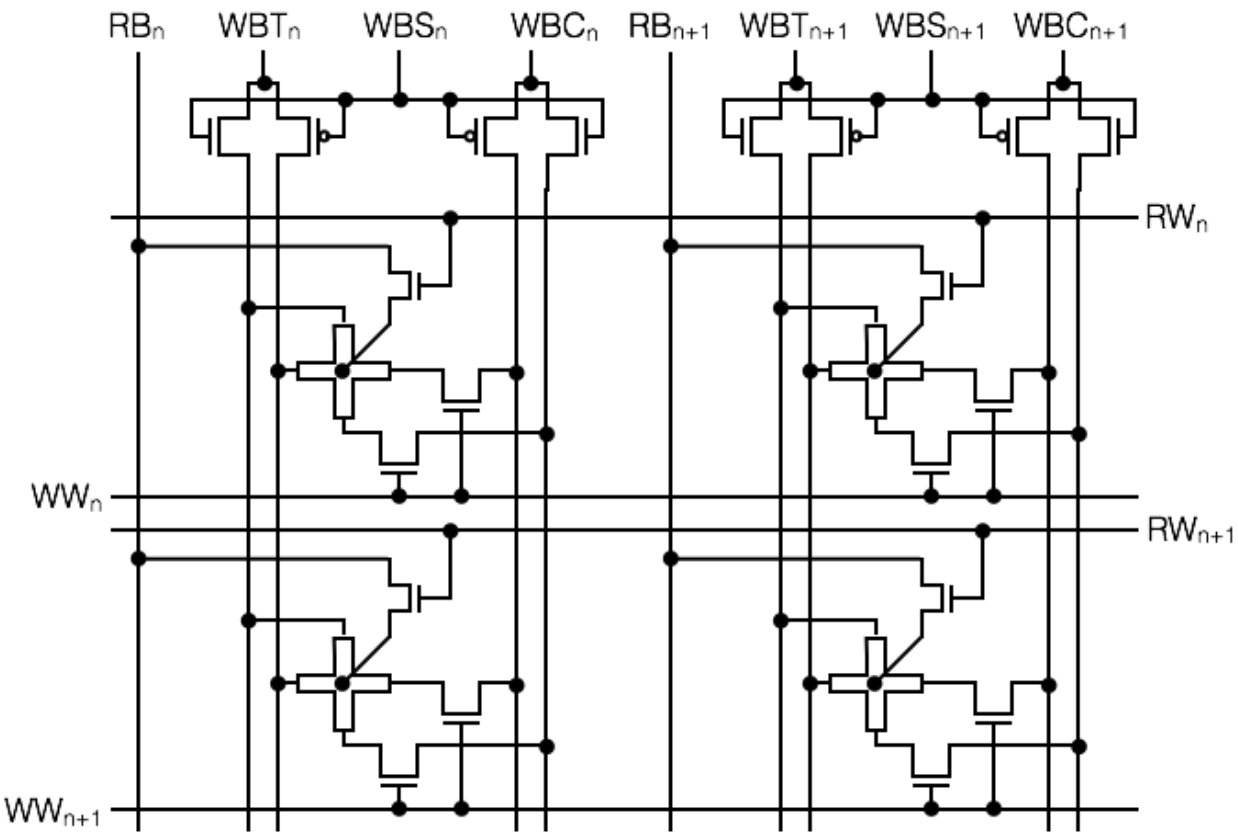

Figure 8. 8: Circuit diagram of 2x2 MRAM cell array using 5-terminal 2-bit devices.

transistor as implemented in the three-terminal device in section 8.2 would also be needed at the fifth (top) contact to prevent large currents from passing through the MTJ. Compared to the three-terminal device, our five-terminal device in total requires one fewer MTJ and one fewer read isolation transistor per two bits, the same number of write isolation transistors, and one additional large transistor per bit line (where each cell in the usual 'cross-point' is considered to have two bit lines). Figure 8.8 gives our proposed cell array architecture. In addition to the signal lines of the three-terminal device, we have an additional bit select line (WBS) per set of four bit lines that chooses which pair of bit lines are high-impedance. In the usual 'cross-point', each independent bit line signal controls two bit lines (a true and a complement). In our case, four bit lines are controlled by a single independent bit line signal.

Due to gains of up to a factor of two for bit-wise write energy efficiency and bit-wise read isolation transistor count, we believe that this five-terminal MRAM device warrants experimental investigation.

Chapter 9. Dynamic Experimental Methods for Investigating the Spin Hall Effect

1. Optical Second Harmonic Generation

Complementary to MOKE, optical second harmonic generation (SHG) is a non-linear optical probe that can also measure magnetism and exhibits a different set of properties. Most notably, SHG is inherently sensitive to surfaces and interfaces[84], leading to the ability to probe buried interfaces[85] as well as antiferromagnetic ordering[86]. In this section we introduce the theory of SHG and how it can measure magnetization at surfaces and interfaces. This particular phenomenon is known as magnetization-induced second harmonic generation (MSHG).

We can relate the radiated second harmonic to the fundamental by starting with the following Maxwell's equations and constitutive relations:

$$\vec{\nabla} \times \vec{E} = -\frac{\partial \vec{B}}{\partial t} \tag{9.1}$$

$$\vec{\nabla} \times \vec{H} = \vec{J} + \frac{\partial \vec{D}}{\partial t} \tag{9.2}$$

$$\vec{B} = \mu_0(\vec{H} + \vec{M}) \tag{9.3}$$

$$\vec{D} = \epsilon_0 \vec{E} + \vec{P} \tag{9.4}$$

Putting the above equations together produces the well-known wave equation for the electric field, where the source term that is typically written simply in terms of the total current is rewritten as the sum of free current and two bound currents:

$$\vec{\nabla} \times \vec{\nabla} \times \vec{E} + \epsilon_0 \mu_0 \frac{\partial^2 \vec{E}}{\partial t^2} = -\mu_0 \left(\frac{\partial^2 \vec{P}}{\partial t^2} + \frac{\partial \vec{J}}{\partial t} + \vec{\nabla} \times \frac{\partial \vec{M}}{\partial t} \right) \tag{9.5}$$

We take the approximation that the dominant source comes from the polarization:

$$\vec{\nabla} \times \vec{\nabla} \times \vec{E} + \epsilon_0 \mu_0 \frac{\partial^2 \vec{E}}{\partial t^2} \approx -\mu_0 \frac{\partial^2 \vec{P}}{\partial t^2} \tag{9.6}$$

We take the time-harmonic form of the polarization up to second order in the power series expansion with respect to the incident monochromatic electric field:

$$\mathcal{F}\vec{P}(t) = \vec{P}(\omega) \approx \vec{P}^{(1)}(\omega_0) + \vec{P}^{(2)}(2\omega_0) \approx \epsilon_0 \left[\chi^{(1)}(\omega_0)\vec{E}(\omega_0) + \chi^{(2)}(2\omega_0) : \vec{E}(\omega_0)\vec{E}(\omega_0)\right] \tag{9.7}$$

The susceptibility factors are thus proportional to the expansion coefficients. The second-order susceptibility term is multiplied by a tensor scalar product onto the dyadic product of two vectors. This amounts to a third-rank tensor multiplying a second-rank tensor (dyad) to produce a first-rank tensor (vector). In Einstein notation, this term is written:

$$P_i^{(2)} = \epsilon_0 \chi_{ijk}^{(2)} E_j E_k \tag{9.8}$$

The symmetry property that leads to SHG's interface sensitivity is inversion symmetry. Applying spatial inversion to all vectors, we have:

$$\begin{aligned} \vec{P} &= \epsilon_0[\chi^{(1)}\vec{E} + \chi^{(2)} : \vec{E}\vec{E}] \\ -\vec{P} &= \epsilon_0[-\chi^{(1)}\vec{E} + \chi^{(2)} : \vec{E}\vec{E}] \end{aligned} \tag{9.9}$$

If both equations are to be satisfied, $\chi^{(2)}$ necessarily vanishes. Therefore, in the bulk of a centrosymmetric medium, no SHG occurs (at least up to the approximation presented). At surfaces and interfaces, full inversion symmetry is broken and thus SHG is allowed. Another symmetry is in the ordering of incident electric field vectors. Since the incident light is monochromatic, we can switch the polarizations of the two field vectors without affecting the total field. Therefore, the rank-3 tensor $\chi^{(2)}$ only has 18 independent elements since it is restricted by:

$$\chi_{ijk}^{(2)} = \chi_{ikj}^{(2)} \tag{9.10}$$

As a result of the above restriction, we can also write the rank-3 tensor in a more compact rank-2 (matrix) form known as Voigt notation:

$$\begin{pmatrix} P_x \\ P_y \\ P_z \end{pmatrix} = \begin{pmatrix} \chi_{xxx} & \chi_{xyy} & \chi_{xzz} & \chi_{xyz} & \chi_{xxz} & \chi_{xxy} \\ \chi_{yxx} & \chi_{yyy} & \chi_{yzz} & \chi_{yyz} & \chi_{yxz} & \chi_{yxy} \\ \chi_{zxx} & \chi_{zyy} & \chi_{zzz} & \chi_{zyz} & \chi_{zxz} & \chi_{zxy} \end{pmatrix} \begin{pmatrix} E_x E_x \\ E_y E_y \\ E_z E_z \\ 2E_y E_z \\ 2E_x E_z \\ 2E_x E_y \end{pmatrix} \tag{9.11}$$

Additional restrictions in the number of independent elements of $\chi^{(2)}$ can be deduced by symmetry properties relating to specific materials. We can apply symmetry transformations to rank-3 tensors using the following operation[87]:

$$\overline{\overline{T}}\chi_{ijk} = \sum_{i'j'k'} T_{ii'}T_{jj'}T_{kk'}\chi_{i'j'k'} \tag{9.12}$$

We consider an amorphous material, as it is the most relevant to our work. The bulk is of symmetry group K_h and the surface is of symmetry group $C_{\infty,v}$. We choose to let the x-y plane lie on the surface, and thus the z axis includes the surface normal. The surface is invariant under rotation by any angle about the surface normal and also under reflection through any plane that includes the surface normal. The rotation symmetry operation about the surface normal is:

$$\overline{\overline{T}}(\theta) = \begin{pmatrix} \cos\theta & \sin\theta & 0 \\ -\sin\theta & \cos\theta & 0 \\ 0 & 0 & 1 \end{pmatrix} \tag{9.13}$$

The constraints set by the mirror symmetries are a subset of those set by the rotation symmetry. We require the following rotational invariance:

$$\overline{\overline{T}}(\theta)\chi^{(2)}(0) = \chi^{(2)}(0) \tag{9.14}$$

Here, $\chi^{(2)}(0)$ means the case of no magnetization. The resulting constraints are:

$$\chi^{(2)}(0) = \begin{pmatrix} 0 & 0 & 0 & 0 & \chi_{wz} & 0 \\ 0 & 0 & 0 & \chi_{wz} & 0 & 0 \\ \chi_{zw} & \chi_{zw} & \chi_{zzz} & 0 & 0 & 0 \end{pmatrix} \tag{9.15}$$

The index w represents both xx and yy and signifies that these two components are equal. There are thus only 3 independent elements.

We now add the magnetization of the material into consideration. We write the susceptibility to first order (we will find the first order term to be non-zero and so will not consider higher order terms) in the power series expansion with respect to magnetization:

$$\chi^{(2)}(\vec{M}) \approx \chi^{(2)}(0) + [\vec{\nabla}_{\vec{M}}\chi^{(2)}(\vec{M})]\vec{M} \tag{9.16}$$

For clarity and compactness, we present several other ways to express the last term:

$$[\vec{\nabla}_{\vec{M}}\chi^{(2)}(\vec{M})]\vec{M} = \chi^{(2,dM)}_{ijk\ell}M_\ell = \chi^{(2,M)}(\vec{M}) \tag{9.17}$$

While polarization and electric field are polar vectors, magnetization is an axial vector, which gains an additional sign flip under improper rotations such as reflections. Therefore, applying spatial inversion to all vectors again, we find that SHG is also forbidden in the bulk of a magnetic centrosymmetric medium:

$$\begin{aligned}\vec{P} &= \epsilon_0[\chi^{(1)}\vec{E} + (\chi^{(2,0)} + \chi^{(2,dM)}\vec{M}) : \vec{E}\vec{E}] \\ -\vec{P} &= \epsilon_0[-\chi^{(1)}\vec{E} + (\chi^{(2,0)} + \chi^{(2,dM)}\vec{M}) : \vec{E}\vec{E}]\end{aligned} \tag{9.18}$$

At the surface, the magnetization reduces the symmetry so that only mirror operations remain:

$$\overline{\overline{T}}(x \mapsto -x) = \begin{pmatrix} -1 & 0 & 0 \\ 0 & 1 & 0 \\ 0 & 0 & 1 \end{pmatrix} \tag{9.19}$$

$$\overline{\overline{T}}(y \mapsto -y) = \begin{pmatrix} 1 & 0 & 0 \\ 0 & -1 & 0 \\ 0 & 0 & 1 \end{pmatrix} \tag{9.20}$$

The corresponding actions on the components of magnetization are:

$$\begin{aligned} x \mapsto -x &\Rightarrow \{M_y \mapsto -M_y, M_z \mapsto -M_z\} \\ \chi^{(2,M)}(M_x) &= \overline{\overline{T}}(x \mapsto -x)[\chi^{(2,M)}(M_x)] \\ -\chi^{(2,M)}(M_y) &= \overline{\overline{T}}(x \mapsto -x)[\chi^{(2,M)}(M_y)] \\ -\chi^{(2,M)}(M_z) &= \overline{\overline{T}}(x \mapsto -x)[\chi^{(2,M)}(M_z)] \end{aligned} \tag{9.21}$$

$$\begin{aligned} y \mapsto -y &\Rightarrow \{M_x \mapsto -M_x, M_z \mapsto -M_z\} \\ -\chi^{(2,M)}(M_x) &= \overline{\overline{T}}(y \mapsto -y)[\chi^{(2,M)}(M_x)] \\ \chi^{(2,M)}(M_y) &= \overline{\overline{T}}(y \mapsto -y)[\chi^{(2,M)}(M_y)] \\ -\chi^{(2,M)}(M_z) &= \overline{\overline{T}}(y \mapsto -y)[\chi^{(2,M)}(M_z)] \end{aligned} \tag{9.22}$$

These restrictions produce a $\chi^{(2,M)}(M)$ of the following form:

$$\chi^{(2,M)}(\vec{M}) = \begin{pmatrix} \chi_{xxx}M_y & \chi_{xyy}M_y & \chi_{xzz}M_y & \chi_{xyz}M_z & 0 & \chi_{xxy}M_x \\ \chi_{yxx}M_x & \chi_{yyy}M_x & \chi_{yzz}M_x & 0 & \chi_{yxz}M_z & \chi_{yxy}M_y \\ 0 & 0 & 0 & \chi_{zyz}M_x & \chi_{zxz}M_y & \chi_{zxy}M_z \end{pmatrix} \tag{9.23}$$

The full susceptibility tensor (the sum of equations 9.23 and 9.15) is therefore:

$$\chi^{(2)}(\vec{M}) =$$
$$\begin{pmatrix} \chi_{xxx}M_y & \chi_{xyy}M_y & \chi_{xzz}M_y & \chi_{xyz}M_z & \chi_{wz} & \chi_{xxy}M_x \\ \chi_{yxx}M_x & \chi_{yyy}M_x & \chi_{yzz}M_x & \chi_{wz} & \chi_{yxz}M_z & \chi_{yxy}M_y \\ \chi_{zw} & \chi_{zw} & \chi_{zzz} & \chi_{zyz}M_x & \chi_{zxz}M_y & \chi_{zxy}M_z \end{pmatrix} \tag{9.24}$$

If we consider additional expansion terms for the second-harmonic polarization, we find that a quadrupole-like term[87] can exist in the bulk of a centrosymmetric medium:

$$\vec{P}^{(2)}(2\omega) = \epsilon_0[\chi^{(2,D)}(2\omega) : \vec{E}(\omega)\vec{E}(\omega) + \chi^{(2,Q)}(2\omega) : \vec{E}(\omega)\vec{\nabla}\vec{E}(\omega)] \tag{9.25}$$

In metals, screening effects usually allow the dipole-like term to be significantly larger[88]. However, this is not a general rule and significant bulk SHG contributions can exist even in metals.

The susceptibility tensor elements may be calculated[89] from microscopic theory, but doing so requires a great deal of knowledge about the wavefunctions in the material. However, useful information can still be obtained without knowing the tensor elements. If we choose an experiment geometry that is selective to particular polarizations of incident and radiated light, equation 9.24 shows that we can selectively be sensitive to particular components of magnetization. In addition, equation 9.16 shows that the tensor has components that are even or odd in magnetization. Since the optical intensity I is proportional to the square of the electric field, we have:

$$I_{\pm} \propto |\vec{E}_{even} \pm \vec{E}_{odd}|^2 \tag{9.26}$$

The ± denote the cases for opposite magnetizations. Considering that in general $\chi^{(2)}$ is complex and that there is some phase difference θ between the even and odd components, this expression expands to:

$$I_{\pm} \propto |\vec{E}_{even}|^2 + |\vec{E}_{odd}|^2 \pm 2|\vec{E}_{even}||\vec{E}_{odd}|\cos(\theta) \tag{9.27}$$

As long as the odd component is much smaller than the even component (a common case), we can arrange the opposing pair $I_{\pm}$ to get a quantity that is linear in magnetization:

$$|\vec{E}_{odd}| \ll |\vec{E}_{even}| \Rightarrow A = \frac{I_+ - I_-}{I_+ + I_-} \approx 2\frac{|\vec{E}_{odd}|}{|\vec{E}_{even}|}\cos(\theta) \approx 2\frac{|\chi^{(2,dM)}_{odd}|}{|\chi^{(2)}_{even}|}M\cos(\theta) \tag{9.28}$$

On the other hand, if it is possible to completely demagnetize and measure the intensity for zero magnetization I_0, which removes the odd component, then we may also use:

$$A = \frac{I_+ - I_-}{2I_0} = 2\frac{|\vec{E}_{odd}|}{|\vec{E}_{even}|}\cos(\theta) = 2\frac{|\chi_{odd}^{(2,dM)}|}{|\chi_{even}^{(2)}|}M\cos(\theta) \tag{9.29}$$

Various experimental methods have been used to probe the spin Hall effect in metals. These include anomalous Hall effect[81], spin torque ferromagnetic resonance[65], tunneling spectroscopy[90], and MOKE[91]. Out of these, only MOKE allows a bare metal film to be probed for spin accumulation. Based on the results of related experiments[92], we add SHG into this category of bare metal SHE probes. Advantages over pure MOKE include much larger magnetic sensitivity[84] and geometries sensitive only to in-plane magnetization[93] (which can be measured simultaneously alongside MOKE).

2. Time-Resolved SHG Experimental Setup

Figure 9.1 shows our experimental setup for performing time-resolved optical SHG. The desired sample geometry is a $\frac{\pi}{4}$ angle of incidence and p-polarized (x-z) incident and radiated light. By inspecting equation 9.24, we see that this geometry is sensitive to the transverse (y) direction of magnetization. We used a Coherent Mantis oscillator and Coherent RegA amplifier with external stretcher and compressor. We configured this

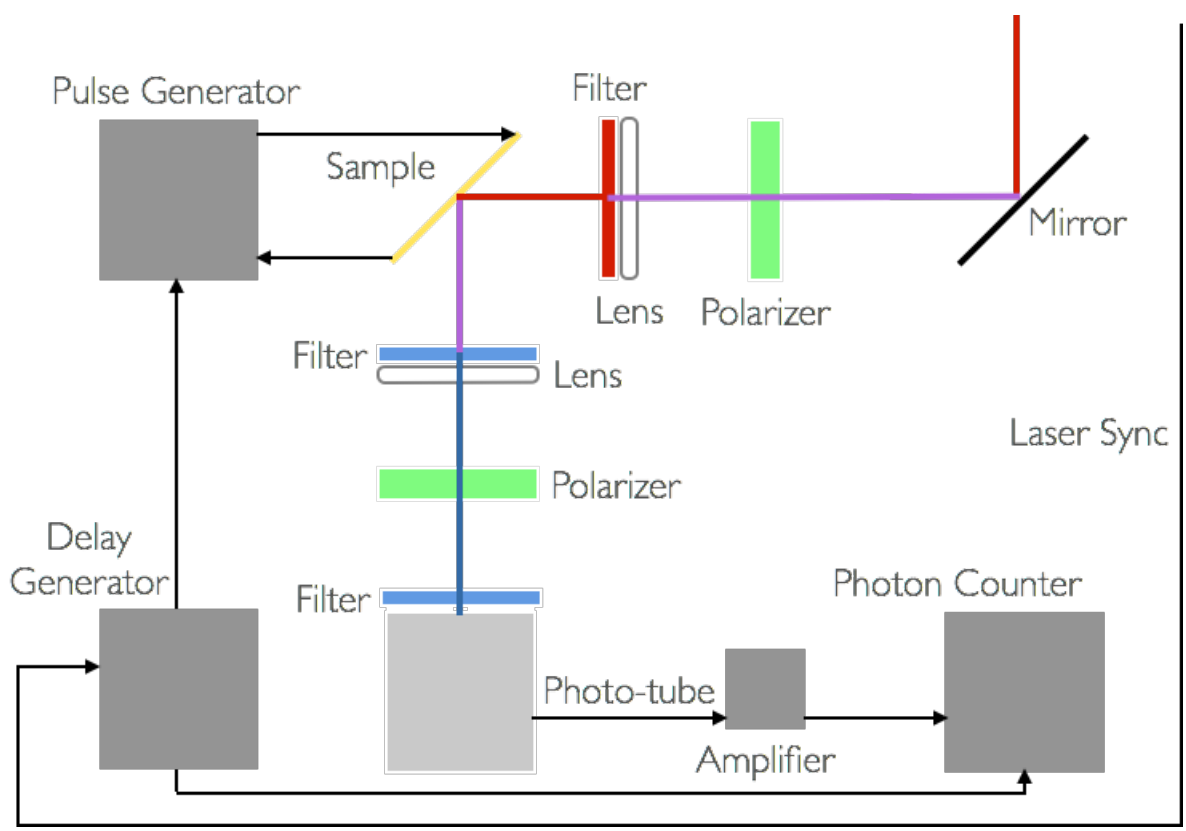

Figure 9. 1: Time-resolved optical SHG experimental schematic.

combination to produce an 800 nm wavelength laser beam with 100 fs pulse width and 250 KHz repetition rate. The setup in the figure is a stroboscopic experiment with electrical pump and optical probe pulses. The laser incident into the setup in the figure has an energy of approximately 17.7 nJ per pulse.

The laser beam first reflects off of a mirror that allows for fine adjustment of the angle of incidence. The first polarizer along the path is a Glan-laser polarizer, which is set to p-polarization. The first lens (5 cm singlet) focuses the beam onto the sample and the first filter (Schott RG715) removes any spurious second harmonic component from the beam (so that it does not reflect off of the sample and mix with the generated second harmonic). The spot size on the sample is just over 35 μm (full-width half-maximum). The second filter (Schott BG39) removes the fundamental component from the beam (so that only the second harmonic passes). The second lens (5 cm singlet) collimates the beam and focuses it into the photomultiplier tube (PMT). The second polarizer is a Glan-Thompson polarizer, which is set to p-polarization. Finally, the third filter (Semrock BrightLine 720 nm) simply increases the selectivity of the second harmonic versus the fundamental, and blocks some of the ambient light entering the PMT. We used a Hamamatsu R464 PMT biased at -1200 V. The PMT and the components along the optical path are placed under a light-absorbing enclosure to minimize ambient light contributions to noise. The signals from the PMT are provided gain through a Hamamatsu C6438 amplifier and then counted by a Stanford SR400 photon counter. For more accurate alignment needs, the focusing singlet is replaced with a 5x objective lens and a CCD camera is placed after the collimating singlet. This allows for imaging during alignment as well as a spot size of just under 20 μm.

Figure 9.2 shows the relevant section of the sample layout in our experiment. The SHE metal (yellow) forms a simple channel between two contacts (usually a layer of gold deposited on top). The laser spot probes this channel, which is designed to be as laterally small as possible (allowing for the spot size of the laser) to maximize the current density. Based upon the SHE geometry described in section 8.2, current passing in the direction of the arrow would generate spins on the top (probed) surface that are aligned along the up

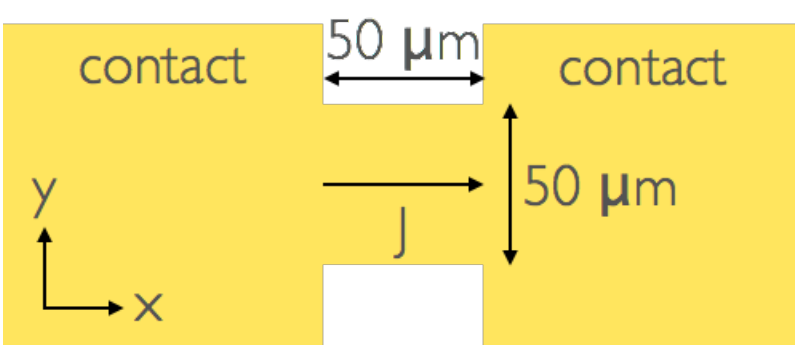

Figure 9. 2: Sample layout for detecting SHG due to spin accumulation from SHE. The SHE metal (yellow) is deposited onto an insulating substrate (typically silicon dioxide).

and down directions. The SHE metal must be thicker than its absorption depth for 800 nm wavelength light to prevent the oppositely-aligned spins on the bottom surface from contributing significantly (which counteracts the magnetic contrast from the top surface). We wire bonded each sample to a chip carrier, which inserts into the chip socket of a custom PCB that links the socket to an end-mount SMA connector by a coplanar waveguide.

An electrical signal synchronized to each laser pulse triggers a Stanford DG645 delay generator. This delay generator can frequency divide the trigger signal by an integer factor. In our case, our integer factor is 2, which allows us to modulate the measurement into two bins labeled 'A' and 'B' that represent I_+ and I_-, respectively. The ½-frequency signal is used to trigger both the pump pulse generator and the photon counter (for gating). Since the probe pulses are fixed and arrive once every 4 μs, the pump pulse waveform is triggered every 8 μs and has the shape shown in figure 9.3 programmed into the Agilent 33220A pulse generator. The time delay between the leading edges of the 'A' and 'B' bins is calibrated to the best of our ability so that the time delay Δt between a probe pulse and the nearest leading edge is the same for both bins. The two-channel photon counter is also triggered every 8 μs and is programmed to gate its counting so that each channel counts every other probe pulse. Again, the time delay between the gates is calibrated to the best of our ability. In this fashion, probe photons from I_+ and I_- are collected by bins 'A' and 'B', respectively. The dynamical time delay Δt probed can be changed by adjusting the pump delay from the delay generator.

A fairly well-behaved material to investigate using these methods is platinum. Since platinum does not oxidize at room ambient, no capping layer is required. This makes the SHG measurement much simpler to interpret, as the dominant contribution should come from the exposed surface of the platinum. We sputter-deposited 10 nm of platinum onto thermally-oxidized silicon chips. We then etched the pattern of figure 9.2 by ion milling using I-line photoresist as an etch mask. This etch mask was then removed by soaking in warm (65 °C) Baker PRS-3000 for one day. We then used a bi-layer lift-off as described in appendix D.1 to evaporate 80 nm thick gold contacts. The finished chips were finally adhered onto chip carriers using SPI flash-dry silver paint. After wire bonding, each sample exhibited an electrical resistance of around 35 Ω. Our pulse generator has a maximum output of 5 V, which (after accounting for impedance mismatch) provides 23.6

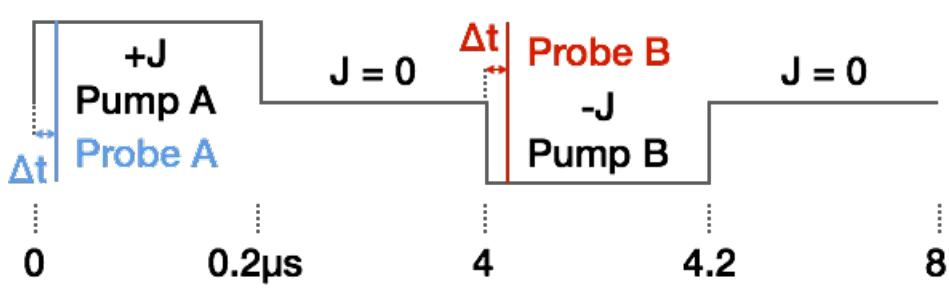

Figure 9. 3: Pump and probe pulse timing patterns and photon count binning.

MA/cm^2 through the channel. We also fabricated a similar sample with 20 nm of platinum instead. The electrical resistance of this sample was 17 Ω, which allows for 14.5 MA/cm^2 through the channel. We report measurements on these samples in the next section.

3. Detection of Spin Accumulation on Bare Platinum due to SHE

Figure 9.4 shows the pulse generator output (pump 'A' in the pattern of figure 9.3) as measured from the monitor output of the generator. Delayed by 4 μs from this output is an output designed to be the negative (pump 'B') of figure 9.4. We measured a time delay sweep using the Δt parameter as shown in figure 9.3 by sweeping the delay generator. The integration time at each time delay was 2000 s, which produced approximately 15000 photon counts per bin. Using these two bins, we constructed the asymmetry parameter A as given in equation 9.28. Figure 9.5 plots the SHG asymmetry from 10 nm of platinum versus the time delay for the geometry shown in figure 9.2 (where M_y is being probed) as well as the $\frac{\pi}{2}$ rotation of the sample from that geometry (where M_x is being probed). We immediately notice that the asymmetry more or less is proportional to the applied current. Since the asymmetry detects contributions that are odd in applied current, we attribute this result to the spin accumulation generated by the SHE. In other words, effects that are even in applied current such as Joule heating would not manifest here. Additionally, the spin accumulation oriented in the direction parallel to the current density is much less than

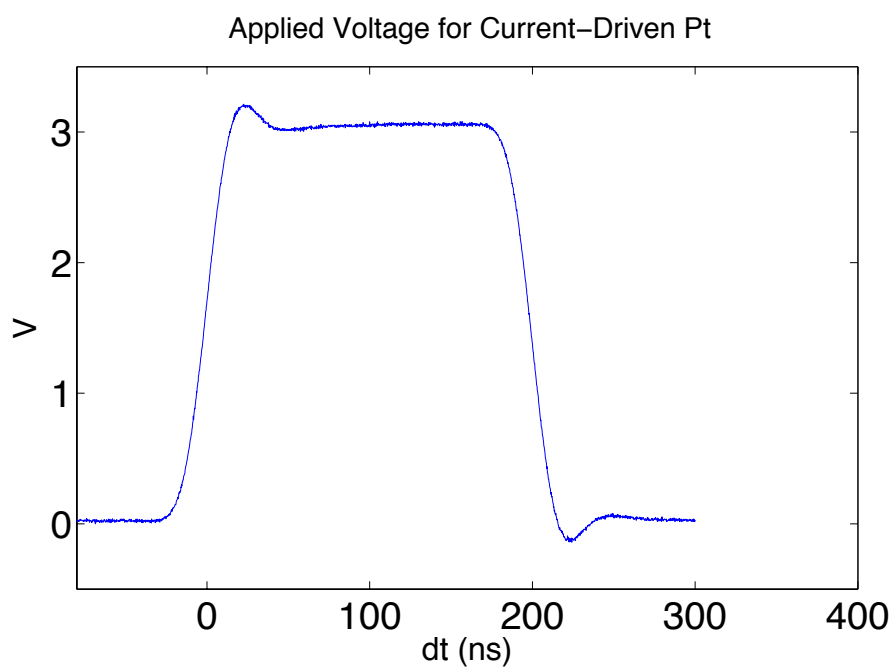

Figure 9. 4: Voltage pulse (positive half) applied using the arbitrary waveform generator as measured on its monitor output. The amplitude differs from the output by a constant while the shape does not account for additional distortion encountered downstream.

the spin accumulation oriented in the direction perpendicular to the current density. This agrees with the predictions made in section 8.2. We attribute the residual asymmetry of the rotated-sample measurement to a combination of three factors: non-collinear current density (an explanation used by previous work[91]), imperfect polarizer rotations leading to sensitivity to other magnetization components, and imperfect sample mounting leading to projections of other magnetization components along the axis of sensitivity.

The time axes in figures 9.4 and 9.5 are offset semi-arbitrarily such that the plots coincide. However, using a photodiode and a pair of identical cables, we confirmed to within a few nanoseconds that the measured asymmetry does coincide in time with the applied current. The plot also shows that at the time scales of tens of nanoseconds (the rise and fall times of the pump signal are approximately 30 ns and the jitter between pump and probe as limited by the gate generators on the photon counter is around 2 ns with bin 'B' having more jitter than bin 'A'), the spin accumulation equilibrates nearly instantaneously and no additional dynamics are observed. To our knowledge, this is the first SHE time dynamics measurement on bare metal with a resolution of tens of nanoseconds.

Figure 9.6 plots the peak asymmetry (taken at the time delay corresponding to the center of the pump pulse) versus the peak amplitude of the pump pulse (the current density scales linearly with voltage). The blue points are measured data and the red line is a linear fit that passes through the origin. The result shows that asymmetry also scales linearly with current density, which confirms the relationship given in equation 8.16.

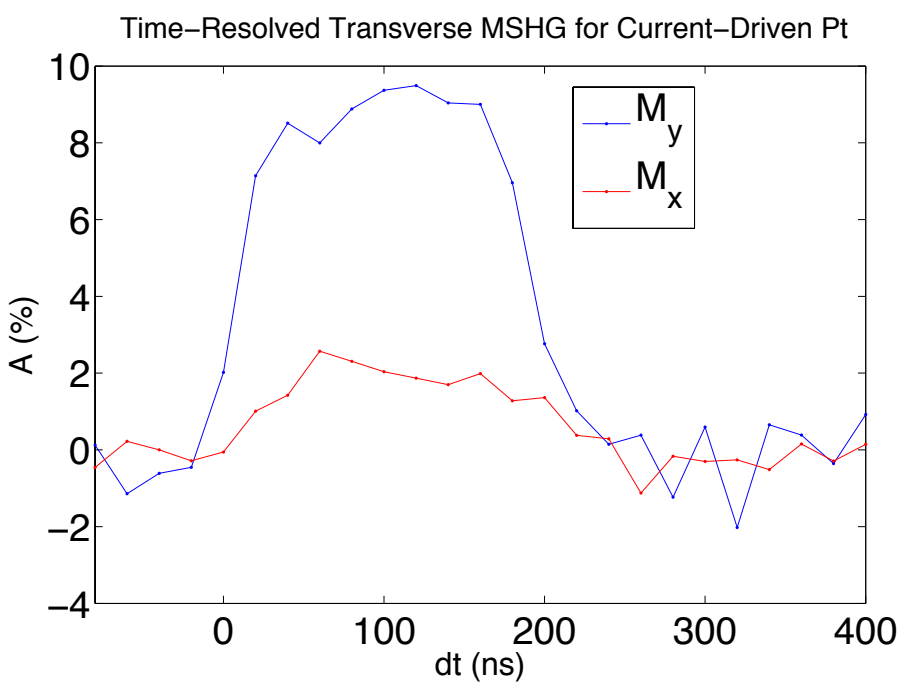

Figure 9. 5: Magnetic asymmetry versus time delay for platinum pumped by the current pulses shown in figure 9.4. Measured in orientations sensitive to the in-plane spin components parallel and perpendicular to the direction of the applied current.

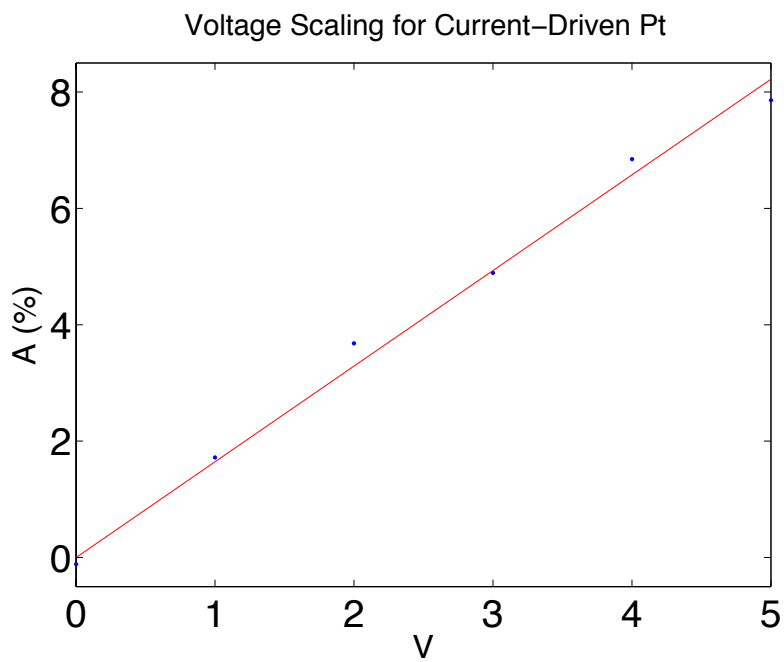

Figure 9. 6: Magnetic asymmetry versus applied voltage for platinum pumped by the current pulses shown in figure 9.4. Measured at dt = 100 ns as determined by figure 9.5.

Figure 9.7 plots the peak asymmetry from 20 nm of platinum versus the rotation angle of the sample about the sample plane normal, where the angle of the above measurements is taken to be 0. The blue points are measured data and the red curve is a sinusoidal fit that allows for both amplitude and phase degrees of freedom. The result shows that the asymmetry follows the expected cosine dependence on angle for the projection of the spin accumulation along the direction of magnetic sensitivity. This measurement was performed using the 5x objective and imaging alignment described in section 9.2.

This work is still ongoing as of the time of writing. The technique shows strong potential and many more measurements can be performed. For example, other material systems such as tungsten and tantalum can be measured to check for asymmetry generated by SHE. Control material systems such as copper and aluminum can be checked to ensure that no asymmetry is observed. Even faster pump pulses and finer time resolution can be achieved with faster pulse generators and impedance-matched sample designs. Additionally, an optical pump pulse can be added to induce ultrafast demagnetization[94] during the electrical pump in order to study the remagnetization dynamics. Different interfaces achieved using various capping layers can be measured to attempt to distinguish interfacial spin effects[95]. Finally, all of the above measurements can be compared to MOKE (which can be performed simultaneously) in order to distinguish bulk effects from interface effects.

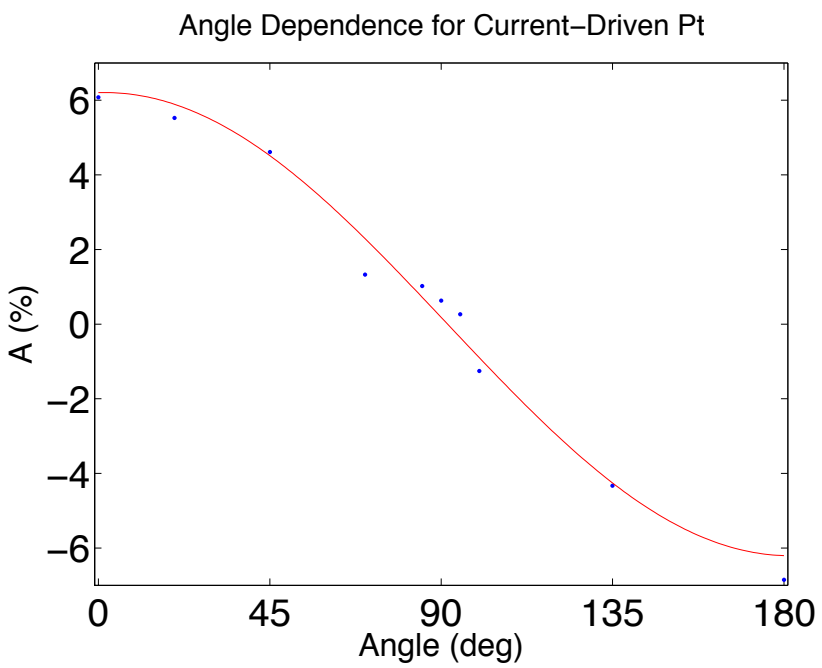

Figure 9. 7: Magnetic asymmetry versus rotation angle about sample plane normal for platinum pumped by the current pulses shown in figure 9.4. Measured at dt = 100 ns as determined by figure 9.5.

Chapter 10. Conclusion

In this dissertation, we have researched the behavior of nearly-single-domain nanomagnets and developed some possible applications in both spin logic and spin memory devices. We have also analyzed, simulated, and experimentally imaged the behavior of nanomagnetic logic chains in the context of transmitting information through interconnects. Finally, we have adapted an experimental technique to directly probe the spin Hall effect, motivated as an energy-efficient mechanism for energetically exciting spin logic and spin memory devices.

As of the time of writing, there exists a large amount of ongoing work on the spin Hall effect. We expect our work on it to lead to more thorough experimentation with various materials and contribute to advancing the understanding of the physics of the spin Hall effect. Further research into energy-efficient spin-transfer mechanisms (likely extending beyond spin Hall effect) is paramount for spintronics, because it most directly pushes spin devices toward being able to leverage their fundamental energy-dissipation advantages over charge-based devices. Meanwhile, we do not believe that field-coupled nanomagnetic logic in its current incarnations is worth pursuing any further due to the far better interconnect reliability and speed predicted for torque-coupled devices. Aside from efficient spin-charge coupling mechanisms, reducing leakage in spin logic systems will likely also be the focus of a good deal of future work.

Looking forward, we believe that due to innate non-volatility, spin-based systems integrating logic and memory would play a major role in data-centric computing[96]. Commercially viable spin systems of the future may combine many ideas from concepts that currently seem to lack promise. Spintronics research has so far been tremendously rich in both the physics involved and the variety of devices studied, leaving a very large amount of space for innovation. The inherent properties of spin are incredibly attractive and will continue to inspire research and development in this field.

References

[1] M. T. Niemier, G. H. Bernstein, G. Csaba, A. Dingler, X. S. Hu, S. Kurtz, S. Liu, J. Nahas, W. Porod, M. Siddiq, and E. Varga, J Phys Condens Matter **23**, 493202 (2011).

[2] E. Pop, Nano Research **3**, 147 (2010).

[3] S. Gustavsson, *Blue LEDs – Filling the World with New Light* (The Royal Swedish Academy of Sciences, 2014), pp. 1–5.

[4] S. Salahuddin and S. Datta, Appl. Phys. Lett. **90**, 93503 (2007).

[5] F. M. Spedalieri, A. P. Jacob, D. E. Nikonov, and V. P. Roychowdhury, IEEE Trans Nano **10**, 537 (2011).

[6] T. N. Theis and P. M. Solomon, Science **327**, 1600 (2010).

[7] D. B. Carlton, B. Lambson, A. Scholl, A. Young, P. D. Ashby, S. D. Dhuey, and J. Bokor, IEEE Trans Nano **11**, 760 (2012).

[8] D. B. Carlton, N. C. Emley, E. Tuchfeld, and J. Bokor, Nano Lett. **8**, 4173 (2008).

[9] F. Pulizzi, Nature Materials **11**, 367 (2012).

[10] J. Kiermaier, S. Breitkreutz, I. Eichwald, M. Engelstädter, X. Ju, G. Csaba, D. Schmitt-Landsiedel, and M. Becherer, J. Appl. Phys. **113**, 17B902 (2013).

[11] S. Breitkreutz, J. Kiermaier, I. Eichwald, X. Ju, G. Csaba, D. Schmitt-Landsiedel, and M. Becherer, IEEE Trans. Magn. **48**, 4336 (2012).

[12] B. Lambson, D. Carlton, and J. Bokor, Phys. Rev. Lett. **107**, 10604 (2011).

[13] I. Eichwald, S. Breitkreutz, G. Ziemys, G. Csaba, W. Porod, and M. Becherer, Nanotechnology **25**, 335202 (2014).

[14] S. A. Wolf, Science **294**, 1488 (2001).

[15] A. Imre, G. Csaba, L. Ji, A. Orlov, G. H. Bernstein, and W. Porod, Science **311**, 205 (2006).

[16] S. Datta, S. Salahuddin, and B. Behin-Aein, Appl. Phys. Lett. **101**, 252411 (2012).

[17] E. Varga, A. Orlov, M. T. Niemier, X. S. Hu, G. H. Bernstein, and W. Porod, IEEE Transactions on Nanotechnology **9**, 668 (2010).

[18] B. Lambson, Z. Gu, M. Monroe, S. Dhuey, A. Scholl, and J. Bokor, Appl. Phys. A **111**, 413 (2013).

[19] D. E. Nikonov, G. I. Bourianoff, T. Ghani, and I. A. Young, in *IEEE International Magnetics Conference (Intermag)* (2012), pp. BT–08.

[20] B. Behin-Aein, D. Datta, S. Salahuddin, and S. Datta, Nature Nanotech **5**, 266 (2010).

[21] J. A. Currivan, Youngman Jang, M. D. Mascaro, M. A. Baldo, and C. A. Ross, IEEE Magn. Lett. **3**, 3000104 (2012).

[22] S. S. P. Parkin, M. Hayashi, and L. Thomas, Science **320**, 190 (2008).

[23] E. C. Stoner and E. P. Wohlfarth, Philosophical Transactions of the Royal Society of London. Series a. Mathematical and Physical Sciences **240**, 599 (1948).

[24] J. D. Jackson, *Classical Electrodynamics*, 3rd ed. (Wiley, 1998).

[25] R. Cowburn and M. Welland, Phys. Rev. B **58**, 9217 (1998).
[26] B. Hillebrands and K. Ounadjela, *Spin Dynamics in Confined Magnetic Structures I* (Springer Science & Business Media, 2002).
[27] D. C. Ralph and M. D. Stiles, J Magn Magn Mater **320**, 1190 (2008).
[28] J. Xiao, Spin-Transfer Torque in Magnetic Nanostructures, Georgia Institute of Technology, 2006.
[29] A. Thiaville, Y. Nakatani, J. Miltat, and Y. Suzuki, Europhys. Lett. **69**, 990 (2007).
[30] C. Melcher and M. Ptashnyk, SIAM J. Math. Anal. **45**, 407 (2013).
[31] B. Hillebrands and K. Ounadjela, *Spin Dynamics in Confined Magnetic Structures II* (Springer Science & Business Media, 2003).
[32] M. P. Sharrock, J. Appl. Phys. **76**, 6413 (1994).
[33] W. F. Brown Jr, Physical Review **130**, 1677 (1963).
[34] D. D. Tang and Y.-J. Lee, *Magnetic Memory* (Cambridge University Press, 2010).
[35] M. D'Aquino, C. Serpico, G. Coppola, I. D. Mayergoyz, and G. Bertotti, Journal of Applied Physics **99**, 08B905 (2006).
[36] M. J. Donahue and D. G. Porter, editors, *Http://Math.Nist.Gov/Oommf/Doc/* (2008).
[37] N. A. Spaldin, *Magnetic Materials* (Cambridge University Press, 2003).
[38] R. Cowburn, A. Adeyeye, and M. Welland, Phys. Rev. Lett. **81**, 5414 (1998).
[39] R. Cowburn and M. Welland, Appl. Phys. Lett. **72**, 2041 (1998).
[40] M. T. Niemier, E. Varga, G. H. Bernstein, W. Porod, M. T. Alam, A. Dingler, A. Orlov, and X. S. Hu, IEEE Trans Nano **11**, 220 (2012).
[41] D. H. Staelin, A. W. Morgenthaler, and J. A. Kong, *Electromagnetic Waves* (Prentice Hall, 1993).
[42] B. Lambson, Energy Efficient Digital Logic Using Nanoscale Magnetic Devices, University of California, Berkeley, 2013.
[43] R. Cowburn, Phys. Rev. B **65**, 092409 (2002).
[44] B. Lambson, Z. Gu, D. Carlton, S. Dhuey, A. Scholl, A. Doran, A. Young, and J. Bokor, Appl. Phys. Lett. **100**, 152406 (2012).
[45] D. B. Carlton, B. Lambson, A. Scholl, A. Young, S. D. Dhuey, P. D. Ashby, E. Tuchfeld, and J. Bokor, IEEE Trans Nano **10**, 1401 (2011).
[46] B. Lambson, Z. Gu, J. Bokor, D. Carlton, S. Dhuey, and A. Scholl, in *IEEE International Electron Devices Meeting (IEDM)* (IEEE, 2012), p. 11.5.1.
[47] G. Csaba and W. Porod, in *International Workshop on Computational Electronics* (IEEE, 2010), p. 311.
[48] I. Eichwald, A. Bartel, J. Kiermaier, S. Breitkreutz, G. Csaba, D. Schmitt-Landsiedel, and M. Becherer, IEEE Trans. Magn. **48**, 4332 (2012).
[49] M. T. Alam, S. J. Kurtz, M. A. J. Siddiq, M. T. Niemier, G. H. Bernstein, X. S. Hu, and W. Porod, IEEE Trans Nano **11**, 273 (2012).
[50] D. Carlton, Nanomagnetic Logic, University of California, Berkeley, 2012.
[51] I. Eichwald, J. Kiermaier, S. Breitkreutz, J. Wu, G. Csaba, D. Schmitt-Landsiedel, and

M. Becherer, IEEE Trans. Magn. **49**, 4468 (2013).
[52] S. Breitkreutz, J. Kiermaier, I. Eichwald, C. Hildbrand, G. Csaba, D. Schmitt-Landsiedel, and M. Becherer, IEEE Trans. Magn. **49**, 4464 (2013).
[53] J. Stöhr and H. C. Siegmann, *Magnetism* (Springer Science & Business Media, 2007).
[54] G. Denbeaux, P. Fischer, G. Kusinski, M. Le Gros, A. Pearson, and D. Attwood, Magnetics, IEEE Transactions on **37**, 2764 (2001).
[55] A. Doran, M. Church, T. Miller, G. Morrison, A. T. Young, and A. Scholl, Journal of Electron Spectroscopy and Related Phenomena **185**, 340 (2012).
[56] M. T. Bryan, D. Atkinson, and R. P. Cowburn, Appl. Phys. Lett. **85**, 3510 (2004).
[57] M. T. Alam, M. J. Siddiq, G. H. Bernstein, M. Niemier, W. Porod, and X. S. Hu, IEEE Transactions on Nanotechnology **9**, 348 (2010).
[58] B. J. Setlik, Electromigration Characterization of Aluminum-Copper Alloy Interconnects, University of Rhode Island, 2002.
[59] *Http://Www-Als.Lbl.Gov/Index.Php/Beamlines/Storage-Ring-Parameters.Html* (Lawrence Berkeley National Laboratory, n.d.).
[60] A. F. G. Leontowich and A. P. Hitchcock, J. Vac. Sci. Technol. B **30**, 030601 (2012).
[61] J. Vogel, W. Kuch, M. Bonfim, J. Camarero, Y. Pennec, F. Offi, K. Fukumoto, J. Kirschner, A. Fontaine, and S. Pizzini, Appl. Phys. Lett. **82**, 2299 (2003).
[62] K. L. Wang, J. G. Alzate, and P. Khalili Amiri, J. Phys. D: Appl. Phys. **46**, 074003 (2013).
[63] L. Liu, C.-F. Pai, Y. Li, H. W. Tseng, D. C. Ralph, and R. A. Buhrman, Science **336**, 555 (2012).
[64] M. I. Dyakonov and V. I. Perel, Jetp Letters **13**, 657 (1971).
[65] L. Liu, T. Moriyama, D. C. Ralph, and R. A. Buhrman, Phys. Rev. Lett. **106**, 036601 (2011).
[66] C.-F. Pai, L. Liu, Y. Li, H. W. Tseng, D. C. Ralph, and R. A. Buhrman, Appl. Phys. Lett. **101**, 122404 (2012).
[67] Z. Tang, Y. Kitamura, E. Shikoh, Y. Ando, T. Shinjo, and M. Shiraishi, Appl. Phys. Express **6**, 083001 (2013).
[68] T. Seki, Y. Hasegawa, S. Mitani, S. Takahashi, H. Imamura, S. Maekawa, J. Nitta, and K. Takanashi, Nature Materials **7**, 125 (2008).
[69] Y. Niimi, Y. Kawanishi, D. H. Wei, C. Deranlot, H. X. Yang, M. Chshiev, T. Valet, A. Fert, and Y. Otani, Phys. Rev. Lett. **109**, 156602 (2012).
[70] Y. Niimi, M. Morota, D. H. Wei, C. Deranlot, M. Basletic, A. Hamzic, A. Fert, and Y. Otani, Phys. Rev. Lett. **106**, 126601 (2011).
[71] Y. Niimi, H. Suzuki, Y. Kawanishi, Y. Omori, T. Valet, A. Fert, and Y. Otani, Phys. Rev. B **89**, 054401 (2014).
[72] Y. K. Kato, R. C. Myers, A. C. Gossard, and D. D. Awschalom, Science **306**, 1910 (2004).
[73] A. R. Mellnik, J. S. Lee, A. Richardella, J. L. Grab, P. J. Mintun, M. H. Fischer, A. Vaezi, A.

Manchon, E. A. Kim, N. Samarth, and D. C. Ralph, Nature **511**, 449 (2014).
[74] J. Balakrishnan, G. K. W. Koon, A. Avsar, Y. Ho, J. H. Lee, M. Jaiswal, S.-J. Baeck, J.-H. Ahn, A. Ferreira, M. A. Cazalilla, A. H. C. Neto, and B. O. zyilmaz, Nature Communications **5**, 4748 (2014).
[75] A. Bérard and H. Mohrbach, Phys Lett A **352**, 190 (2006).
[76] S.-Q. Shen, Phys. Rev. B **70**, 081311 (2004).
[77] P. M. Haney, H.-W. Lee, K.-J. Lee, A. Manchon, and M. D. Stiles, Phys. Rev. B **87**, 174411 (2013).
[78] R. V. Shchelushkin and A. Brataas, Phys. Rev. B **71**, 045123 (2005).
[79] S. Zhang, Phys. Rev. Lett. **85**, 393 (2000).
[80] S. Kaka and S. E. Russek, Appl. Phys. Lett. **80**, 2958 (2002).
[81] D. Bhowmik, L. You, and S. Salahuddin, Nature Nanotech **9**, 59 (2013).
[82] H. Jaffrès, D. Lacour, F. Nguyen Van Dau, J. Briatico, F. Petroff, and A. Vaurès, Phys. Rev. B **64**, 064427 (2001).
[83] W. T. Coffey and Y. P. Kalmykov, Journal of Applied Physics **112**, 121301 (2012).
[84] A. Kirilyuk and T. Rasing, Optical Society of America Journal B **22**, 148 (2005).
[85] Y. Fan, K. J. Smith, G. Luepke, A. T. Hanbicki, R. Goswami, C. H. Li, H. B. Zhao, and B. T. Jonker, Nature Nanotech **8**, 438 (2013).
[86] M. Fiebig, D. Frohlich, G. Sluyterman, and R. V. Pisarev, Appl. Phys. Lett. **66**, 2906 (1995).
[87] I. E. Radu, Ultrafast Electron, Lattice and Spin Dynamics on Rare Earth Metal Surfaces. Investigated with Linear and Nonlinear Optical Techniques, Freien Universität Berlin, 2006.
[88] T. Rasing, J Magn Magn Mater **175**, 35 (1997).
[89] R.-P. Pan, H. D. Wei, and Y. R. Shen, Phys. Rev. B **39**, 1229 (1989).
[90] L. Liu, C.-T. Chen, and J. Z. Sun, Nature Physics **10**, 561 (2014).
[91] O. M. J. van t Erve, A. T. Hanbicki, K. M. McCreary, C. H. Li, and B. T. Jonker, Appl. Phys. Lett. **104**, 172402 (2014).
[92] A. Melnikov, I. Razdolski, T. O. Wehling, E. T. Papaioannou, V. Roddatis, P. Fumagalli, O. Aktsipetrov, A. I. Lichtenstein, and U. Bovensiepen, Phys. Rev. Lett. **107**, 076601 (2011).
[93] T. Gerrits, H. A. M. Van Den Berg, J. Hohlfeld, L. Bär, and T. Rasing, Nature **418**, 509 (2002).
[94] E. Beaurepaire, J. C. Merle, A. Daunois, and J. Y. Bigot, Phys. Rev. Lett. **76**, 4250 (1996).
[95] X. Wang, J. Xiao, A. Manchon, and S. Maekawa, Phys. Rev. B **87**, 081407 (2013).
[96] *Http://Research.Ibm.com/Articles/Datacentricdesign/* (International Business Machines Corporation, n.d.).

Appendix A. OOMMF Programs

1. Exploring Configurational Phase Diagrams

Due to configurational anisotropy, nearly-single-domain magnets typically have a set of stable magnetic configurations. One can determine which one in the set has the overall lowest energy by changing the size and shape of the magnet. For example, squares can take on flower, leaf, and linear combinations of flower and leaf configurations depending on the thickness. Since flower and leaf configurations have different average magnetization angles, one can initialize the square's magnetization along an angle between the two and allow it to adiabatically relax into its stable configuration. By finding this configuration for a range of lateral sizes and thicknesses, one can build a configurational phase diagram. The following OOMMF program serves this purpose by initializing and calculating the time evolution of the magnet until its time rate of change becomes very slow, and then stores the end result.

```
# Grid sizes
set xcell 1e-9
set ycell 1e-9
set zcell 1e-9

# Image sizes
Parameter xpix 27
Parameter ypix 27
Parameter zpix 24

set width  [expr {$ypix*$ycell}]
set length [expr {$xpix*$xcell}]
set thick  [expr {$zpix*$zcell}]

set PI                  [expr {4*atan(1.)}]
set Sim 1   ;# Random seed
set As 13e-12           ;# Exchange constant
set Ms 800e3            ;# Saturation magnetization
set alpha 0.02          ;# Damping constant
set gamma 2.21e5        ;# Gyromagnetic ratio
set Temp 0              ;# Temperature
set timestep 1e-13      ;# Simulation time step
set dmdtstop 1          ;# Simulation dm/dt end
set infile square.ppm;# Input image
set outfile configurational        ;# Output filename
set theta 22.5          ;# Initial angle

Specify Oxs_ImageAtlas:atlas1 [subst {
  xrange {0 $width}
  yrange {0 $length}
  zrange {0 $thick}
  image $infile
  viewplane xy
  colormap {
     white nonmagnetic
```

```
    black magnetic1
  }
}]

Specify Oxs_RectangularMesh:mesh [subst {
  cellsize {$xcell $ycell $zcell}
  atlas :atlas1
}]

Specify Oxs_UniformExchange [subst {
  A  $As
}]

Specify Oxs_Demag {}

Specify UHH_ThetaEvolve [subst {
  do_precess 1
  gamma_LL $gamma
  alpha $alpha
  fixed_timestep $timestep
  temperature $Temp
  uniform_seed $Sim
}]

Specify Oxs_TimeDriver [subst {
 basename $outfile
 evolver UHH_ThetaEvolve
 stopping_dm_dt $dmdtstop
 mesh :mesh
 Ms {
        Oxs_AtlasScalarField {
                atlas :atlas1
                values {
                        nonmagnetic  0
                        magnetic1 $Ms
                }
        }
}
 m0 {
        Oxs_AtlasVectorField {
                atlas :atlas1
                default_value { 0 0 0 }
                values {
                        nonmagnetic { 0 0 0 }
                        magnetic1 { [expr {cos($PI*$theta/180.)}] [expr {sin($PI*$theta/180.)}] 0 }
                }
        }
 }
}]

Destination archive mmArchive
Schedule Oxs_TimeDriver::Magnetization archive Stage 1
Schedule DataTable archive Stage 1
```

2. Characterizing Switching Magnetic Fields

One way of reducing the degrees of freedom of an arbitrary magnet's anisotropy down to a second-order (uniaxial and biaxial) approximation is by matching the applied magnetic fields required to switch the magnet between the energy minima. The following OOMMF program serves this purpose by first allowing the magnetization of a magnet to relax along an initial energy local minimum until its time rate of change becomes very slow, then applying a specified magnetic field and calculating its time evolution until its time rate of change becomes very slow, and finally removing all applied magnetic fields and allowing it to relax. By sweeping the applied magnetic field's strength, one can find the critical switching magnetic fields needed to rotate the magnetization. The result at the end of each of the three steps described above can be stored.

```
# Grid sizes
set xcell 5e-9
set ycell 5e-9
set zcell 4e-9

# Image sizes
set xpix 30
set ypix 98
set zpix 3

set width  [expr {$ypix*$ycell}]
set length [expr {$xpix*$xcell}]
set thick  [expr {$zpix*$zcell}]

set Sim 1   ;# Random seed
set As 13e-12          ;# Exchange constant
set Ms 800e3           ;# Saturation magnetization
set alpha 0.02         ;# Damping constant
set gamma 2.21e5       ;# Gyromagnetic ratio
set Temp 0             ;# Temperature
set timestep 1e-13     ;# Simulation time step
set dmdtstop 5         ;# Simulation dm/dt end
Parameter fieldx 40    ;# Applied field (x, mT)
Parameter fieldy 0     ;# Applied field (y, mT)
set infile biaxl00.bmp          ;# Input image
set outfile biax       ;# Output filename

Specify Oxs_ImageAtlas:atlas [subst {
 xrange {0 $length}
 yrange {0 $width}
 zrange {0 $thick}
 image $infile
 viewplane xy
 colormap {
   white nonmagnetic
   black up
   red left
   blue right
   green down
 }
}]

Specify Oxs_RectangularMesh:mesh [subst {
```

```
  cellsize {$xcell $ycell $zcell}
  atlas :atlas
}]

Specify Oxs_UniformExchange [subst {
  A  $As
}]

Specify Oxs_Demag {
}

Specify Oxs_UZeeman [subst {
  multiplier 795.77472
  Hrange {
    { 0 0 0 $fieldx $fieldy 0 1 }
    { $fieldx $fieldy 0 0 0 0 1 }  }
}]

Specify UHH_ThetaEvolve [subst {
  do_precess 1
  gamma_LL $gamma
  alpha $alpha
  fixed_timestep $timestep
  temperature $Temp
  uniform_seed $Sim
}]

Specify Oxs_TimeDriver [subst {
  basename $outfile
  evolver UHH_ThetaEvolve
  stopping_dm_dt $dmdtstop
  mesh :mesh
  Ms {
        Oxs_AtlasScalarField {
                atlas :atlas
                values {
                        nonmagnetic 0
                        right $Ms
                        up $Ms
                        down $Ms
                        left $Ms
                }
        }
  }
  m0 {  Oxs_AtlasVectorField {
                atlas :atlas
                values {
                        nonmagnetic { 0 0 0 }
                        right { 1 0 0 }
                        up { 0 1 0 }
                        down { 0 -1 0 }
                        left { -1 0 0 }
                }
        }
  }
}]

#Destination archive mmArchive
#Schedule Oxs_TimeDriver::Magnetization archive Stage 1
#Schedule DataTable archive Stage 1
```

3. Applying Piecewise Linear Magnetic Fields

In simulation of clock pulses one would like to apply a time-dependent magnetic field that has a simple form while being a good approximation of realistic pulses. The most typical clock pulses can be characterized by a rise time, a peak amplitude duration, and a fall time. The following OOMMF program makes a piecewise linear approximation of this pulse shape and applies it uniformly in all space at the start of the simulation. The result after a specified amount of simulation time can be stored. Adjustments are required for different directions of applied magnetic field.

```
# Grid sizes
set xcell 1e-8
set ycell 1e-8
set zcell 12e-9

# Image sizes
set xpix 279
Parameter ypix 46
set zpix 1

set width  [expr {$ypix*$ycell}]
set length [expr {$xpix*$xcell}]
set thick  [expr {$zpix*$zcell}]

Parameter Sim 1       ;# Random seed
set As 13e-12         ;# Exchange constant
set Ms 800e3          ;# Saturation magnetization
set alpha 0.02        ;# Damping constant
set gamma 2.21e5      ;# Gyromagnetic ratio
set Temp 300          ;# Temperature
set timestep 1e-13    ;# Simulation time step
set timestop 30e-9    ;# Simulation end time
set infile shallower[expr {$ypix-5}].bmp    ;# Input image
set outfile xm1fastclock/chain_${ypix}_${Sim}          ;# Output filename
set PAmp 84           ;# Pulse amplitude (mT)
set PRise 2e-10       ;# Pulse rise time
set PFall 3e-10       ;# Pulse fall time
set PHold 2e-9        ;# Pulse peak width

Specify Oxs_ImageAtlas:atlas [subst {
 xrange {0 $length}
 yrange {0 $width}
 zrange {0 $thick}
 image $infile
 viewplane xy
 colormap {
   white nonmagnetic
   black right
   red up
   blue down
   green left
 }
}]
```

```
Specify Oxs_RectangularMesh:mesh [subst {
  cellsize {$xcell $ycell $zcell}
  atlas :atlas
}]

Specify Oxs_UniformExchange [subst {
  A  $As
}]

Specify Oxs_Demag {
}

Specify Oxs_ScriptUZeeman [subst {
  script_args total_time
  script {PulseField $PAmp $PRise $PHold $PFall}
  multiplier 795.77472
}]

proc PulseField { PAmp PRise PHold PFall total_time} {
        if {$total_time < $PRise} {
                set Hx [expr $PAmp * ( $total_time / $PRise )]
                set dHx [expr $PAmp / $PRise]
                return [list $Hx 0 0 $dHx 0 0]
        } elseif {$total_time <= [expr $PRise + $PHold]} {
                return [list $PAmp 0 0 0 0 0]
        } elseif {$total_time < [expr $PRise + $PHold + $PFall]} {
                set Hx [expr $PAmp * ( $PFall + $PHold + $PRise - $total_time ) / $PFall]
                set dHx [expr -$PAmp / $PFall]
                return [list $Hx 0 0 $dHx 0 0]
        } else { return [list 0 0 0 0 0 0] }
}

Specify UHH_ThetaEvolve [subst {
  do_precess 1
  gamma_LL $gamma
  alpha $alpha
  fixed_timestep $timestep
  temperature $Temp
  uniform_seed $Sim
}]

Specify Oxs_TimeDriver [subst {
  basename $outfile
  evolver UHH_ThetaEvolve
  mesh :mesh
  stopping_time $timestop
  Ms {
        Oxs_AtlasScalarField {
                atlas :atlas
                values {
                        nonmagnetic 0
                        right $Ms
                        up $Ms
                        down $Ms
                        left $Ms
                }
        }
  }
  m0 {  Oxs_AtlasVectorField {
```

```
                atlas :atlas
                values {
                        nonmagnetic { 0 0 0 }
                        right { 1 0 0 }
                        up { 0 1 0 }
                        down { 0 -1 0 }
                        left { -1 0 0 }
                }
        }
 }
}]

#Destination archive mmArchive
#Schedule Oxs_TimeDriver::Magnetization archive Stage 1
#Schedule DataTable archive Stage 1
```

Appendix B. MATLAB Programs

1. Exploring Chains with Second-Order Anisotropy

The dynamics of nanomagnets with any combination of uniaxial and biaxial anisotropy can be modeled using macro-spin simulations based on existing code. The following MATLAB program creates chains of macro-spins with anisotropy parameters, dimensions, and temperature, and checks for correct signal propagation. If the chain behaves correctly over a certain number of simulations, this program stores the corresponding anisotropy values and simulation time. An arbitrary range of anisotropy values can be checked. This program employs an algorithm that assumes a continuous region of anisotropy values works correctly. The algorithm checks each biaxial value, and for each biaxial value, it starts at the lowest working uniaxial value for the last biaxial value and checks both lower and higher uniaxial values until it finds a certain number of uniaxial values in a row that do not work. This number, called the buffer, can easily be changed up to an equivalent of simply brute force checking all combinations of anisotropy values. The code below is configured to check horizontal chains, however the initialization and correctness conditions for vertical chains can easily be implemented. Arbitrary layouts of macro-spins, such as majority logic gates, can also be simulated by likewise implementing the appropriate correctness conditions. The inputs to the function are the array of biaxial values, the array of uniaxial values, the lateral size of the nanomagnets (assumed to be square), the gap size between nanomagnets, and the temperature, respectively. The nanomagnet thickness is currently fixed but can easily be changed in line 4. Code inherited from previous work[42] including the singlespin library and the couplingmatrix and biaxtiltevolve functions is required for this code to function.

```
function mySimAnisotropy(kb,ku,sz,spc,temp)
nMagnets=12+2;  % Number of magnets in chain plus input and block
period=sz+spc;  % Center-to-center spacing of magnets (nm)
dimension=[sz sz 12];   % Dimensions of magnets (nm)
timestep=1e-12; % Simulation time step (s)
input=1;    % input magnetization
filename=['ZGU' num2str(temp) 'K12x' num2str(sz) '+' num2str(spc) '.mat'];
Hmax=0.1/cnst.mu_0; % Maximum applied field (A/m)
Hstbl=0.05/cnst.mu_0;   % Stabilization field on block (A/m)
stage=[0 0 0 0 6000];   % Number of steps per stage
stopstep=sum(stage);    % Total simulation steps
HT=zeros(stopstep,3);   % Set applied field vs. time
HT(:,1)=Hmax*[zeros(stage(1),1);
        (linspace(0,1,stage(2)).*ones(1,stage(2)))';
        ones(stage(3),1);
        (linspace(1,0,stage(4)).*ones(1,stage(4)))';
        zeros(stage(5),1)];

nSims=2+round(temp*18/300); % Number of simulations
lengthku=length(ku);    % Number of uniaxial anisotropy values
```

```
lengthkb=length(kb);    % Number of biaxial anisotropy values
volume=prod(dimension)*1e-27;   % Volume of magnets (m^3)
Eb=kb*volume/(4*cnst.q);    % Biaxial energy (eV)
Eu=ku*volume/cnst.q;    % Uniaxial energy (eV)
limitstep=stopstep/2;   % Cutoff simulation step for stuck magnets
maxbuffer=lengthku;
limitbuffer=2;  % Maximum number of nonworking ku values to check
clockstage=sum(stage(1:2));
lastindex=1;

for ikb=1:lengthkb
   scanright=false;
   scanup=false;
   buffer=0;
   thisindex=lengthku;
   iku=lastindex;
   while ~scanright
      thisku=ku(iku);
      thiskb=kb(ikb);
      correct=ones(nSims,nMagnets);
      chainmt=zeros(nSims,nMagnets,3);
      scan=false;
      times=zeros(nSims,1);
      iSim=1; % Start simulation
      while ~scan
         tic;
         clear chain
         chain(nMagnets)=singlespin;
         for i=1:nMagnets
            chain(i).dim=dimension;
            if clockstage>0
               if mod(i,2)==0
                  chain(i).initialize([0 1 0]);
               else
                  chain(i).initialize([0 -1 0]);
               end
            else
               chain(i).initialize([1 0 0]);
            end
            chain(i).Eu=[0 -Eu(iku) 0];
            chain(i).Eb=[-Eb(ikb) 0];
            chain(i).position=[(i-1)*period 0 0];
            chain(i).temp = temp;
         end
         chain(1).initialize([0 -1 0]);
         chain(nMagnets).initialize([1 0 0]);
         coupling=couplingmatrix(chain);
         options=optimset('Display', 'off','Algorithm',{'levenberg-marquardt',0},'TolX',1e-5,'Jacobian','off');
         for time=2:stopstep
            Happ=HT(time,:);
            if time>sum(stage(1:2))
               chain(1).evolve([0 input 0],[0 0 0]);
            else
               chain(1).evolve([0 -1 0],[0 0 0]);
            end
            chain(nMagnets).evolve([1 0 0],[0 0 0]);
            MT=zeros(nMagnets,3);
            for i=1:nMagnets
               MT(i,:)=chain(i).MT(time-1,:);
            end
```

```
      for i = 2:nMagnets-1
         Hnn=[0 0 0];
         for j=1:nMagnets
            Hnn=Hnn+[sum(coupling(1,:,i,j).*MT(j,:)) sum(coupling(2,:,i,j).*MT(j,:)) sum(coupling(3,:,i,j).*MT(j,:))];
         end
         if i==nMagnets
            Hnn=Hnn+[Hstbl 0 0];
         end
         chain(i).biaxtiltevolve(timestep,temp,Happ+Hnn,options)
      end
      nFlipped=0;
      for i=2:nMagnets-1
         if abs(chain(i).MT(time,2))>(1/sqrt(2))
            nFlipped=nFlipped+1;
         end
      end
      if time>limitstep && nFlipped==0
         break;  % All magnets stuck
      end
      if nFlipped>=nMagnets-2
         break;  % All magnets flipped
      end
   end
   for i=1:nMagnets
       chainmt(iSim,i,:) = chain(i).MT(time,:);
       if (i < nMagnets-1 && chain(i).MT(time,2)*chain(i+1).MT(time,2)>-0.5)
         correct(iSim,i)=0;  % Count errors
       end
   end
   times(iSim)=time*timestep;
   disp(['kb: ' num2str(thiskb) ' ku: ' num2str(thisku) ' Sim: ' num2str(iSim) ' Time: ' num2str(times(iSim))])
   err=find(correct(iSim,:)==0);
   if isempty(err)
      disp('No errors');
   else
      disp(['Error(s): ' num2str(err)]);
      scan=true;
   end
   iSim=iSim+1;
   if iSim>nSims
      break;  % End simulation
   end
   toc
end
kbs=thiskb;
kus=thisku;
ts=times;
if ~scan
   if (exist(fullfile(cd,filename),'file') ~= 0)
      load(fullfile(cd,filename))
      kbs = [kbs thiskb];
      kus = [kus thisku];
      ts = [ts times];
   end
   save(filename,'kbs','kus','ts')
   buffer=0;
   thisindex=min(iku,thisindex);
   maxbuffer=limitbuffer;
else
   buffer=buffer+1;
```

```
    end
    if ~scanup
      iku=iku-1;  % Decrement ku value
      if iku<1 || buffer>maxbuffer
        iku=lastindex+1;
        buffer=0;
        scanup=true;
      end
    else
      iku=iku+1;  % Increment ku value
    end
    if iku>lengthku || buffer>maxbuffer
      scanright=true; % Check next kb value - all kb values are checked
    end
    if ~scanright
      if ~scanup
        disp(['Scanning down with ' num2str(maxbuffer-buffer) ' tolerance...']);
      else
        disp(['Scanning up with ' num2str(maxbuffer-buffer) ' tolerance...']);
      end
    else
      disp('Advancing independent variable...');
    end
  end
  lastindex=thisindex;
end
```

2. Reading and Processing SPE Images

Images produced by the Princeton Instruments charge-coupled device in the XM-1 transmission x-ray microscope are stored in the SPE file format. The following interactive MATLAB program reads a series of SPE files and converts them to images. The images are sorted such that every consecutive pair of images can be compared to each other through per-pixel division. The program will attempt automatic alignment of the two images using a rectangular region that the user selects. Subsequently, the user can manually use the arrow keys to finely adjust the alignment and use the square bracket and angle bracket keys to adjust brightness and contrast. The median noise and Gaussian blur filtering included can be tuned using the program's parameters. Finally, pressing the space key stores the displayed image. The input to the function is the bin number, which is chosen appropriately for the pixel size of the image. A function named metric that takes as input 2 matrices of identical dimensions is required for this code to function.

```
function SPEcompare(bin)
pixels = bin*512;   % Typical is bin = 2 for 1024 x 1024 pixels
blur = [3 3];   % Median noise filter range (pixels)
stretch = [0.005 0.995];    % Contrast range (percent pixels)
strint = 0.005; % Contrast range step size (percent pixels)
buffer = 16;    % Automatic alignment scan range (pixels)
shift = 0.5;    % Manual alignment step size (pixels)
gaussian = fspecial('gaussian',5,1);    % Gaussian blur
[Xq,Yq] = meshgrid((1:pixels),(1:pixels));
[trgname,trgpath] = uigetfile('../XM12013/092012/*.spe','Select images','MultiSelect','on');
```

```
if iscell(trgname)
   filesc = size(trgname,2);
elseif isnumeric(trgname)
   if trgname == 0
      filesc = 0;
   end
elseif ischar(trgname)
   filesc = 1;
   trgname = {trgname};
end
files = filesc/2;   % Create image arrays
refimgs = zeros(pixels,pixels,files);
trgimgs = zeros(pixels,pixels,files);
for f = 1:files
   fid1 = fopen([trgpath trgname{1,2*f-1}]);
   fread(fid1,2050,'uint16');
   array1 = fread(fid1,pixels*pixels,'uint32');
   fclose(fid1);
   fid2 = fopen([trgpath trgname{1,2*f}]);
   fread(fid2,2050,'uint16');
   array2 = fread(fid2,pixels*pixels,'uint32');
   fclose(fid2);
   matrix1 = reshape(array1,pixels,pixels);    % Raw images
   matrix2 = reshape(array2,pixels,pixels);
   refimgs(:,:,f) = medfilt2(mat2gray(flipud(matrix1)),blur,'symmetric');
   trgimgs(:,:,f) = medfilt2(mat2gray(flipud(matrix2)),blur,'symmetric');
   colormap('gray');
   imagesc(refimgs(:,:,f));
   axis image;
   rect = round(getrect);  % Create alignment boundary
   xmin = rect(1);
   ymin = rect(2);
   xmax = rect(1)+rect(3);
   ymax = rect(2)+rect(4);
   refimg = edge(refimgs(ymin:ymax,xmin:xmax,f),'canny');
   trgimg = edge(trgimgs(ymin-buffer:ymax+buffer,xmin-buffer:xmax+buffer,f),'canny');
   [wy,wx] = size(refimg); % Calculate automatic alignment
   n = 2*buffer+1;
   m = buffer+1;
   matrix = zeros(n);
   for i = 1:n
      for j = 1:n
         matrix(j,i) = metric(refimg,trgimg(j:j+wy-1,i:i+wx-1));
      end
   end
   [mins,ind] = min(matrix(:));
   [ty,tx] = ind2sub(size(matrix),ind);
   ty = m-ty;
   tx = m-tx;
   z = 0;  % Manual alignment and brightness/contrast
   while z == 0
      sy = round(ty);
      fy = ty - sy;
      sx = round(tx);
      fx = tx - sx;
      image = circshift(trgimgs(:,:,f),[sy sx]);
      image = interp2(image,Xq-fx,Yq-fy);
      image = mat2gray(imfilter(refimgs(:,:,f)./image,gaussian));
      image = imadjust(image,stretchlim(image(ymin:ymax,xmin:xmax),stretch));
      imagesc(image);
```

```
    axis image;
    waitforbuttonpress;
    try
    switch uint8(get(gcf,'CurrentCharacter'))
      case 28 % Left arrow
        tx = tx-shift
      case 29 % Right arrow
        tx = tx+shift
      case 30 % Up? arrow
        ty = ty-shift
      case 31 % Down? arrow
        ty = ty+shift
      case 91 % Left square bracket
        if stretch(1)-strint >= 0
          stretch = [stretch(1)-strint stretch(2)-strint]
        end
      case 93 % Right square bracket
        if stretch(2)+strint <= 1
          stretch = [stretch(1)+strint stretch(2)+strint]
        end
      case 44 % Comma
        newstretch = max((stretch(1)+1-stretch(2))/2 - strint,0);
        oldshift = (stretch(1)+stretch(2)-1)/2;
        tol1 = newstretch+oldshift;
        tol2 = 1-newstretch+oldshift;
        if (tol1 >= 0)&&(tol2 <= 1)&&(tol1<tol2)
          stretch = [tol1 tol2]
        end
      case 46 % Period
        newstretch = min((stretch(1)+1-stretch(2))/2 + strint,0.5);
        oldshift = (stretch(1)+stretch(2)-1)/2;
        tol1 = newstretch+oldshift;
        tol2 = 1-newstretch+oldshift;
        if (tol1<tol2)
          stretch = [tol1 tol2]
        end
      case 32 % Space: saves the image
        z = 1;
        imwrite(image,['xm1shot/' strrep(trgname{1,2*f},'.spe','.png')]);
      otherwise
        z = 0;
    end
    catch err
    end
  end
end
close;
end
```

Below is a sample metric function that calculates the sum of the per-pixel difference squared as an error metric for grayscale images. The smallest sum indicates the least error, but the rudimentary procedure used in the code above does not work well for images with background intensity gradients.

```
function z = metric(x,y)
z = sum(sum((x-y).^2));
end
```

3. Generating OOMMF Image Atlases

OOMMF uses images to determine what the material properties of each mesh point are. If large numbers of different images with systematic variations are needed for a series of OOMMF simulations, a tool that converts text into images may be useful. Below is an extensible MATLAB program that interprets an XML file as a layout, generates the corresponding image, and adjusts any parameters needed in the corresponding OOMMF script. The minimum mesh size in this program is 1 nm. More types of shapes can be added to images by writing additional statements inside the case block. Different OOMMF script parameters can be adjusted by editing the mif block near the end. Support for more than two colors can be added, but requires more significant code changes. The input to the function is a string that gives the path to the XML file.

```
function nmldraw(file)
% Get XML DOM tree
tree = xmlread(file);
% Parse image dimensions (nm) and meshsize (nm)
dimensions = tree.getElementsByTagName('dimensions').item(0);
magnets = tree.getElementsByTagName('magnet');
mesh = str2num(dimensions.getElementsByTagName('mesh').item(0).getTextContent);
xdim = str2num(dimensions.getElementsByTagName('x').item(0).getTextContent);
ydim = str2num(dimensions.getElementsByTagName('y').item(0).getTextContent);
name = char(dimensions.getElementsByTagName('name').item(0).getTextContent);
% Initialize image matrix and colormap
image = ones(ydim,xdim);    % 1 is white, 2 is black
map = [1 1 1; 0 0 0];   % white;black for a;b where a<b
for i = 0:magnets.getLength-1
   % For each magnet check what type of shape it is
   magnet = magnets.item(i);
   shape = magnet.getElementsByTagName('shape').item(0);
   switch char(shape.getTextContent)
      % Simple square magnet, origin x0,y0 at top left corner with side
      % length s.
      case 'square'
         x0 = str2num(magnet.getElementsByTagName('x0').item(0).getTextContent);
         y0 = str2num(magnet.getElementsByTagName('y0').item(0).getTextContent);
         s = str2num(magnet.getElementsByTagName('s').item(0).getTextContent);
         image(y0+1:y0+s,x0+1:x0+s) = 2;
      % Simple rectangular magnet, origin x0,y0 at top left corner with
      % extent dx in x direction and dy in y direction.
      case 'rectangle'
         x0 = str2num(magnet.getElementsByTagName('x0').item(0).getTextContent);
         y0 = str2num(magnet.getElementsByTagName('y0').item(0).getTextContent);
         dx = str2num(magnet.getElementsByTagName('dx').item(0).getTextContent);
         dy = str2num(magnet.getElementsByTagName('dy').item(0).getTextContent);
         image(y0+1:y0+dy,x0+1:x0+dx) = 2;
      % Rectangular magnet with concave edges along the top and bottom
      % approximated by rectangular cutouts so that the magnet resembles
      % an 'H', origin x0,y0 at top left corner with extent dx in x
      % direction and dy in y direction, cutout width cx and depth cy
      % where dx-cx must be an even number.
      case 'concaverect'
```

```
        x0 = str2num(magnet.getElementsByTagName('x0').item(0).getTextContent);
        y0 = str2num(magnet.getElementsByTagName('y0').item(0).getTextContent);
        dx = str2num(magnet.getElementsByTagName('dx').item(0).getTextContent);
        dy = str2num(magnet.getElementsByTagName('dy').item(0).getTextContent);
        image(y0+1:y0+dy,x0+1:x0+dx) = 2;
        cx = str2num(magnet.getElementsByTagName('cx').item(0).getTextContent);
        cy = str2num(magnet.getElementsByTagName('cy').item(0).getTextContent);
        image(y0+1:y0+cy,x0+1+(dx-cx)/2:x0+(dx+cx)/2) = 1;
        image(y0+1+dy-cy:y0+dy,x0+1+(dx-cx)/2:x0+(dx+cx)/2) = 1;
      % Rectangular magnet with concave edges along the top and bottom
      % approximated by rectangular cutouts and biasing wings along the
      % left and right approximated by rectangular growths, origin x0,y0
      % at the upper left corner of the 'H' so that the growths lie
      % outside the bounding box x:x+dx, rectangular dimensions dx,dy,
      % cutout width and depth cx,cy where dx-cx must be even, growth
      % width and height bx,by and y-separation bd between the centers of
      % the wings where dy-by+bd must be even.
      case 'biasconcaverect'
        x0 = str2num(magnet.getElementsByTagName('x0').item(0).getTextContent);
        y0 = str2num(magnet.getElementsByTagName('y0').item(0).getTextContent);
        dx = str2num(magnet.getElementsByTagName('dx').item(0).getTextContent);
        dy = str2num(magnet.getElementsByTagName('dy').item(0).getTextContent);
        image(y0+1:y0+dy,x0+1:x0+dx) = 2;
        cx = str2num(magnet.getElementsByTagName('cx').item(0).getTextContent);
        cy = str2num(magnet.getElementsByTagName('cy').item(0).getTextContent);
        image(y0+1:y0+cy,x0+1+(dx-cx)/2:x0+(dx+cx)/2) = 1;
        image(y0+1+dy-cy:y0+dy,x0+1+(dx-cx)/2:x0+(dx+cx)/2) = 1;
        bx = str2num(magnet.getElementsByTagName('bx').item(0).getTextContent);
        by = str2num(magnet.getElementsByTagName('by').item(0).getTextContent);
        bd = str2num(magnet.getElementsByTagName('bd').item(0).getTextContent);
        image(y0+1+(dy+bd-by)/2:y0+(dy+bd+by)/2,x0+1-bx:x0) = 2;
        image(y0+1+(dy-bd-by)/2:y0+(dy-bd+by)/2,x0+1+dx:x0+dx+bx) = 2;
    end
end
% Initialize smaller image with 1 pixel per mesh point
xrdim = xdim/mesh;
yrdim = ydim/mesh;
reduced = ones(yrdim,xrdim);
% To figure out the color at a pixel, just average a square of the size of
% the mesh grid and round.  Works for black and white colormap only.
for i = 0:xrdim-1
    for j = 0:yrdim-1
        reduced(j+1,i+1) = round(mean2(image(j*mesh+1:(j+1)*mesh,i*mesh+1:(i+1)*mesh)));
    end
end
% Save the image with corresponding filename
imwrite(reduced,map,strcat(name,'.ppm'));
% Generate corresponding OOMMF script file
miffile = fileread('nmldraw.mif2');
miffile = strrep(miffile,'$MESH$',num2str(mesh));
miffile = strrep(miffile,'$XDIM$',num2str(xdim));
miffile = strrep(miffile,'$YDIM$',num2str(ydim));
miffile = strrep(miffile,'$NAME$',name);
newmif = fopen(strcat(name,'.mif2'),'w');
fwrite(newmif,miffile,'*char');
fclose(newmif);
end
```

Below is a sample XML file.

```
<NML>

<dimensions>
<x>76</x>
<y>20</y>
<mesh>1</mesh>
<name>bgate</name>
</dimensions>

<magnet>
<shape>square</shape>
<x0>0</x0>
<y0>5</y0>
<s>10</s>
</magnet>

<magnet>
<shape>rectangle</shape>
<x0>20</x0>
<y0>0</y0>
<dx>10</dx>
<dy>20</dy>
</magnet>

<magnet>
<shape>concaverect</shape>
<x0>40</x0>
<y0>0</y0>
<dx>12</dx>
<dy>20</dy>
<cx>8</cx>
<cy>2</cy>
</magnet>

<magnet>
<shape>biasconcaverect</shape>
<x0>62</x0>
<y0>0</y0>
<dx>12</dx>
<dy>20</dy>
<cx>8</cx>
<cy>2</cy>
<bx>2</bx>
<by>2</by>
<bd>2</bd>
</magnet>

</NML>
```

Below is a relevant section of the template OOMMF script nmldraw.mif2.

```
# Grid sizes
set xcell $MESH$e-9
set ycell $MESH$e-9
set zcell 1e-9

# Image sizes
```

```
Parameter xpix $XDIM$
Parameter ypix $YDIM$
Parameter zpix 24
```

Below is the corresponding section in the resulting OOMMF script.

```
# Grid sizes
set xcell 1e-9
set ycell 1e-9
set zcell 1e-9

# Image sizes
Parameter xpix 76
Parameter ypix 20
Parameter zpix 24
```

The following is the resulting image atlas.

Figure B. 1: Image generated by MATLAB script where a square, rectangle, concave magnet, and biased concave magnet are placed by text.

Appendix C. Python Programs

1. Efficient Multi-Threading in OOMMF

OOMMF currently lacks any form of efficient support for multi-core processors. In order to gain performance, one must simultaneously run multiple simulations and task the operating system with allocating processing resources. The following Python script loops through two parameters using as many concurrent simulations as there are cores in the processor. Adjustments need to be made if a different number of parameters is needed. Adjustments are also needed to set the correct path to OOMMF, change the parameter space, and relay new parameters to OOMMF. However, this script provides a working framework for running concurrent simulations.

```
import os, sys, subprocess, time

root = os.getcwd()+'/oommf12a4pre-20100719bis'
allocated = 0

os.chdir(root)
threads = []
idles = []
maxthick = 51
maxdepth = 11
cores = 8

for depth in range(1,maxdepth):
  for thick in range(1,maxthick):
    command = 'tclsh oommf.tcl boxsi -parameters "D '+str(depth)+' H '+str(thick*2)+'" -- square.mif2'
    if allocated < cores:
      threads.append(subprocess.Popen(command,shell=True))
      allocated += 1
    else:
      while len(idles) == 0:
        time.sleep(1)
        for i in range(0,allocated):
          if threads[i].poll() != None and idles.count(i) == 0:
            idles.append(i)
      threads[idles.pop()] = subprocess.Popen(command,shell=True)

while len(idles) < allocated:
  time.sleep(1)
  for i in range(0,allocated):
    if threads[i].poll() != None and idles.count(i) == 0:
      idles.append(i)
```

Appendix D. Fabrication Recipes

1. Bi-Layer Lift-Offs with Lift-Off Resist

In typical lift-off processing one masks features using a bright mask exposure and evaporates on top if it such that the unwanted areas adhere to the photoresist and are removed when the photoresist dissolves in solvent. A common problem arises from the fact that the evaporated material will adhere to some degree onto the sidewalls of the photoresist. A much thicker than intended layer of material will build up at the edges of the masked features. Once solvent solution is introduced, this material will stay on the substrate because it is still anchored at its base by the substrate. The thick edges will cause issues when small features, smooth surfaces, or further processing is needed. Figure D.1 illustrates this issue with cross-sectional profile of a rectangular feature, measured by AFM.

Worse still, the thick edges may bend or break for soft or brittle materials when subject to mechanical forces such as the case during sonication. Typically a thin adhesion layer that adheres well to both the substrate and the target material is first evaporated as an interface material. This usually will allow the sample to tolerate sonication without causing the target material to rinse off in the solution. However, this does not help much in preventing the thick edges from separating. Figure D.2 is an SEM image that illustrates a

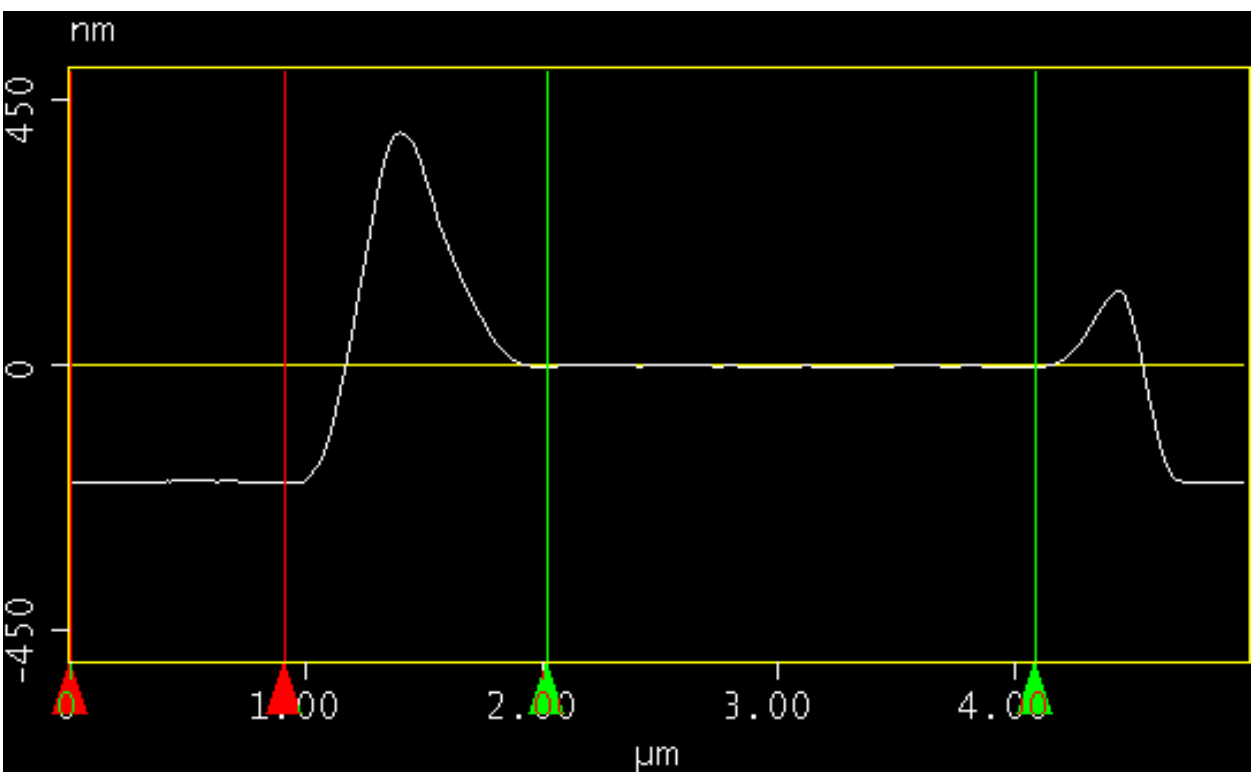

Figure D. 1: AFM height profile of a rectangle with significant lift-off edge residue.

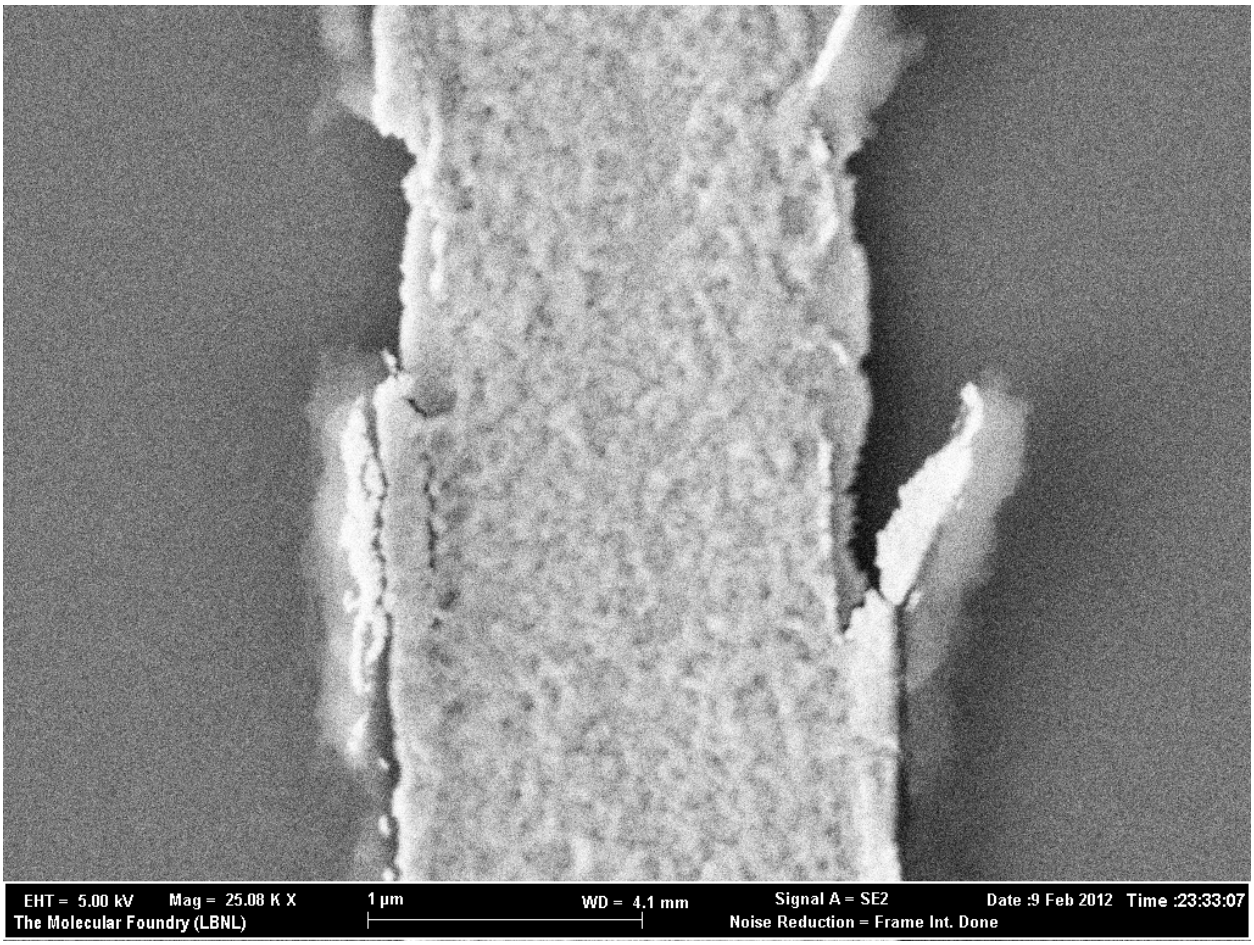

Figure D. 2: SEM of a rectangle with lift-off edge residue and peeling.

particularly bad case of thick edges bending and breaking after a copper lift-off.

The solution to this problem is to use bi-layer resists. An additional resist layer that undercuts the mask is inserted between the substrate and the photoresist. Evaporated material will still adhere to the sidewalls of the photoresist, but will no longer be anchored down to the substrate. Instead, this material hangs over the features and will wash away once the resists are dissolved. One combination of resists typically used is I-line and G-line photoresists. Their differing exposure rates will cause one to develop larger areas, making it appropriate as the undercutting layer.

The combination that the author used is MicroChem Lift-Off Resist (LOR) and Fujifilm positive photoresist. LOR is a spin-on film that does not expose, but etches in photoresist developer. It comes in multiple dilutions, which spin on at different thicknesses (the author used LOR-5A which is appropriate for evaporations of 100 nm – 200 nm). Before spinning, one should bake the sample to drive off any water. Unlike most photoresists, LOR does not need any hexamethyldisilazane (HMDS) for adhesion, and hardens rather than dissolves in acetone. The spin parameters determine the thickness of the LOR, which should be significantly (by a factor of 2 or more) thicker than the total

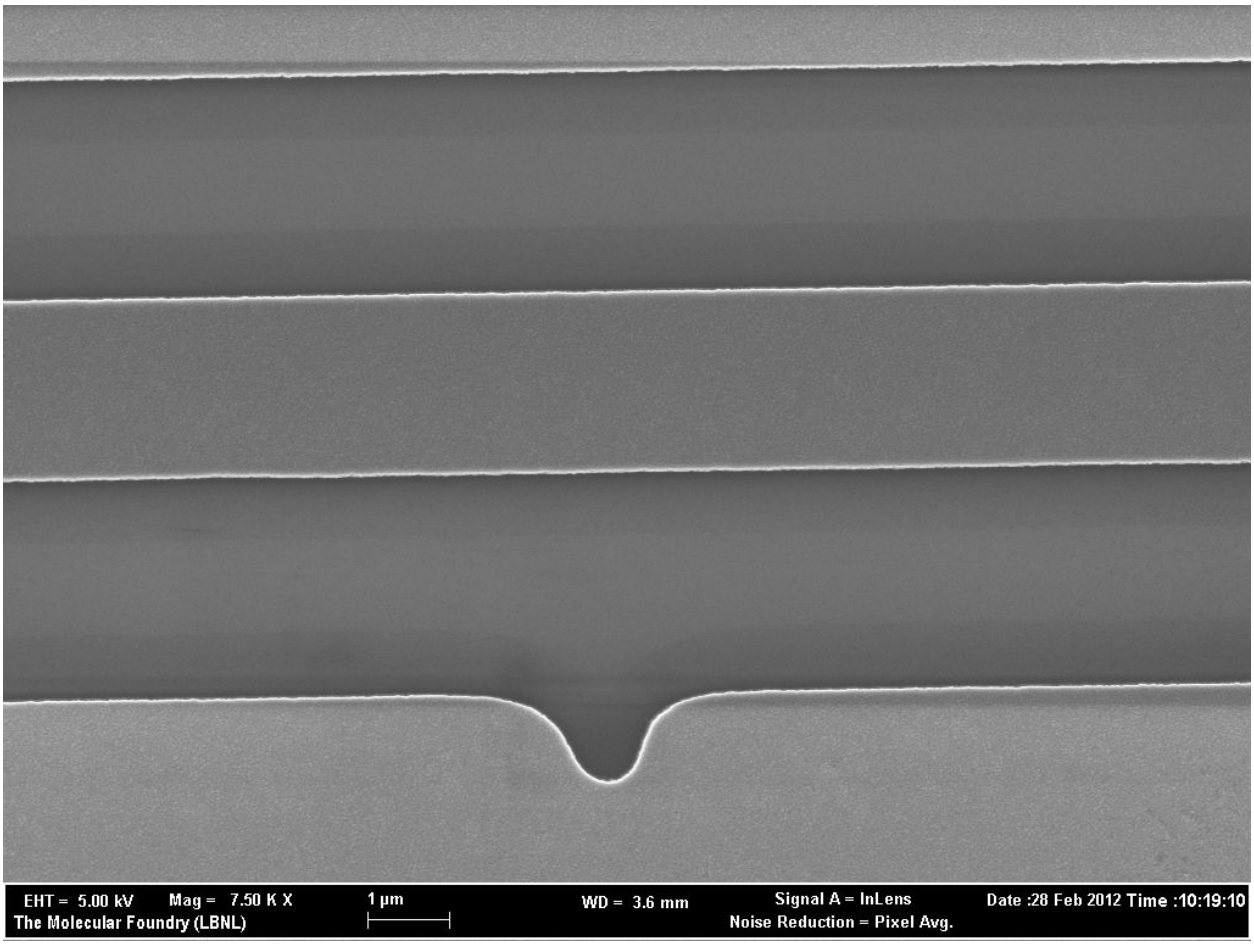

Figure D. 3: SEM of a rectangle after bi-layer lift-off.

thickness of evaporated material. 3000 rpm for 45 seconds is typical. After spinning, one should bake the sample to determine the etch rate of the LOR in photoresist developer. Higher temperatures and longer bakes result in slower etch rates. 150 °C – 180 °C for 10 minutes is typical. Afterward, one would spin on, soft bake, expose, and develop photoresist as normal. The LOR will etch faster than the photoresist in the developer solution, causing an undercut to form. Finally, after evaporation, lift-off should be performed in MicroChem Remover PG, which is a solvent that dissolves both LOR and photoresist. Figure D.3 is an SEM image that illustrates the drastic improvement in lift-off quality after evaporating copper onto a bi-layer process.

For larger chips as well as wafers, the author recommends that lift-off be done with the sample upside down in solvent solution. A levitation mechanism such as a wafer cassette should be used so that there is sufficient space under the sample. This way, material that has lifted off does not stick back onto the sample. Figure D.4 is a cross-sectional profile of a rectangular feature similar to the profile shown above, also measured by AFM, illustrating the clean lift-off gained by using bi-layer processes.

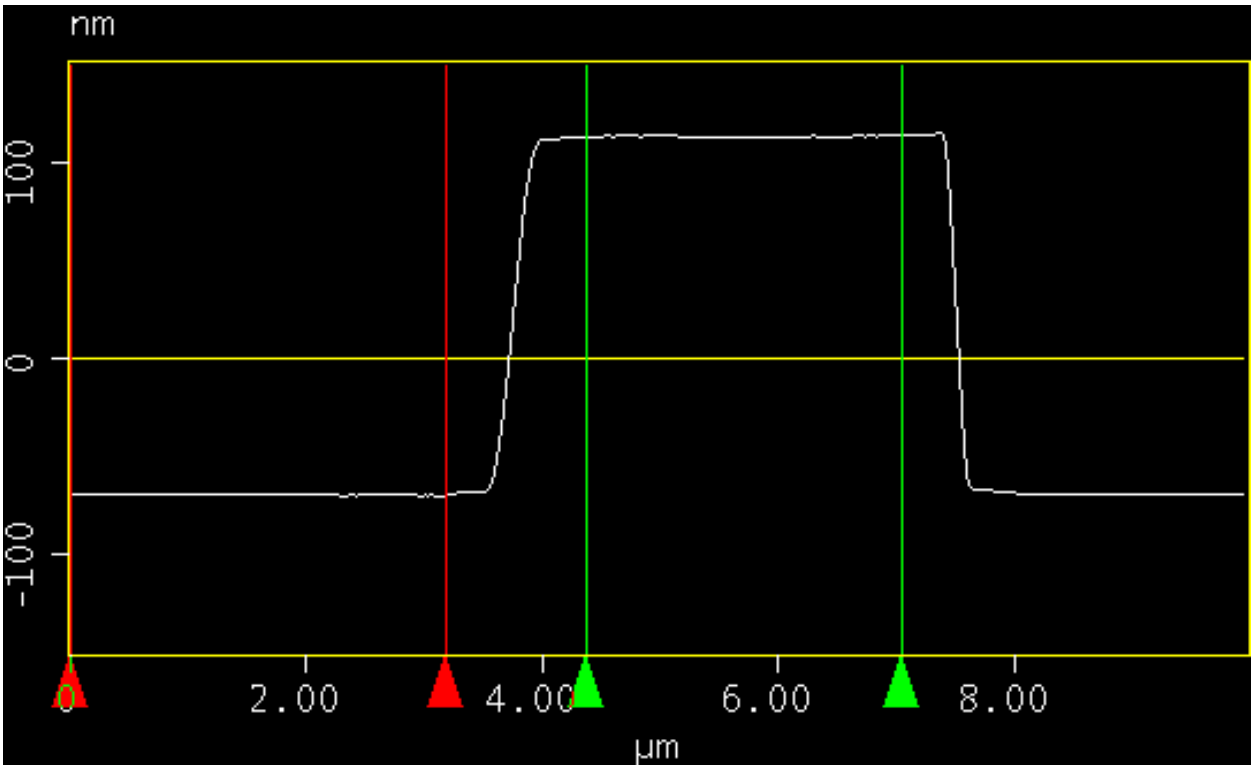

Figure D. 4: AFM height profile of a rectangle after bi-layer lift-off.

2. Surface Planarization with Spin-On Dielectrics

It is typically very difficult to get extremely smooth top surfaces on thick (100 nm or higher) evaporated metal features. Ideally, evaporations inherit the surface roughness of the substrate, but most metals tend to form grains, and as a result increase the roughness of the top surface as the deposition becomes thicker. An obvious step to take in ensuring the smoothest possible top surface is to ensure that the substrate is as smooth as possible before evaporation, using plasma de-scum or the like. Figure D.5 is an AFM image of the surface of a 160 nm thick gold evaporation after lift-off using a bi-layer process. The root-mean-square surface roughness is 1.9 nm.

If one requires an even smoother surface and can accept a layer of dielectric deposited on top of the metal surface, then spin-on dielectrics such as Honeywell's spin-on glass or Inpria's spin-on metal oxides can serve the role of planarization much better than

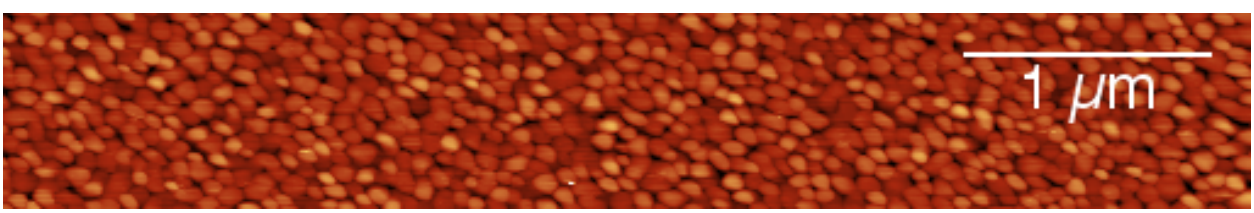

Figure D. 5: AFM image of a thick gold evaporation with grains.

Figure D. 6: AFM image of a 3-layer AlPO planarized thick gold evaporation.

chemical mechanical polishing (CMP). The author used aluminum oxide phosphate (AlPO) from Inpria for this purpose. The thickness that it spins on is determined by the spin parameters, but a typical thickness is 45 nm from 3000 rpm for 1 minute. The adhesion of AlPO depends on how hydrophilic the substrate surface is. An oxygen plasma clean before spinning usually helps in this regard. One should also be careful to keep all solvent fumes away from the substrate while spinning. After spinning, AlPO must be cured by a 5 minute bake at 350 °C. Multiple layers can be deposited by repeating cycles of clean, spin, and cure. If smaller (less than tens of microns) features need to be planarized, the AlPO thickness spun on over these features will be lower than that of bare substrate. Figure D.6 is an AFM image of the surface of the same 160 nm thick gold feature (6 μm critical size) after depositing and curing 3 layers of AlPO. The root-mean-square surface roughness has significantly improved to 0.3 nm.

Various wet etch recipes will work for etching AlPO. For a relatively slow, well-controlled etch, the author used 4 M phosphoric acid. Etch rates were not well characterized, though a 7.5 minute soak at room temperature removed at least 135 nm of AlPO.